2019

ROBOTICS AND SMART-GRIDS IN FUTURE POWER SYSTEMS: SENSING AND MONITORING THE GRID

MENÉNDEZ GRANIZO, OSWALDO ANÍBAL

UNIVERSIDAD TÉCNICA FEDERICO SANTA MARÍA
DEPARTMENT OF ELECTRONIC ENGINEERING

DOCTORAL DISSERTATION

ROBOTICS AND SMART-GRIDS IN FUTURE POWER SYSTEMS: SENSING AND MONITORING THE GRID

OSWALDO ANÍBAL MENÉNDEZ GRANIZO

DOCTORATE PROGRAM
DOCTORATE IN ELECTRONIC ENGINEERING

THESIS SUPERVISOR	:	PROF. DR. FERNANDO AUAT CHEEIN
EVALUATION COMMITTEE	:	PROF. DR. MARCELO PÉREZ LEIVA
	:	PROF. DR. MIGUEL TORRES TORRITI
	:	PROF. DR. MARCOS ORCHARD

MAY 2019

VALPARAÍSO-CHILE

All of my work is dedicated to my beloved parents Angélica and Oswaldo and my driving force behind this result my son Sebastián …

I couldn't have done it without you

Acknowledgements

There comes a time when the world gets quiet and the only thing left is your own heart. So you'd better learn the sound of it. Otherwise, you'll never understand what it's saying.

Sarah Dessen

Hoy que esta travesía llamada Doctorado ha llegado a su fin, en mi mente solo pasan miles de recuerdos de cada etapa vivida en esta magnífica experiencia de crecimiento personal y profesional. Hubo momentos en que hubiera querido regresar al pasado para corregir y cambiar aquellos momentos de tristeza, sin embargo he comprendido que cada recuerdo triste sirve para afianzar y enaltecer los miles de momentos de felicidad.

Agradezco a Dios por sobre todas las cosas por haberme guiado a lo largo de estos años y por haber sido mi fortaleza para poder culminar con éxito mi Doctorado. A mi mamá Angélica y a mi papá Oswaldo por todo el esfuerzo brindado a lo largo de mi vida, por ser un ejemplo de dedicación y esfuerzo, y por respaldarme en cada decisión que he tomado sin dejarme ni un momento desamparado. A mi hermana Paola por apoyarme en momentos de necesidad y representar la unión familiar. Mi sobrino Matías que lo considero como un hijo y me impulsa a seguir siendo un ejemplo. A mi abue Tere por creer en mí en todo momento. Y en especial a toda mi familia, por demostrarme su amor incondicional y respaldo.

Agradezco a mi director y tutor del doctorado Prof. Dr. Fernando Auat Cheein, un profesional invaluable con el que siempre estaré en deuda. Tener la oportunidad de trabajar con un investigador de tan alto nivel ha sido un honor, le agradezco por todos los conocimiento compartidos. El grupo ha alcanzando la excelencia gracias a su guía. Muchas gracias por la confianza depositada y por el respaldo brindado. Usted más que un guía se ha convertido en un amigo invaluable.

Durante mi etapa de doctorado tuve la oportunidad de conocer investigadores de excelencia que me aportaron muchas cosas en el ámbito personal y profesional. Agradezco al Prof. Dr. Marcelo Pérez por su ayuda y guía durante mi posgrado, al Prof. Dr. Samir Kouro por el tiempo y soporte brindados y al Prof. Dr. Miguel Torres Torriti por sus enseñanzas. Quiero agradecer al Prof. Dr. Andrés Rosales quien fue el vínculo entre la Escuela Politécnica Nacional y la Universidad Técnica Federico Santa María, por su amistad y ayuda.

En este punto no quisiera olvidarme de nombrar a aquellas personas que aunque no compartamos sangre son mi familia. Mis amigos del posgrado, personas magníficas, profesionalmente muy capacitadas, que hicieron de cada día algo muy acogedor. A Javier y Francisco, ustedes saben que este triunfo es de los tres, esto no hubiera sido igual si no hubiéramos coincidido, muchas gracias por sus palabras de apoyo y respaldo en las diferentes etapas de mi vida. Como olvidarme de mis amigos de colegio, han pasado 12 años desde que llenos de ilusiones salimos a la universidad, saben que toda la vida serán mis hermanos, gracias por permanecer a mi lado aun en la distancia, por compartir conmigo todos los momentos de triunfo, y más que nada sostenerme en aquellos momentos de tristeza.

Agradezco a la Universidad Técnica Federico Santa María por su excelente programa de posgrado, por abrir las puertas a estudiantes extranjeros y apoyar con su programa de becas. A cada uno de mis profesores mis más gratos agradecimientos. Quiero agradecer a la Comisión Nacional de Investigación Científica y Tecnológica (CONICYT-PCHA/Doctorado Nacional/2015-21151338) por el soporte económico brindado para mis estudios de Doctorado.

Finalmente, he reservado este párrafo para la persona más importante de mi vida, un ser que cambio mi forma de ver la realidad y que cada día lo amo más. Mi hijo Oswaldo Sebastián, caballerito cuando tengas edad y puedas leer este párrafo entenderás que todo lo que hice lo hice por ti. Cada minuto de mi doctorado pensé en ti y luche por ti. Aunque te dedico este triunfo, también te quiero agradecer que existas, tú has sido el motor que día a día me impulso a seguir. Gracias mi Caballerito!!!

RESUMEN EJECUTIVO

El crecimiento económico y demográfico a gran escala en varios países ha llevado a un aumento en la demanda de energía eléctrica alrededor del mundo. Actualmente Chile enfrenta desafíos energéticos tanto para el consumo habitacional, como el comercial e industrial, y ha planteado como objetivo fomentar el uso eficiente de la energía, estableciendo una ambiciosa meta de 20% de reducción de la demanda energética respecto a la proyectada al año 2025 (Ministerio de Energía, "Agenda de Energía: Un desafío país, progreso para todos". El esfuerzo país se focaliza en la búsqueda de fuentes de energía renovables no convencionales y en la optimización de procesos de operación y mantenimiento (O&M) dentro de los sistemas existentes con el objetivo de generar las condiciones adecuadas para alcanzar el desarrollo en las próximas décadas a nivel país (Estrategia Nacional de Energía 2012-2030, "Energía para el futuro: limpia-segura-económica, Gobierno de Chile").

Con este fin, el desarrollo de maquinaria basada en robots autónomos, Internet de las cosas, sistemas dedicados y máquinas inteligentes es la respuesta de la Ingeniería Eléctrica para abordar los desafíos cada vez más complejos dentro de una industria de energía en rápida expansión. Sin embargo, el uso de robots en sistemas de potencia es limitado debido a las condiciones extremas de los sistemas eléctricos de potencia y las restricciones mecánicas de los robots. En este contexto, esta tesis presenta un estidio completo y el desarrollo de diferentes sistemas dedicados relacionados con la robótica en sistemas de potencia, cuyo principal objetivo es el trabajo de mantenimiento.

Tres enfoques diferentes son propuesto con la finalidad de resolver diferentes desafíos: percepción de la red eléctrica, navegación de plataformas eléctricas y carga inalámbrica. Se presenta el análisis teórico y los lineamientos necesarios para su implementación práctica. Cada uno de los desafíos han sido abordados mediante la implementación de aplicaciones prácticas, y evaluados mediante simulaciones y pruebas de campo.

ABSTRACT

Accelerated demographic and economic growth in several countries has led to an increase in electrical energy demand. Inspection of power system assets –including conductors, protection systems, electrical towers/poles, transformers, and other devices– plays an important role to address the growing need for sustainable energy worldwide. Chile is facing various energy challenges that threaten both consumer and suppliers. To this end, government action and policy is geared to encourage efficient use of electrical energy, establishing an ambitious target: the reduction of 20% of energy demand with regard to projected at 2025 (Ministerio de Energía, "Agenda de Energía: Un desafío país, progreso para todos"). The internal polities are focused on the development of non-conventional renewable energies and the optimization of operation and maintenance (O&M) practices of current power systems in order to generate the adequate conditions to achieve the country development in the next few decades (Estrategia Nacional de Energía 2012-2030, "Energía para el futuro: limpia-segura-económica").

Within this context, the development of machinery based on autonomous robots, Internet of Things (IoT), embedded systems and smart machines is the response of the Electrical Engineering discipline to face the increasingly complex challenges within a rapidly expanding power industry. However, hazardous conditions of power systems and mechanical constraints of robots have limited their use. In this regards, this Thesis presents comprehensiveness study and the development of real applications of robotics in power systems. The main approach is the development of different dedicated systems that can be mounted in robotic platforms in order to solve different identified challenges.

Three different approaches are proposed in order to solve different challenges: perception of the electric network, navigation of electric platforms and wireless charging. The theoretical analysis and the necessary guidelines for its practical implementation are presented. Each of the challenges has been addressed through the implementation of practical applications, and evaluated through simulations and field tests.

Contents

List of Tables

List of Figures

Chapter 1

INTRODUCTION

1.1 Problem Statement, Context and Motivation

In recent years, global warming, increase in carbon emissions, demographic expansion and power demand have led governments and power companies to take concrete steps towards the development of larger and more complex power systems based on renewable energies and their integration within the current system. This complexity has a direct toll on inspection and maintenance tasks and the occurrence of blackouts in different electrical grids worldwide exposes the vulnerability of power systems. A clear example of the fragility of power systems befell on September 24th, 2011, in Chile, due to a fault in the transformer 500V / 230V from an electrical substation in Ancoa, causing a power blackout of the national power system. The electrical outage affected approximately 9 million people and interrupted normal operations in several copper mines with immediate impact on the local economy [1].

A power system embraces the electrical energy generation, its transmission, and its distribution to the end consumer [2]. Although the size and complexity of power systems can vary widely, they all have the same basic features and structure: they operate essentially at constant voltage and frequency and they are composed by generation, transmission and distribution stages [3]. An example of a typical power system including typical voltage levels and different types of users is shown in Fig. 1.1.

Power systems are vulnerable to numerous threats which can be classified into three main groups as shown in Table 1.1. Environmental threats are related to climate, temperature, and humidity; weather conditions that change in time and during the year, including the presence of snow, rain, wind, and dust, among other factors [4]. Operational threats are directly related to the continued use, installation of the electrical equipment [5], and the integration of renewable energy sources to a traditional grid (intermittency inherent). Human and animal threats are related to potential damage due to the presence and actions of living beings [6].

The main issues related to threats can be divided, according to their nature, into three groups as shown in Table 1.1: Chemical, mechanical and electrical. Chemical issues are mainly related to pitting corrosion [7, 8], which is an extremely localized corrosion that

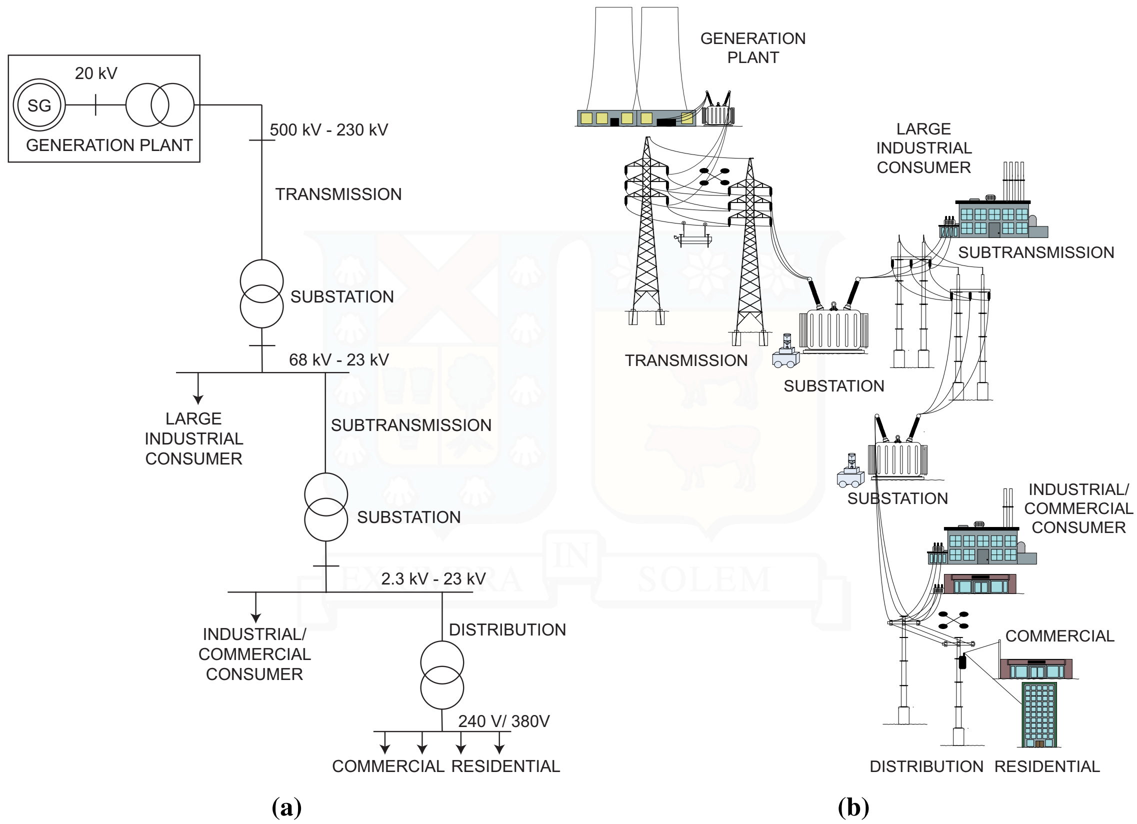

Figure 1.1: Basic elements of a power system: generation of energy and transportation to substations; transmission through substations and distribution. **(a)** Single-line diagram; **(b)** Structure diagram
. (Menéndez et al., 2017) © 2017 IEEE Industrial Electronics Magazine.

leads to the creation of small holes in the metal or to general corrosion which decreases the surface uniformly [9]. Mechanical problems, are mainly related to fractures or damages, as a consequence of the ageing or degradation of the equipment [4]. Finally, electrical problems are related to environment discharges, not only affecting the electrical equipment but also putting into risk people and workers [6].

The monitoring process of a power system is often neglected or shelved due to more pressing priorities, high deployment costs or industrial policies, which brings hardship to both unprepared business and society at large [10, 11]. Strategic assets such as transmission grids must be operated in a fast, secure and reliable way for proper fault-free operation [12]. To this end, operations and maintenance (O&M) practices of power systems must evolve to cost-effective practices that respond better to dynamical changes in power systems and can enhance life-cycle system economics. However, supervising the different power system stages is not a simple task due to their high complexity. As a solution, just a few years ago, it was commonplace for line crews to work on deenergized power lines. Nowadays, live-line work is more than ever a necessity in order to satisfy a society that demands a full availability of service. Helicopters are used to carry out operation and maintenance practices in power systems [13, 14], as these procedures can be performed on energized

Table 1.1: Main threats in power systems and their impact

Main Threats		Power System Impact	
Environment	Wind, wind+ice, Ice and snow, Salty or corrosive, Galvanic, Lightning, Earthquake	**Chemical corrosion**	Steel cross section; Zinc layer; Contamination Aluminium
Operational	Aging; Power cycling; Over current/voltage; Source intermittency	**Mechanical**	Fatigue; Creeping; Cracking/rupture; Fretting/unfastening
Animal and human	Bird scats; bird nest; Wood peckers/insects	**Electrical**	Partial discharge; Increase of resistence; Loss of insulation; Voltage reduction; Overheat

power lines without interrupting service. However, this technology is sometimes limited, due to the fact that power systems are hostile environments, which are often located in inaccessible locations. In addition, helicopter surveys are ecologically unsustainable and expensive (about 4000 USD per day). These constraints are a key factor in the introduction of robotics in this field.

Hence, the future of the power system inspection is focused on the inspection robotics with a special emphasis on dedicated systems capable of detecting and correcting failures in electrical equipment in real-time [15]. Robotic devices and self-sustainable mechanism based on embedded systems, smart-devices and Internet of Things (IoT) have proved to be a realistic approach for power grid owners. Safety, flexibility, efficiency, and reliability of devices are the main factors driving this trend. Figure 1.2a shows a conceptual traditional representation of the working environment of a smart-grid with inspection robots. Power system robotics is the modern technology that enables the assessment of the condition and status of power system components using different autonomous or remotely controlled machines. Its main objective is to reduce or eliminate human exposure to potentially dangerous environments while collecting the data required for reliable monitoring of electrical substations [16], high voltage overhead transmission lines [17] and power plants [18].

Robotic technologies used on power systems have evolved from tele-operated machinery [19, 20] to completely automated smart-robots [21]. Disregarding the use of robotic platforms in other situations (e.g. operation, assembling and control), successful case studies of them can be categorized into two main groups according to the tasks they perform: inspection and maintenance robots [15]. Likewise, potential robotic platforms are broadly classified as brachiating robots, unmanned aerial vehicles, and unmanned ground vehicles. Each one with its own advantages, disadvantages, and characteristics, summarized in Table 3.6. Unmanned aerial vehicles (UAV) have reached the technological summit during the last decade [22], due to their top-quality technical and economic performance.

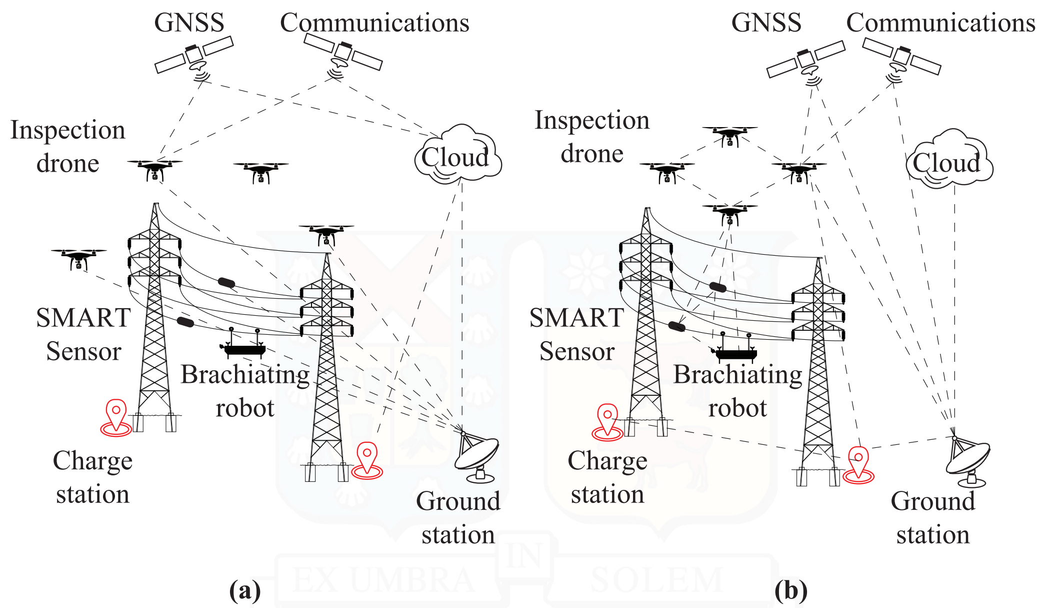

Figure 1.2: **(a)** Centralized architecture for electrical grid monitoring ; **(b)**Distributed architecture for electrical grid monitoring

During this period of time, UAVs evolved from a niche market of small scale applications to a common inspection, treatment and surveillance platform of electric equipment mounted on transmission grids. These robotic platforms can be used to perform inspection tasks of equipment under hazardous conditions or access restrictions, due to it navigation is only affected by Chilean Flight Regulation - DAN 151, where the guidelines to perform the UAV flight over high voltage overhead transmission lines is summarized.

The main advantage of robots is work safety since they can be used for high-risk tasks in hazardous working environments where people would be directly involved in accidents or mishaps. As the robots are very accurate machines, they can be optimally designed to perform specific tasks minimizing errors under different environmental conditions. In fact, the growing importance of robots for minimization of risk and execution of complex tasks within power systems has been addressed in [16, 31], where the importance and impact of this technology are underlined. Although robots are an enabling and already proven technology, its application to power systems presents several open challenges which must be faced [15, 32]. Autonomous robotics and teleoperated machines, despite being useful, have found only reduced application because of the limited payload capacity, autonomy, and availability. For example, Table 1.3 provides the payload analysis for several commercial drones. It is worth noting that no electrically powered unmanned aerial vehicle is able to develop a flight with duration more than 30 minutes [33, 34, 35, 36]. Therefore, the integration of robotic platforms and smart-grid sensors, as shown in Fig. 1.2b, could improve several inspection tasks in power systems, optimizing the inspection time.

Table 1.2: Comparison of three main robotic platforms used to perform inspection work in transmission lines.

Type of Robot	Ground vehicles	Brachiating robots	Unmanned aerial vehicles
Payload Restrition	Low	Medium	High
Navigation Restrition	Ground accessibility.	Crossing obstacles.	Chilean flight regulation.
Autonomy	High	Medium	Low
Maintenance work	Yes	Temporary repairs.	No
Development cost	Very high	High	Low
Industrial prototypes	LineMaster [23] Elevator IV [24] ROBTET [25]	LineROVer [26] Expliner [27] LineScout [28]	AIBOT-6 [29] UAV-Borne [30]

Table 1.3: Selected commercial drones

	DJI AGRAS MG-1 [34]	**FREEFLY ALTA 8** [35]	**DJI S1000** [36]	**HJ-5000**
N° Rotor	8	8	8	6
Battery Capacity	533 Wh	444 Wh	222 Wh	60 Wh
Maximum payload	9 kg	9.1 kg	8 kg	4.5 kg
Flight time	24 min	16 min	15 min	18 min
Weight	8.8 kg	6.2 kg	4.4 kg	3.0 kg
Price	13.500 USD	15.000 USD	4500 USD	2300 USD

1.2 The challenges of power system robotics

Very few robotic technologies have actually been implemented in grid operation, inspection, and maintenance practices. The two main reasons are: (i) power system robotics is a young research field; (ii) place a robotic platform on a transmission grid is a very complex process due to the fact that the power grid infrastructure is very critical and susceptible to damages. Therefore, a robotic platform has to be capable of addressing different challenges and restrictions in order to achieve successful implementation. Briefly:

- Robot capacity to work on live-line power grids: Sometimes, power systems cannot be deenergized due to generated economic losses it could entail, and the reduction of the customer satisfaction.
- Systems availability: The robotic platform must be able to perform inspection and/or maintenance work in several situations, in which other methods cannot be used.
- Perception of the grid: The robot must be able to analyze the condition of any component, tool or equipment mounted on the grid.
- Robustness: Power systems are hazardous environments where a robotic platform can be affected by a large number of threats (electromagnetic interference, electromagnetic fields, mechanical shocks, environmental conditions). Reliability and safe

operation are paramount given the strategic importance of the target assets.

- Self-sustainability: Technologies face extremely challenges to ensure high-accuracy data collection and enhanced inspection work quality. Robots must run during long working periods and do it so autonomously.
- Inspection and/or maintenance tasks: Robotic inspection incorporates imaging, sensing, and other technologies to assess the condition and status of power system components. These applications must be significant to asset managers. Therefore, the selection of the robot platform (its technical characteristics, and its potential application) is not an ambiguous solution.
- Information and communication technologies: The robot should be able to send the inspection data to a central operations center for further analysis.

1.3 Hypotheses

This thesis addresses the following questions regarding power system robotics.

1. *Could the use of low-cost sensors based on vision enable to characterize the most representative artifacts associated with the power system functionalities?*

   The visual and infra-red monitoring of electrical equipment is a non-invasive inspection method which provides information about possible failures, regarding thermal behavior of the device to the operational status of the power system. This thesis will test a portable ground-based system capable of detecting and classifying hot-spots related to photovoltaic module failures. The system characterizes in 3D-thermal information from the panel structure to detect and classify hot-spots. Unlike traditional systems, this system is provided with a removal algorithm that will be able to detect and eliminate false hot-spots associated with people or device reflections, and from external radiations sources.

2. *Which is the performance of low-cost sensors in the positioning of robotic platforms used to develop inspection tasks in power systems?*

   Technology constraints related to the payload and autonomy could affect critical processes such as navigation and localization, restricting the use of power system robots. A navigation system based on global navigation satellite system (GNSS) is currently the most adopted sensing mode to locate robotic platforms over different industrial environments [37]. In an electrical environment, however, the use of GNSS is limited due to size and weight constraints of robotic platforms and sensors; it can be affected by electromagnetic interference and, additionally, it could not operate in cluttered urban areas; it is not reliable at low altitudes and suffers from satellite signal cuts. This thesis faces this challenge by developing a transmission line autonomous tracking system, which enables the location of a commercial drone over a transmission grid using a monocular camera. This feature provides the vehicle an accurate positioning even when the GNNS signal is denied, enabling to report the status of the line at any time.

3. *Is it possible to exploit the phenomenon of electric field induction on objects in the proximity to power-lines energized at power frequencies as energy supply?*

   Electric field energy harvesting is a promising solution to energize a variety of self-sustainable wireless sensor nodes, which may be used in next-generation smart-grids. In this Thesis, a low-power energy harvesting system targeting to extract energy from the electric field around energized wires is presented. Unlike the conventional electric field harvesters, the generators described in this work is intended on contactless household low voltage applications. A low-power design methodology to reduce power dissipation and to increase the harvested power has been implemented, considering the electric field scarcity in household applications and a variety of challenging design issues. In addition, the proposed harvester is equipped with a mechatronized maximum power point tracking system, that is used to automatically varies the location of the electrodes until harvesting the maximum power.

1.4 Thesis Structure

The thesis is oriented to present a comprehensive analysis of the robotic systems and smart-devices to perform the inspection work in power systems.

Chapter 1 This chapter introduces the context of this thesis and presents the research objectives addressed in this work. It also provides a description of the main contributions developed.

Chapter 2 This chapter aims to collect and review the main contributions regarding robotics in power systems to establish the main links and gaps between power systems and robotics. It also includes the robot classification according to the task they perform and their navigation system.

Chapter 3 This chapter aims to face two challenges "Perception of the grid" and "Inspection and/or maintenance tasks". In this context, a 3D characterization system for photovoltaic modules is presented. provides the main technical details of the proposed system. In addition, it develops the theoretical analysis and practical implementation of the system. Experimental findings are presented to evaluate system behavior.

Chapter 4 This chapter aims to address the dare "Systems availability". To this end, this chapter presents the development of a low-cost positioning system for unmanned aerial vehicles. In addition, detailed theoretical analysis, computer simulations and experimental results are presented to test the proposed system and underscore its accomplishments and constraints in terms of efficiency.

Chapter 5 This chapter aims to address the dare "Self-sustainability". This chapter introduces a non-contact approach for electric field energy harvesting that uses the parasitic capacitance between energized wires. Also, the chapter includes a review of the energy harvesting methods available for smart-grids, with special emphasis on electric field energy harvesting.

Chapter 6 This chapter details the overall conclusions of this research work.

Chapter 2
LITERATURE REVIEW

Power systems face numerous challenges to address the growing need for sustainable energy worldwide. Monitoring of mains in real time requires distributed and centralized processing of large amounts of data from distributed sensor networks in order to increase the grid reliability, to analyze the aging status and to detect potential failures. Hence, the transformation of the power system from a less informed or a dumb system to a smart-grid system is indispensable. Within this context, several tasks directly focused on power systems operation can be either partially or completely automated by unmanned or tele-operated autonomous robots, self-sustainable systems, and smart machines. The development of these sophisticated mechanisms helps to address the increasingly complex challenges within rapidly expanding power industry, ensuring an efficient, cost-effective and safe maintenance process. This chapter explores the main contributions from the robotics field to the inspection and maintenance of power systems through the analysis of the state-of-the-art and current advances.It also presents a comprehensive market survey of the power system robotics. The main conclusions from this chapter are:

- Most robots in power systems are designed and built for a single specific task, such as transmission-line supervision, detection of the hot-spots, vegetation management or surveillance, thus limiting their potential in the industry. Future works in this field might focus on increasing the versatility of robots in power systems and improving their sensory systems to allow multitasking.
- The new generation of power system robots is focused on the integration between smart-grid technology and robotics. Increasing the interaction between robots and power systems beyond inspection and maintenance would be a step toward a fully autonomous power system industry.
- Unmanned aerial vehicles can be considered as an emerging and promising alternative in order to perform inspection tasks on power systems, due to their top-quality technical and economic performance. Despite UAVs are an enabling and already proven technology, its application to power systems presents several open challenges related to the navigation, payload constraints, and its limited autonomy.

2.1 Robotics in Power Systems

Early publications regarding applications of power system robots basically reported tele-operated machinery for maintenance of substation transformer and power transmission lines [19, 20]. In this scenario, the use of robots in the electric industry was focused mainly on the development of tele-operated robots for maintenance and inspection of live power lines [21]. A few years later, the first publications on mobile robots appeared addressing the security patrolling of substation [38], overhead distribution line work manipulation and underground cable conduit monitoring [32]. These works became the earliest validated robotic prototypes used in power systems.

Several robotic platforms have been developed to perform operation and maintenance practices in power system [39, 26, 28, 27, 40, 29]. The most noteworthy initiatives can be classified into two groups according to the task that they perform: inspection and maintenance. Using robots for these tasks improved the management of the electric power systems by adding new value and capabilities to the process, due to the high adaptability of robots to different environments otherwise hostile for human labor force [41, 42, 43]. Furthermore, robotic platforms are broadly classified as ground vehicles, brachiating robots, and aerial vehicles by this thesis. By regarding this separation and the frequency of preference, some leading robotic systems are discussed. A further description of the evolution of robot usage in power systems and its corresponding milestones is shown in Fig. 2.1, where it is depicted, in time, the impact of robotics in the power systems field.

2.2 Inspection Task

Inspection tasks are focused on applications that do not require direct contact with the asset. Inspection robots aim to detect and analyze the mains status using modern remote sensing sensors, such as light detection and ranging systems (LIDAR), synthetic aperture radar images (SAR) and a huge number of different cameras (visual, thermal, ultraviolet). These remote sensors are used for the monitoring of power system components, potential failure sources, and vegetation around the power system. They can be classified within three categories: brachiating robots, unmanned aerial vehicles (UAV) and unmanned ground vehicles (UGV), according to the needs of the power system (e.g., power plant, transmission line, and substation).

2.2.0.1 Brachiating Robots

Brachiating robots, like the one depicted in Fig. 2.2, move either on the conductors for inspecting transmission lines or on the steel cables in the case of substations. For example, *Tokyo Electric Power Co* in cooperation with *Toshiba Corporation* designed a mobile robot for the inspection of transmission lines in 1991. Such robot had to inspect 66 kV fiber-optic overhead ground wires (OPGW) and navigated over a ground wire that was located above the actual power transmission lines [21]. The robot comprised a controller and power source, and it was self-propelled, with two different behavior modes:

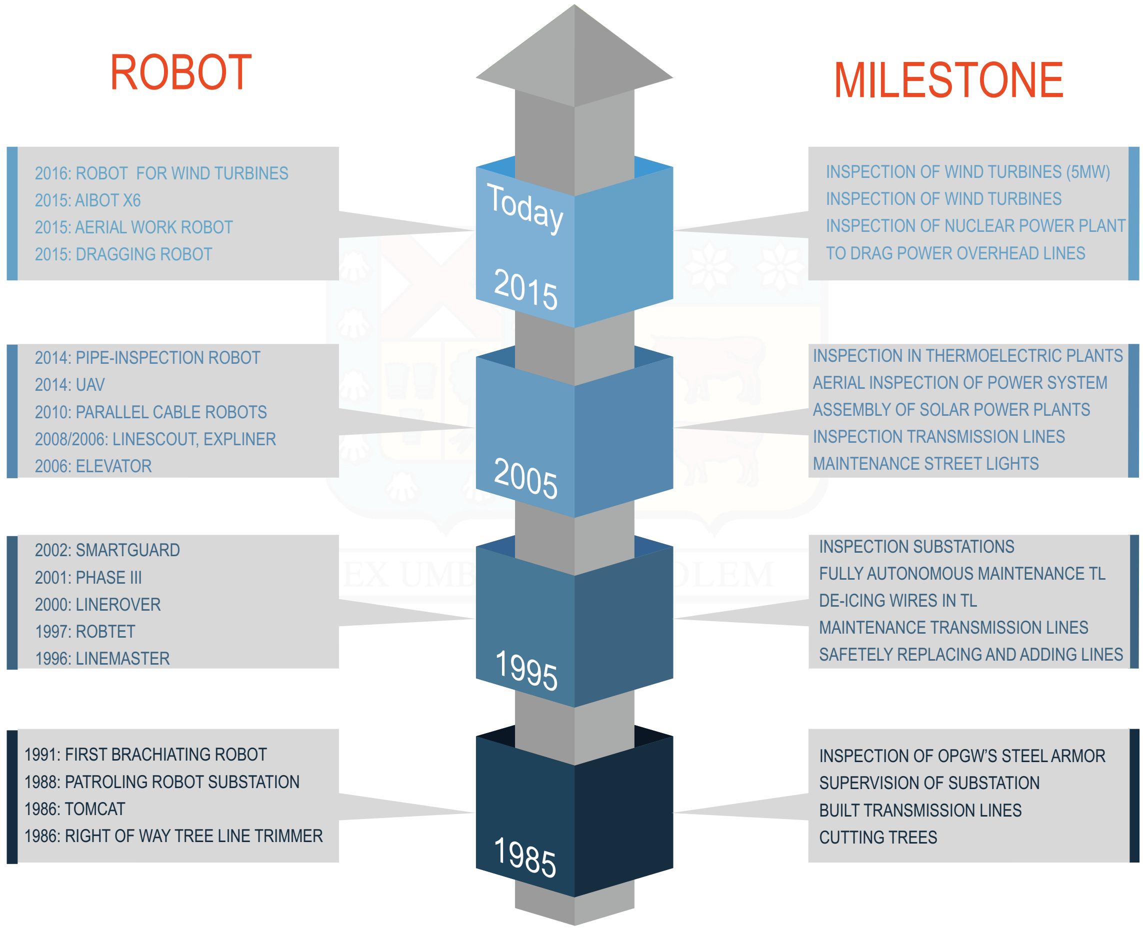

Figure 2.1: Time-line of robots usage in power system. (Menéndez et al., 2017) © 2017 IEEE Industrial Electronics Magazine.

one for approximating motion using pre-programmed data concerning the tower and power line information, and the other one for precise positioning. The automata was outfitted with a tower detection sensor based on a range ultrasonic device, subsidiary contact sensor, guide rail sensing function used for contacting ground wire (resistance measurement of motor torque), clamp wheels status detection sensor and guide rail hook status sensor (status detection by interruption of fiber optic light source, presence of OPGW, open & closed status of hook claw).

With the same aim, *Hydro-Québec Research Institute (IREQ)* presented in 2000 its first prototype of the mobile robot called LineROVer. First presented as an overhead ground wire de-icing application, the capabilities were later improved in the following version called HQ LineROVer [44]. The HQ LineROVer was equipped with an infra-red camera and a monocular camera (RGB), to collect images related to temperature differences that arose from components such as compression splices and insulators with the aim of detecting hot spots and potential problems [45]. Currently, *Hydro-Québec Research Institute (IREQ)* has developed a commercial system for performing inspection tasks on transmission grid based on LineROVer technology [26].

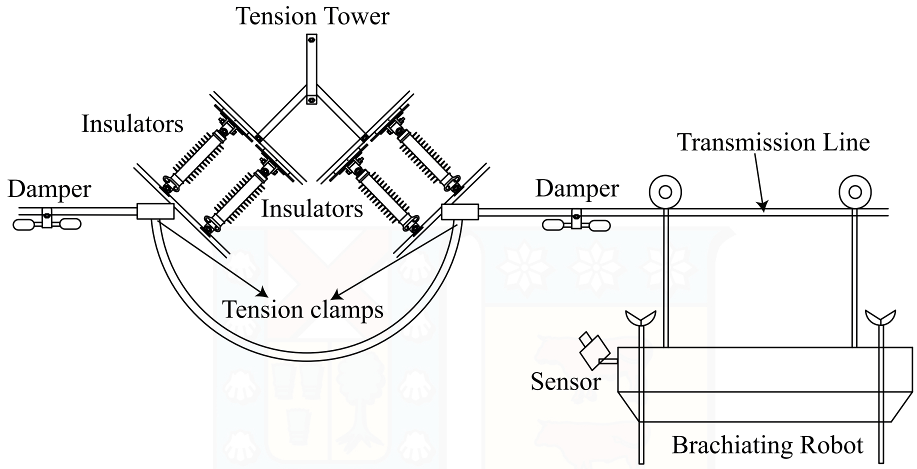

Figure 2.2: The brachiating robot on a transmission line. (Menéndez et al., 2017) © 2017 IEEE Industrial Electronics Magazine.

In 2006, IREQ developed a new platform named LineScout. The main feature of this robot was the capacity of clearing obstacles as it traveled down a line [46]. It can move along several axes, allowing it to adjust its shape in real time to various line configurations and to a wide range of obstacles while remaining as light and compact as possible. It has a robotic arm with a camera for visual inspection of line components which allows for splice condition evaluation and some live-line working. The implementation of programmable pan & tilt camera (PPTC) units and a dual end effector robotic arm (LineArm) to work on bundled conductors was annexed later [47]. The use of Light Detection and Ranging (LIDAR) UTM-30LX to obstacle detection on power line conductors is implemented in [48] and in a sequel of the work, presented in [49]. Since launched, Linescout technology has progressed; Hydro Quebec conducts development, manufacture and sales activities of the overhead transmission line inspection robot nowadays [28].

On the other hand, *Kansai Electric Power Corp. (KEPCO, Japan)*, *Japan Power Systems Corp. (JPS)* and *HiBot Corp.* presented in 2008 a robot designed for remote inspection of powered high-voltage transmission lines named *Expliner* [50]. The robot was composed by motion units (two shafts, each with two pulleys), a base (actuators of the vertical poles) and a manipulator and counter-weight. The *Expliner* was able to detect the ruptured strands using two CCD mini-cameras and a mirror assembly, and also able to detect corrosion employing laser sensors to measure the diameter of the cable. Since 2014, *Hitachi High-Tech* in conjunction with *Hitachi High-Tech Fine Systems* started to develop a commercial prototype based on this technology [27].

State Grid Shandong Electric Power Research Institute (Electric Power Robotics Lab) in association with *State Grid Shandong Electric Power Company (Grid Maintenance Department)* designed a brachiating robot for inspection of overhead transmission lines in China [51]. The system was composed by three arms with two of them equipped with a gripper, designed to clamp firmly onto the conductor to secure the robot.

The *University of Shanghai for Science and Technology* developed a robotic system

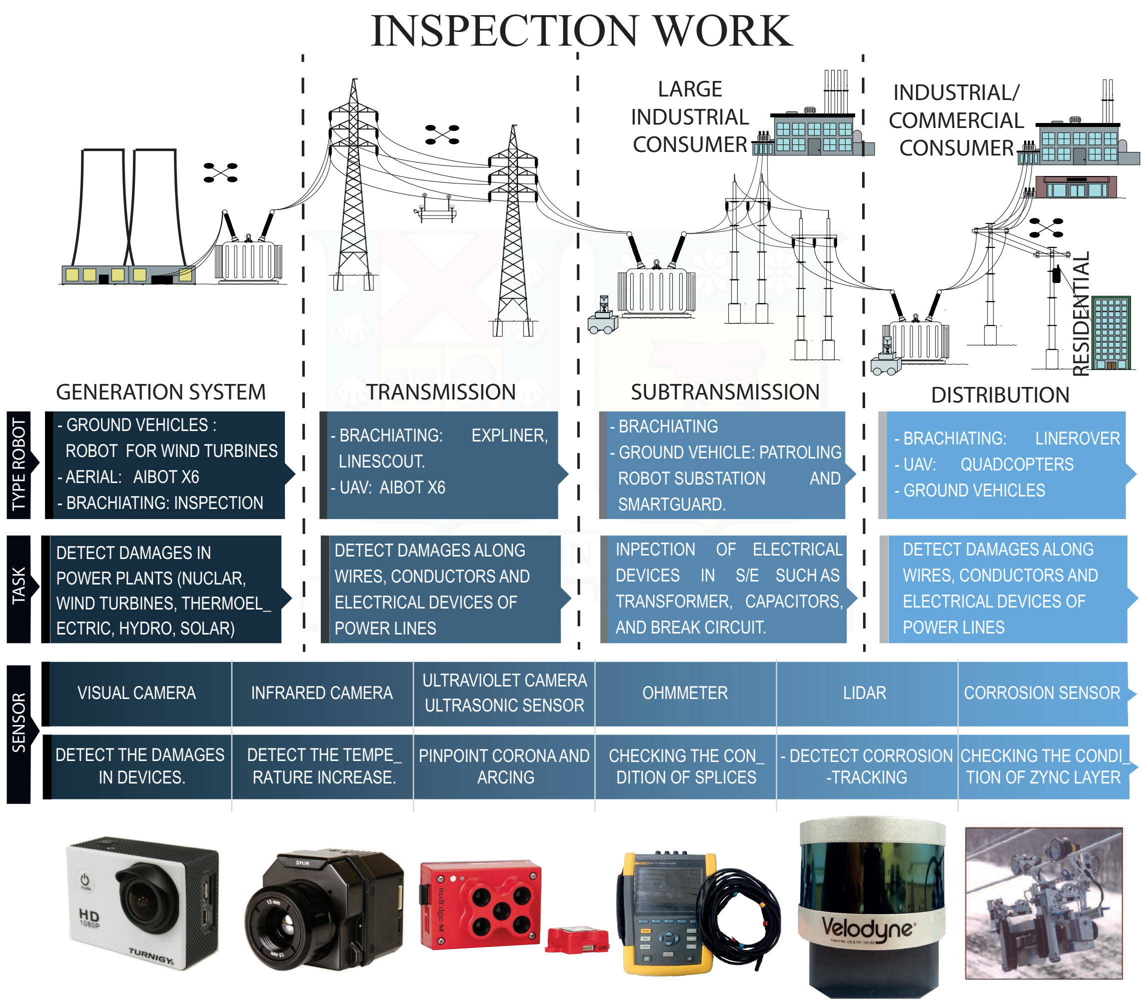

Figure 2.3: Robotic technology applied in power systems for inspection tasks. (Menéndez et al., 2017) © 2017 IEEE Industrial Electronics Magazine.

for inspection of transmission lines of 500 kV [52]. The system walks on overhead ground wires in a 500 kV power tower and can evade obstacles meanwhile it inspects and supervises the electrical equipment. A ground based station remotely controls the robot.

Electric Power Research Institute (EPRI) has been focused on the development of an automata capable of crawling over conductor shield wires along 80-mile long corridor. The system takes advantage of power harvested from power-conductors, supplemented by power from on-board solar panels for running its motors. The system identifies nearby trees that could pose a risk to wires, evaluates right-of-way encroachment and assess the status and condition of the electrical equipment using high resolution cameras [53].

Periodic inspection of the insulators in power transmission lines is required in order to prevent it from failure, which has been known as a major cause of power failure. *Korea Electric Power Corporation (KEPCO)* developed a robotic system for live-line suspension insulator strings [6]. The main aim is to prevent insulator failure in 345 kV power transmission lines. The robot structure is very simple, small-sized, lightweight and

Table 2.1: Example of brachiating robots used in power systems. (Menéndez et al., 2017) © 2017 IEEE Industrial Electronics Magazine.

Type of Robot	Examples of Brachiating Robots		
Name	LineROVer	LineScout	Expliner
Research Group	Hydro-Québec Research Institute (IREQ)	Hydro-Québec Research Institute (IREQ)	HiBot Corp and KEPCO
Year	2000	2006	2008
Inspection sensor	- Infrared and visual camera - Corrosion sensor - Ohmmeter	- Infrared and visual camera - Corrosion sensor - Ohmmeter, ultrasonic device	- Visual camera - LIDAR
Maintenance actuator	- De-icing tool - Foreign suspender clearing tool	- Line Arm with 3 modules: device to measure the splice resistance, wrench and device to repair clamps.	- No actutors
Weight	23 kg	112 kg	60 kg
Live-Line Working	Yes	Yes	Yes
Resistence to EMI	315kV - 800A	735kV - 1000A	500kV - 800A
Energy source	Lithium-ion battery	Lithium-ion battery	Lithium-ion battery
Battery life	45min -10h (depending the task)	5 hours	8 hours
Harvesting energy	Yes (200A primary / 1.13A)	No	No
Autonomy	Controlled by an user	Controlled by an user	Semi-automatic: User not need to control every single detail
Remote control range	1 km	4 km	500m
Ambient temperature range	-10ºC to 35ºC	-10ºC to 35ºC	0ºC to 30ºC
Main Applications	- Visual and infrared inspection. - Verification of splice condicion by measuring of resistence. - Corrosion detection. - De-icing of overhead ground wires and conductors. - Replacement ground wires and conductors - Conductor repair	- Visual and infrared inspection. - Detection of broken strands under suspension clamps - Verification of splice condicion by measuring of resistence. - Corrosion detection. - Tightening and loosening bolted assemblies - Conductor strand repairs.	- Visual inspection. - Corrosion detection.
Platform	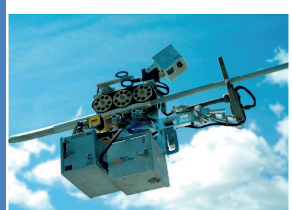		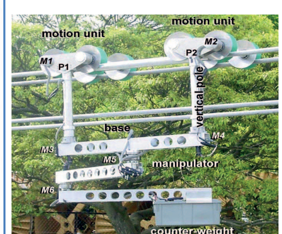

adopting a wheel-leg mechanism for moving along a suspension insulator string.

A summary of the most relevant brachiating robots– including technical characteristics and main applications– is featured in Table 2.1.

2.2.0.2 Unmanned Ground Vehicle

Ground vehicles are also applied to power systems, with its corresponding manoeuvrability features completely different from brachiating robots, making them more appropriate for other different tasks [54]. For example, *Chubu Electric Power Co* developed a patrolling robot for the supervision of the substations [21]. The robotic system navigates around the substation with electromagnetic guidance following a wire buried 1 cm below the surface.

In the same context, *Shandong Electric Power Research Institute* has been developing mobile robots for the inspection of substation equipment since 2002, named as Smartguard [16]. SmartGuard is composed of a robotic platform and a data center. The motion control module consists of four wheels for the navigation, two for traction and two for heading. A magnetic guiding system, presented in [55], acts as a localization system of the SmartGuard. It consists of magnetic markers placed in a roadway that serves as reference for the vehicle. The positioning is implemented using Radio Frequency Identification (RFID) technology. The robot has incorporated a vision system composed by a near-infra-red illumination subsystem, an omnidirectional imaging subsystem, an artificial landmark subsystem, and an image processing subsystem. The robot sees four landmarks at all time and finds its location based on triangulation. A navigation system based on infra-red vision for a mobile robot designed for substation inspection is presented in [56]. Vision systems for navigation and positioning were also reported previously, as shown in [57], where the robot moves on the yellow inspection line of 10 cm width on the power substation ground. Range sensors, such as LiDARs are also used by robots in substations, although its usability is restricted to navigation purposes only [58].

The robotic technology is also well established for solving new challenges in a substation inspection. A clear example was developed for inspecting electrical equipment shown in [59], where it is provided a mobile inspection robot that includes a robot body and a drive system supporting the robot body and configured to manoeuvre the robot over a electric environment. In addition, the development of tele-operated inspector is described in [60], which can tilt and lift a binocular camera and a thermometer by two telescopic rod to analyze the status of the high position electrical equipment.

2.2.0.3 Unmanned Aerial Vehicle

Nowadays, the use of unmanned aircraft vehicles (UAV) has become increasingly popular for the visual industrial inspection, since these systems are able to capture images in difficult and dangerous areas of access [42, 29]. The use of aerial vehicles for inspection tasks on power systems is a recent area of research with many challenges. One of them is related to navigation and control of the attitude around the transmission line. A solution for this problem is based on the design of Extended Kalman Filter observer to preview dynamic attitude of a quad-rotor and to control the aircraft in order to avoid getting out of safe flight paths as shown in [61, 62]. Another approach, and also more conservative, is based on Proportional Integral Derivative (PID) controllers. They are designed based on the linearized model of the UAV. This technique is applied mainly to Vertical Take-Off and Landing (VTOL) [63].

In current applications it is common to use aerial vehicles, such as helicopters, equipped with artificial vision systems for inspection tasks [22, 64]. The images are processed and analyzed with the purpose of detecting faults, damages or problems in the structure or in the performance of the transmission line, such as in [65] where a detection system of damaged cables based on video recordings obtained from aerial inspection of transmission lines is presented. The system detects arc marks and cut wires as consequences of lightning strokes. A brightness check system based on statistical analysis is used to detect arc marks; whereas a shape check system based on the features of the cable is used to detect cut wires. Other applications based on the same technology are used for detection and recognition of insulators [66] or conductors [67] in a transmission grid. In the first application, the detection algorithm is based on a region-based active contour model (ACM) to solve problems related to the existence of the local minimum and the inability to segment images with severe texture inhomogeneity; whereas the second algorithm uses spatial correlation between pylon and line for transmission line detection. In addition, as a case study, in [68] a vision system mounted on UAV that it is able to detect the distance between transmission lines is presented, to evaluate or alert about the distances among lines to a ground operator. Also, it is possible to improve the transmission lines detection by merging several techniques such as Hough transform and Neural Networks [69] or using and matching the data of some sensors such as LIDAR with both a visual camera [70] and a stereo vision camera [71].

Despite the attractiveness of UAVs, they are limited by their navigation range and endurance, due mainly to the limited battery capacity. As a solution, a wireless charging system for UAVs is proposed and developed [72]. This work aims to use wireless charging UAVs for infrastructure inspections of transmission lines. The approach is based on a resonant circuit for wireless energy transmission. Another solution rises from the use of current transformer (CT). The transformer has characteristics such as simple structure, low price, and easy designing [73]. Therefore, better performance can be obtained in inducting power for inspection robot from power transmission lines when using CT.

The capacity of using the transmission lines for self-powering the robot is a new research trend. The first contributions related to this issue can be found in [74], where it is presented the design of a small rotor-craft with a pick-up mechanism. The rotor-craft is equipped with an artificial-vision system and based on the Hough transform, it is able to detect the transmission line. In the same context, robots powered by the transmission line can also be found in [75].

2.3 Maintenance Task

Following the previous analysis, the most important applications from a robotic, sensor and actuator perspective in maintenance tasks are shown in Fig. 2.4. As before, three main types of robots arise brachiating robots, unmanned ground vehicles (UGV) and unmanned aerial vehicles (UAV). Maintenance robots are used to develop the preventive and corrective maintenance of the mains. In some cases, the robotic system should be installed in the live-line where damage occurs. To this end, a huge set of actuators can be mounted in these platforms, whose main goal is to repair the electrical equipment in real time.

2.3.0.1 Brachiating Robots

In general, brachiating robots are highly used for performing maintenance work in transmission networks. The main tasks are: to repair and change electrical devices such as the broken strand in the overhead ground wires (OGWs). The robot should be able to move along the line, get across some obstacles and approach the damage [76]. Also, it is important to note the voltage level since the main enforcement of this type of robot it is the capacity for working in live-line. In this context, the development of the robotic system for autonomous installation and removal of aircraft warning spheres on overhead ground wires of electric power-lines is described in [77]. The robot travels on the ground wire, and its main task is to install and remove the signaling spheres. The operator is responsible for guiding the robot on the wire, thus moving the robot to approximate it to a position where the signaling sphere will be installed. The robot has a gripper which is used for the installation and removal of the spheres.

Korea Electric Power Research Institute in 2006 presented a robot for live-line inspection of transmission line insulators for 345 kV high voltage line. The robot was designed to achieve three specific tasks: to clean insulators, to measure insulation resistance, and to detect cracks. A megger connected to a live-line is used to measure the insulation resistance; the crack is detected by analyzing the sonic resonance frequency of the insulator generated when the robot applies some impact to the insulator [78]. This kind of robot could be used for cleaning the surface of live-line insulators without using water, adopting a dry cleaning method. In addition, the robotic machine can perform cleaning and inspection of the surface of the live-line insulators while automatically moving along an insulator string, as shown in [79].

Hydro-Québec developed a robot prototype for the construction of overhead distribution lines which has as the main feature, the possibility to ascend and descend a pole by tele-operation, and the installation of a pre-assembled cross-arm at the top of a 40 foot (12.20 m) pole [80]. The robot is composed of a climbing system, the cross-arm manipulation system, and the bolting system. In addition, the University of Tehran designed a robotic system that has the same form of navigation aiming to reduce the complexity and increasing the payload of the robots [81]. Finally, climbing robots are also very used in maintenance and inspections tasks of vertical structures as shown in [82, 80, 81].

2.3.0.2 Unmanned Ground Vehicle

Ground robots are highly used to perform maintenance work since 1980. TOMCAT (Teleoperator for Operations, Maintenance, and Construction using Advanced Technology) is an early prototype based on this technology, which was developed by *Electric Power Research Institute (EPRI)* in 1986. The purpose of introducing this system was to address live-line procedures, mainly, maintenance for high voltage overhead transmission lines (138 kV to 765 kV) [19].

Four years later, in Japan, the *Kyushu Electric Power CO (KEPCO)* introduced Phase I, which consisted of a robotic arm coupled to a ground vehicle. It needed a skilled operator for the use of the robotic arm and two operators for the control of the vehicle; the main weakness was the potential risk of human fall [83]. At the end of 1996, *KEPCO* updated the system to Phase II, which allowed live-line work. In addition, Phase II was designed for semi-automatic operation, with the operator assisting via remote controls from a cabin on the ground. The tasks were conducted automatically, with the operator providing judgment and commands for each unit task. The robotic system was composed by a dual-arm manipulator, cameras, a 3D position-finding sensor, an automatic tool changer (ATC), an automatic material changer (ANIC), and a third arm [84]. Publications from 2001 reported that around 93 robots of Phase I and Phase II are working on site. The same year, the company presented a new update of this robot called Phase III, which is a fully autonomous [83].

In Spain, the *Universidad Politécnica de Madrid* introduced a maintenance robot, the aim was to do maintenance and repairing of distribution lines rated up to 49 kV. The technology behind this system, called ROBTET, is reported in [25]. The main tasks of the robot were insulator string replacement, opening, and closing of bridges, bypasses, and branch installation. The robot is composed by the truck, an insulated telescopic boom achieving a maximum height of 15 m, a rotating platform located on the top of the boom, two hydraulic manipulators with force reflection, a jib is placed next to the slave manipulators on the rotating platform and visual sensor (stereo vision system and overall view camera) for control and surveillance of the robotic system by an operator.

In the same context, *Shanghai Jiaotong University* developed a live-line robot called DWR-I [85]. The main goal was to help the operator in repairing and maintenance tasks of distribution live-lines. The system is designed to work in distribution networks at medium voltage levels (up to 10 kV). The main tasks of the robot are exchanging broken insulators, exchanging fused switches, cutting and jointing wires. The system reduces the live working operators workload and human live working risk, and it is composed of a mobile vehicle, booms, robot portions, and control system.

Quanta Energized Services presented LineMaster Robotic Arm [23, 86], the aim was to find a solution for specific live-line projects, such as the replacement of rotten poles utilizing the existing hole, re-conductoring of existing transmission lines conductors, and re-framing and re-insulating of structures, which are typically difficult to execute with traditional live-line tools like hot-sticks [54]. Currently, *Quanta Energized Services* manufactures, applies and markets its robotics technology in two different systems: Single-Phase and Three-Phase LineMaster Robotic Arm. The single phase LineMaster Robotic Arm is capable of handling voltages 765 kV, supporting at 4535 kg in vertical and horizontal applications. Added to this, the three-phase LineMaster Robotic Arm is capable of handling voltages about 345 kV per phase and supporting 136 kg - 1020 kg per phase in vertical and horizontal applications respectively [40].

Companhia Paulista de Forca e Luz (CPFL) in partnership with *Escola Politecnica of Sao Paulo University* reported the design of a robotic platform for maintenance of public lighting equipment in Brazil. The first and second version of the system called Elevator, are described in [24]. Elevator I was an electrically assisted automatic elevator used for the maintenance of street lights. The system aims to reduce efforts in maintenance tasks. The actualization of the robotic system called Elevator II aims to provide a wider workspace, enabling electrician to reach more components of the distribution line. Later, the company updated the robotic system and presented a version called Elevator IV, which is a mechatronic computer controlled device, equipped with electrical and hydraulic actuators and sensors to facilitate maintenance and fault detection in lighting equipment and it was first reported in [87]. In the same work was described the previous version called Elevator

Table 2.2: Example of unmanned ground vehicles used in power systems. (Menéndez et al., 2017) © 2017 IEEE Industrial Electronics Magazine.

Type of Robot	Examples of Unmanned Ground Vehicles (UGVs)		
Name	LineMaster (Three phase)	Elevator IV	ROBTET
Research Group	Quanta Energized Service	Companhia Paulista de Forza e Luz (CPFL)	Universidad Politécnica de Madrid
Year	2008	2014	1995
Inspection sensor	- Position control sensor - Visual camera	- Position control sensor to monitor bucket position. - Visual camera	- Stereo vision system - Over-all visual camera
Maintenance actuator	- Unit consist of adaptor, robotic arm and fiberglass segment	- Telescopic column made of aluminum	- Two commercial master-slave system with force reflection. - Two slaves ares hydraulically powered.
Weight	136 kg - 1020 kg per phase	1500 kg	120 kg
Live-Line Working	Yes	Yes	Yes
Votage level	up to 345 kV	Distribution lines	up to 56 kV
Energy source	Generator	Batteries or vehicle engine	Generator of 10 kW
Isolation	Electric	Electric	Electric
Autonomy	- Controlled by an user in vehicle or a lineman in bucket	- Controlled by an user in bucket	- The user sends and receives commands and information from the cabin on the truck.
Height	60 m	10 m	15 m
Degrees of freedom	3 (Elevation, Inclination and rotation)	3 (Elevation, Inclination and rotation)	6 (Master and Slaves)
Main Applications	- Relocating energized conduc_ tors of different voltages level.	- Development of maintenance process of street lights.	- Perform maintenance tasks on distribution networks.
Platform	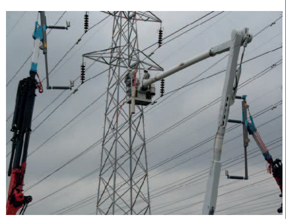	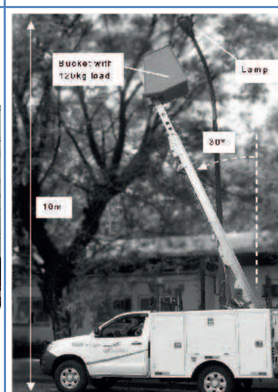	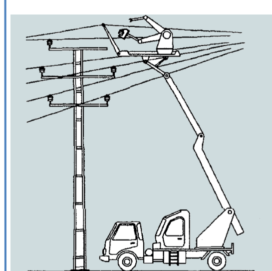

III.

Meijo University in collaboration with *Chubu Electric Power Co.* in Japan, reported a semi-autonomous system for checking the status of power-lines. The performance of the proposed robot system is previously analyzed in a Computer Graphics Simulator (CGS), which counts with all the necessary technical specifications for solving different simulated cases. The controller is composed by a human-machine interface, task planner, motion planner, arm controller, tool controller, and computer graphics display. The system is fitted with a robotic arm (from Mitsubishi Electric) and the three cameras (type SONY EVI-D100) for solving maintenance tasks in distribution lines such as: installing a switch gear, removing the high voltage insulator or peeling the coating off a cable [88].

Finally, it is worth mentioning that different kinds of robots were developed for the trimming of branches and limbs from standing trees along rural power lines. A mobile robot called Tree trimmer telescopic was patented in 2011 [89]. The mechanism has been designed with the purpose of removing difficult to reach overhead tree branches. It consists of a motorized vehicle and it features a cab for the operator and an articulated boom. The end of the boom carries a circular saw and by pivoting the boom sections vertically relative to the vehicle and to the operator it was able to cut a swath of branches or limbs. A tree-trimming apparatus mounted on a mobile support vehicle was patented in 2014 [90]. Similar devices to trim vertical sections of trees can be found in [91] and commercial prototypes provided by TERRATECH [39].

A summary of the most relevant ground-based robots –including technical characteristics and main applications– is featured in Table 2.2.

2.3.0.3 Unmanned Aerial Vehicle

Nowadays, helicopters are significant and efficient tools to accomplish inspection and maintenance work in power systems, which are capable of working on energized lines without interrupting service. The first work dates back to 1980 and the essential idea was to replace the spacers in transmission systems [13]. Inspection work is performed by a trained pilot, who is highly qualified to fly around power-lines. Additionally, a lineman with a special suit hanged from a helicopter corrects and repairs damages in power-lines [14].

Modern sensor technology, like ultraviolet and infra-red cameras, makes helicopters a much better choice from an innovative point of view. The infra-red cameras mounted in aerial vehicles enables to detect damages by measuring the temperature increase on the electrical devices. The ultraviolet camera enables the detection of distance corona discharge, and the video camera enables the performance of a visual inspection and the damage detection along power-lines [92]. Furthermore, helicopters can be equipped with different actuators to maintain power-lines, such as airborne tree trimming apparatus [93], stringing blocks for building the transmission line or hose for cleaning insulator strings [13]. Because of the success of helicopters, UAVs technology could appear as a versatile and cost-effective solution to perform maintenance work in power systems. However, UAVs are not used for maintaining power systems, due to the difficulty of installing mechanisms (e.g. robotic arm, clamps, wrench) for repairing the electrical equipment and their weight limitation. Nowadays, UAVs are mainly used to assist ground operators and not to actually perform maintenance work [94].

2.4 Discussion

Several countries around the globe require larger and more complex power systems to satisfy their own energy demands. This complexity directly influences on inspection and maintenance work, which are significant processes to ensure high quality and reliability of electric power supplied to industrial and commercial customers. In this context, the continuous and stable operation of the power system is the result of efficiently performing

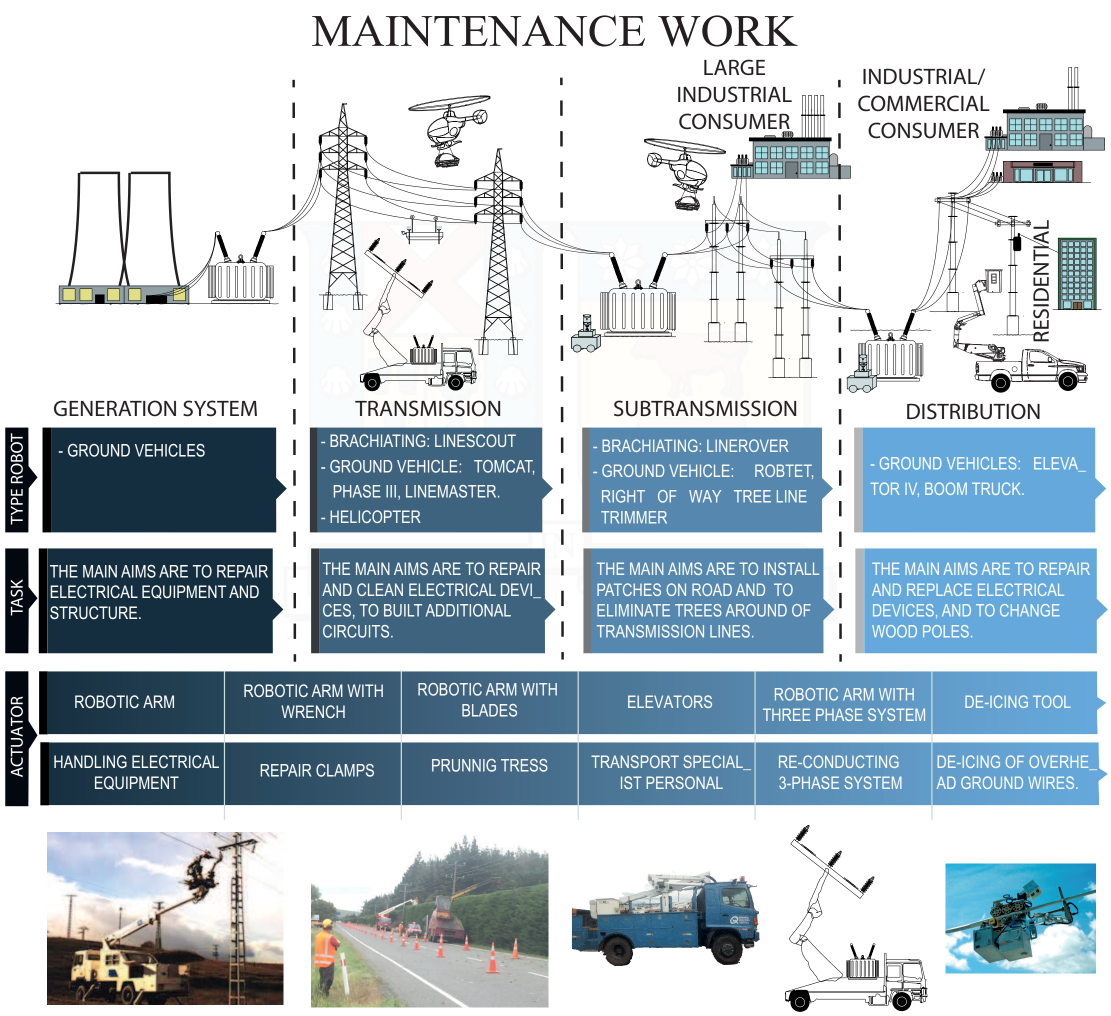

Figure 2.4: Robotic technology applied in power systems for maintenance tasks. (Menéndez et al., 2017) © 2017 IEEE Industrial Electronics Magazine.

the different processes, such as a detailed inspection and periodic maintenance. Neglecting such approaches could lead to a faulty operating system, which entails economic losses, fines, and surcharges, and essentially a critical impact in the industrial and commercial customers.

2.4.1 Inspection Robots

Inspection work is traditionally performed by qualified and skilled operators, who are responsible for detecting and repairing damages in electrical equipment. The process is dangerous and insecure because the power systems are hostile environments and often they are placed in hardly accessible locations. Nevertheless, several works have resolved many challenges by developing autonomous or remotely controlled machines, which incorporate sensors, actuators and other technologies to assess the condition and status of power system components. The main idea is to reduce or eliminate human exposure to potentially dangerous environments while collecting the data required for reliable monitoring of the power system. This work has shown that the most used robotic platforms for power system inspection are classified into three groups: brachiating robots, unmanned ground vehicles, and unmanned aerial vehicles.

- Brachiating robots are ergonomic platforms, which move on ground wires or conductors. The main advantage is the capacity of supervising segments of lines built on inhospitable places such as mountainous or agricultural regions and rivers, highway and railway crossings. A further benefit is the ability to work on energized lines without interrupting the service. This technology is highly used for detecting and repairing damages on transmission and distribution equipment and for inspecting the substation equipment state. The robots detect potential damages with non-invasive sensors such as visual cameras (analyzing of overhead ground wires, conductors and line hardware), infra-red cameras (detecting hot spots in electrical equipment), ultraviolet cameras together with ultrasonic devices (pinpointing corona and arcing), and ohmmeters (checking the condition of splices). Nevertheless, despite the available commercial prototypes and sustainable researches, technology has considerable disadvantages in the field of stability, controllability, ability, and autonomy. Additionally, the power-lines design is a constraining factor in the system mobility along the lines. Though, the challenges are to develop a platform able to surmount and cross the different obstacles, including towers and trees and solve the limitations of size and weight.

- Ground vehicles can be used for performing the inspection work in substations. Inspection robots are mainly used for detecting hot spots or visual faults in electrical devices. Due to the fact that systems are limited to move through specific regions of a substation and several electrical devices are located in inaccessible places, it is difficult to develop an efficient and detailed inspection in the substation using ground vehicles.

- Unmanned aerial vehicles are mainly used for detecting damages along transmission lines with different sensors such as visual cameras, infra-red cameras, ultraviolet cameras, and frame cameras. The challenge, though, is to enhance the flight capacity and autonomy. Due to the difficulty of installing mechanisms (e.g. robotic arm, clamps or wrench) and the limitation of size and weight, UAVs are not used for performing maintenance. Nevertheless, the counterpart (manned vehicles) is the main tool in several maintenance and inspection tasks. The technology consists of a civil airborne with different sensors or actuators, which are handled by an expert operator and a line-man is hanged to its base (repairing electrical equipment). Important disadvantages are the expensive costs of operation; UAVs do not provide workers a good measure of the state of power-line because helicopters cannot fly at close distance to the line; and due to the risk of contact and falls they are still not sufficiently safe for the workers.

2.4.2 Maintenance Robots

The future of power systems robotics focuses on maintenance tasks with an emphasis on robots being able to detect and correct damaged electrical equipment. Nowadays, both autonomous robotics and tele-operated machines, despite being useful, have found only limited application because of the payload capacity of platforms. However, the large variety of actuators will enable a suitable adaptation of the robot in future maintenance applications. As mentioned above, main robotic technologies for power system surveillance can be classified into three essential groups: brachiating robots, unmanned aerial vehicles, and ground vehicles, each with their own technical and specific characteristics.

- The use of actuators in a brachiating robot relies on their size and weight restrictions, reasons why its use is limited to carry out temporary corrections. The robots are capable of correcting issues since they are in contact with the wires using different actuators such as robotic arms (replacing ground wires or repairing conductors), wrenches (tightening and loosening bolted assemblies) or special tools (de-icing of overhead ground wires and conductors). Nevertheless, despite the commercial prototypes and sustainable researches, technology has reported considerable disadvantages in the field of stability, controllability, availability, and autonomy.
- Ground vehicles are used mainly for performing the maintenance work in the transmission grid. Nowadays, significant progress has already been made in a number of fields, becoming in an advanced technology, which is used to conduct maintenance tasks in free access places due to its great autonomy. These systems are an ideal technology for heavy duty tasks such as detecting and correcting potential damages along conductors and wires and relocating energized circuits of different voltages since they are equipped with manipulators installed at their extremities. Nevertheless, the systems have important disadvantages, which are largely due to limitations of the crane (e.g. the long arm, degrees of freedom, insulation), and, to a larger extent, the system cannot move in several challenging locations where power systems are located(e.g. mountains region, rivers, valleys).
- Because of the success of helicopters in solving maintenance tasks in power systems, UAVs technology could appear as a versatile and cost-effective solution to perform maintenance work in power systems. However, UAVs are not used for maintaining power systems, due to the difficulty of installing mechanisms (e.g. robotic arm, clamps, wrench) in order to repair the electrical equipment and their payload limitation. Nowadays, UAVs are mainly used for assisting ground operators and not for actually performing maintenance work.

2.5 Contributions

The research work presented in this chapter is extended and detailed in:

O. Menéndez, F. Auat Cheein, M. Pérez and S. Kouro, "Robotics in Power Systems: Enabling a More Reliable and Safe Grid," in IEEE Industrial Electronics Magazine, vol. 11, no. 2, pp. 22-34, June 2017. doi: 10.1109/MIE.2017.2686458. **Impact Factor:** 10.429

Chapter 3

APPLICATION OF SENSING SYSTEMS TO PHOTOVOLTAIC MODULES DIAGNOSIS

Accelerating deployments of solar photovoltaics (PV) worldwide are placing increasing emphasis on cost-effective inspection practices that can enhance life-cycle plant economics during its life cycle. In this context, long wave infrared detection technologies are suitable methods for detecting a huge suite of different risks in PV-modules, which can be associated with manufacturing defects, module damage, temporary shadowing, defective bypass diodes, and faulty interconnections. This Chapter describes the development and implementation of an inspection system of PV-panels, whose goal is the thermal characterization of the most representative artifacts associated with the PV's functionalities. Because of the high system's flexibility, it can be mounted on almost any manual, tele-operated or robotic platform. In addition, the system incorporates a novel algorithm that evaluates the status and condition of PV-modules through the analysis of their thermography.

Two stages describe the proposed system: PV-module segmentation and PV-module inspection. In the first stage, unlike the works presented in [95, 96, 97, 98, 99, 100], the algorithm uses the same visual information acquired to localize the sensor and to reconstruct the PVs. The latter is based on an artificial vision system strategy called photogrammetry, but instead of using visual RGB (red, green and blue) information, as used in [101, 102, 103], the system takes advantages the thermal information. This method was empirically and theoretically validated in [104]. The second stage is focused on using the 3D reconstruction and visual information processing to extract artifacts from the PVs. This stage includes the artificial intelligence algorithms used for classification and pattern recognition described herein. In addition, the algorithm is able to eliminate hot-spots associated with external radiation sources and reflections.

This chapter is organized as follows. Section 3.1 details the hardware, software, and protocols followed to evaluate the proposed methods for PV characterization; Section 3.2 shows the results obtained when tested the proposed approach on PVs under different environmental and lighting conditions. Finally, Section 3.3 summarizes the contributions of the case studies presented in this chapter.

3.1 Experimental Setup

The system consists of a thermal camera, a tripod, and a companion computer, as shown in Fig. 3.1. The exteroceptive data provided by the camera is stored in a local memory card and later processed on a ground station. The mechanisms can be described in general terms as follows:

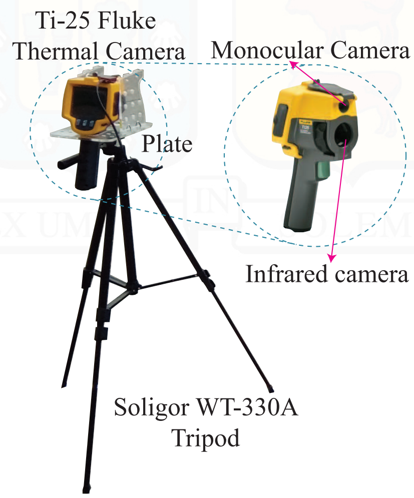

Figure 3.1: Proposed measurement system. The system is composed of an thermal camera Fluke Ti-25 and a Soligor WT-330A tripod

- The device deployed in field applications is a commercial tripod *Soligor WT-330A*, whose characteristics such as the weight (0.73 kg), height (51.5 cm) and payload (3 kg), enable for its portability.
- Visual (monocular camera) and thermal (infrared camera) environmental features are acquired using a Ti-25 Fluke camera. This camera is mounted on the plate of the tripod, aligned with the vertical axis. Each new frame is stored locally in a 16 GB internal memory card with its respective time stamp.
- Both cameras have been previously calibrated to find the focal point and estimate their main parameters.
- The information extracted is stored locally in a 16 GB internal memory and sent as a data packet at regular intervals to a companion computer to prevent problems occurrence.

  The technical specifications of the proposed system are summarized in Table 3.1.

3.1.1 Sensing system

The acquired data are processed and evaluated in a ground station, where the risky hot-spot cells are identified, and the size of the affected surface is computed. All algorithms

Table 3.1: Technical specifications of sensors and instruments used in this work. (Menéndez et al., 2018) © 2018 MDPI Energies.

Sensor / Instrument	Technical Specifications	
Thermal camera Fluke TI-25	**Infra-red camera**	
	Field of view:	23° × 17°
	Image resolution:	160 × 120
	Infrared spectral band:	7.5–14 μm
	Temperature measurements:	−20 °C to 350 °C
	Thermal sensitivity:	≤0.1 °C at 30 °C
	Accuracy:	±2 °C or 2%
	Weight:	1.2 kg
	RGB camera	640 × 480
	Image resolution	Three levels of on-screen IR blending displayed in center 320 × 240 pixels
	IR Fusion	
Tripod	Tripod Tilt Angle:	From −80° to 90°
	Tripod's plate height:	1 m

presented here were implemented in Matlab R2017a programming environment. The system operation is summarized as follows:

1. The system is exclusively used to perform the visual and thermal inspection of PV-modules and can be used under variable lighting conditions, but not under direct sunlight.
2. The mechanism must be positioned facing the PV-structure at different locations. The distance from the tripod to the structure base and tilt angle of the camera can vary depending on field conditions.
3. The distance of the tripod locations between two consecutive images was empirically computed (about 20 cm), in order to ensure proper performance of the matching algorithm (as stated in [105]).
4. The structure supporting the camera can be moved around the horizontal axis, as shown in Figure 3.2.On the other hand, roll and yaw rotations are blocked on the tripod.
5. The visual and thermal images, from a single location, are merged to obtain a new 2D representation with visual and thermal information. The used thermal camera has a fusion mode, which allows to directly merge thermal and visual images for each location. The latter is important since photovoltaic modules need to be displayed at the proper angle relative to their surface to obtain accurate thermal measurements and reduce the probability of misinterpretations.
6. The proposed two-step algorithm isolates the PV-structure and detects collapsed cells by analysing the visual and thermal information.
7. The PV-module inspection involves storing a merged image (thermal and visual

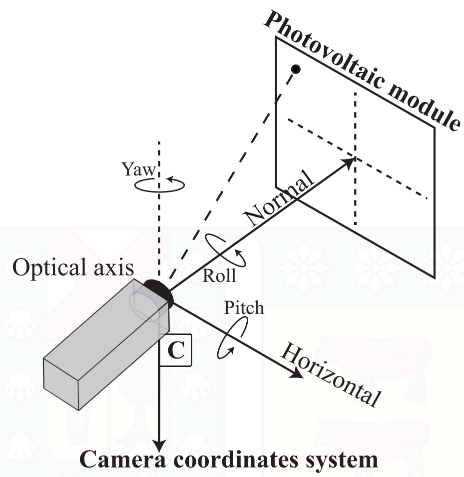

Figure 3.2: Camera model used in this work.

information) of each tranche of PV-structure (between modules), with reference position. In addition, the system returns an inspection report with the location of each hot-spot and the damaged area.

8. Finally, a 3D view, providing thermal and geometrical information of the PV structure, is made available.

3.1.2 Photovoltaic Module Segmentation

The implementation of an efficient segmentation algorithm guarantees the detection and extraction of hot-spots in infrared images, in particular when such hot-spots are not associated with the structure. This section presents the mathematical formulation and thorough analysis of the segmentation algorithms. Figure 3.3 shows the architecture of the proposed module segmentation algorithm.

3.1.2.1 Pre-Processing Images

Lens distortion and noise are two phenomenons that directly disturb the acquired images (both visual RGB and thermal). To measure PV-panel distances in world-units and to compute the camera's position on the environment, these phenomenons must be filtered out. To this end, the algorithm uses the traditional camera calibration method presented in [106]. Furthermore, digital processing algorithms –presented herein– help to reduce the noise and correct image defects, guaranteeing the PV-module detection.

3.1.2.2 Matching Algorithm

Because of the low resolution of the infra-red camera and with the aim of detecting false hot-spots, the PV-module is acquired in different images and in multiple frames. All pre-processed images are then merged. To do this, we implemented the matching algorithms previously published in [105], to get an image with the desired PV-structure. In addition, the system determines the camera's position using Structure From Motion algorithm,

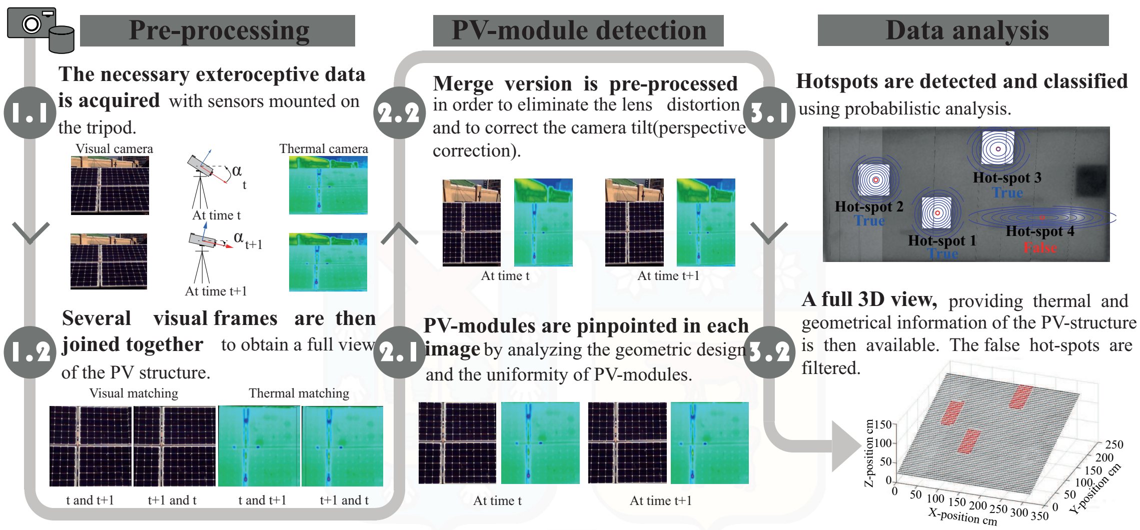

Figure 3.3: Architecture of the segmentation and inspection system of PV-modules. (Menéndez et al., 2018) © 2018 MDPI Energies.

which estimates the 3D structure of a scene from a set of 2D views [101]. Likewise, a pre-processing stage based on Brightness and Contrast Adjustment previously published in [107], improves the PV-module segmentation.

3.1.2.3 Background Filtering

The merged image has additional objects, which are not related to the PV-structure. These objects from the scene must be filtered in order to isolate the PV-modules from the image background. With this goal, the merged image is subjected to two thresholding conditions. First, the color constraint is applied to obtain a gray-scale image. Then, since the PV-module brightness is related to the saturation of the image, it is possible to eliminate all secondary objects by manipulating these parameters. The thresholds are manually defined by evaluating the histograms of the gray-scale image and the saturation image in off-line mode. Finally, the system refines the PV-structure estimation using a filter, which aim is to remove all connected components that have fewer than P pixels. Such parameter, P, is determined off-line and it is related to the module size. This step returns a binary mask associated with the surface of PV-modules.

3.1.2.4 Perspective Correction

The inclination of PV-modules is reflected on the binary mask as a perspective distortion. This phenomena must be considered and corrected to compute the real position of the each detected hot-spot. Homographic mapping method illustrates the relationship between two different views of the same real world scene. Let p and p' be the corresponding projected image points on the image plane of two different views of the same point located in the 3D real world coordinates system, where the coordinates of this pair of matching points in homogeneous form can be respectively denoted as $(x_1, y_1, z_1)^T$ and $(x_2, y_2, z_2)^T$. The homographic mapping is a planar projective transformation, that can be expressed as shown in Equation (3.1) for an homogeneous form. The main challenge is the selection of vectors $[x_1, y_1, z_1]^T$ to compute the homogeneous transformation matrix H:

$$\begin{pmatrix} x_2 \\ y_2 \\ z_2 \end{pmatrix} = \mathbf{H}_{3\times3} \begin{pmatrix} x_1 \\ y_1 \\ z_1 \end{pmatrix}; \mathbf{H}_{3\times3} = \begin{bmatrix} h_{11} & h_{12} & h_{13} \\ h_{21} & h_{22} & h_{32} \\ h_{31} & h_{32} & 1 \end{bmatrix} \tag{3.1}$$

Due to the fact that the system is positioned facing rectangular PV-modules, the proposed algorithm searches for patterns with similar characteristics to module edges on the binary mask. Hough transform can be successfully used to solve this problem, since this method allows to identify the section of the binarized image where high probability of finding straight lines exits (see [108] for further reading). The Hough transform defines a straight line as a co-linear set of points, mapping $\mathbb{R}^2$ into the function space of sinusoidal functions defined by:

$$f : (x, y) \to \rho = x \cos(\theta) + y \sin(\theta) \tag{3.2}$$

where ρ, θ are the perpendicular distance of the line ℓ_i to the center of the coordinates and the angle between the normal of this line and x-axis, respectively. Figure 3.4 illustrates the relation between ρ, θ and line ℓ_i.

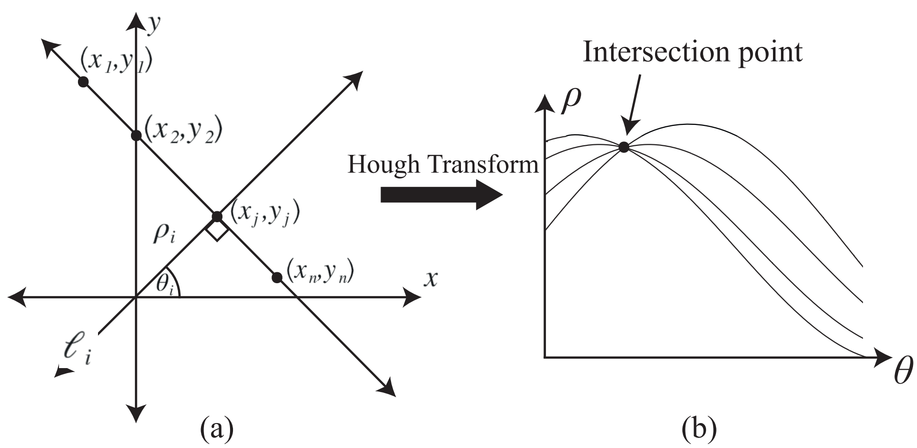

Figure 3.4: Relation of rectangular to polar representation of a line. (**a**) Cartesian axis. (**b**) Hough axis. (Menéndez et al., 2018) © 2018 MDPI Energies.

Hough's parameters (ρ and θ) enable to find the horizontal and vertical metal edges of the PV-module. Since there are several metal edges in the merged image, related to the amount of inspected PV-modules, the algorithm selects those edges that do meet two conditions: (**a**) two horizontal lines, that are parallel and equidistant, and have the maximum separation among them; (**b**) two diagonal lines, that have a slope between $[-30°, -30°]$, are complementary and have the maximum separation among them.

Once the four lines have been detected, the system finds the specific cut points, which are then used for solving the homogeneous transformation matrix. This step returns a binary mask correcting the perspective distortion and the homogeneous transformation matrix.

3.1.2.5 Photovoltaic Structure Refined

Sometimes, the corrected binary mask eliminates a portion of the PV-structure because of the thresholding process. To avoid this, the system uses Normalized Cross Correlation (NCC) to evaluate the similarity between different surfaces of the image with a fixed pattern, which is determined in off-line mode, and it is related to the dimension of the module in an image. The NCC is a cosine-like correlation coefficient, which is defined as:

$$\gamma(u,v) = \frac{\sum_{xy}\left[f(x,y) - \overline{f}_{u,v}\right]\left[t(x-u,y-v) - \overline{t}\right]}{\left\{\sum_{xy}\left[f(x,y) - \overline{f}_{u,v}\right]^2 \sum_{xy}\left[t(x-u,y-v) - \overline{t}\right]^2\right\}^{0.5}} \tag{3.3}$$

where: f is the corrected binary mask; $\overline{t}$ is the mean of the fixed pattern selected; and $\overline{f}_{u,v}$ is the mean of $f(x,y)$ in the region under the fixed pattern selected.

If the value of NCC is closer to 1, then it represents that two images are more similar. Finally, the algorithm returns a refined binary mask with the surface of PV-modules and the number of the analysed PV-modules.

3.1.3 Inspection Algorithm

Once the surface of PV-modules is segmented from the rest of the environment with the previous method, the algorithm detects probable hot-spots using infra-red information provided by the 2D cloud.

3.1.3.1 Temperature Scale Adjustment

The correlation between the PV-module operating temperature T_c and the three basic environmental variables (the ambient air temperature T_a, the air velocity V_f and the incident irradiance flux G) is computed by the following semi-empirical equation [109]:

$$T_c = T_a + \left(\frac{0.32}{8.91 + 2 \times V_f}\right) \times G \qquad \left(V_f > 0\right) \tag{3.4}$$

With this information, the algorithm finds a simple and fast correlation between the expected temperature of each PV-cell, and the measured ones obtained from the field thermographic inspection. The estimated temperature of PV-cell is subtracted from each acquired image, in order to obtain an image with the temperature variation.

The temperature scale adjustment procedure of a thermal image $I_t(x,y)$ (gray-scale mode) can be formulated as follows:

$$I_t = f(I_t, T_c) = \frac{T_{max} - T_{min}}{255} * I_t - T_c \tag{3.5}$$

where (x,y) is the image coordinates, T_{max} and T_{min} are the maximum and minimum temperature of the thermal image respectively and T_c is the estimated temperature of the PV-cell.

3.1.3.2 Hot-Spot Detection

Ideally, the estimated temperature of PV-cell is similar to the temperature provided by the infra-red sensor. In this work, it was empirically determined that a variation of 5 °C induces an abnormal overall temperature pattern, witnessing a potential hot-spot. In addition, this temperature was selected based on the thermal camera accuracy. The algorithm filters all temperatures that are not more than 5 °C, and puts a one in those temperatures that fulfil this condition.

The algorithm clusters the measurements on the raw binary image. To reduce computational time, the algorithm uses an edge detector. Edge detector stage extracts the edges of tentative hot-spots from the rest of the image, and it is based on a combination of contrast adjust and morphological operations. Then, all measurements related to same hot-spot are merged using Fuzzy C-Means algorithm [110] and each characteristic is stored in a matrix of measurements M_t for each time t.

$$M_t = \begin{pmatrix} \overbrace{\quad x_t{}^1 \quad}^{Hot-spot\_1} & \overbrace{\quad x_t{}^2 \quad}^{Hot-spot\_2} & \dots & \overbrace{\quad x_t{}^i \quad}^{Hot-spot\_i} \\ y_t{}^1 & y_t{}^2 & \dots & y_t{}^i \end{pmatrix} \tag{3.6}$$

where $x_t{}^i$ and $y_t{}^i$ are the coordinates of the probable hot-spot in pixels.

Since several hot-spots associated with the same characteristic are detected in different frames, it is necessary to relate the frame $t+1$ to frame t. Therefore, the corresponding points between two sequential images are initially found in order to compute the displacement and the rotation between both images. These points allow for the system to deliver a transformed version refereed to an initial image, which is then analysed in order to detect the probable hot-spots and to create the matrix M_{t+1}. The merging between matrices M_t and M_{t+1} at time t and $t+1$ can be performed using Mahalannobis distance, as shown in Equation (3.8).

$$d = \sqrt{\left(M_t{}^i - M_{t+1}^j\right)^T \Sigma^{-1} \left(M_t{}^i - M_{t+1}^j\right)} \tag{3.7}$$

where $M_t{}^i$ are the coordinates of i-th detected characteristic by the sensor, M_{t+1}^j are the coordinates of j-th previously detected characteristic and Σ is the co-variance matrix of the hot-spot, associated with the j-th previously detected characteristic. The algorithm begins with an empty matrix M_0.

Then, if such distance is greater than an established threshold, the detected characteristic is a new hot-spot. Otherwise, the system merges the detected characteristic with the associated hot-spot. The new mean is defined as:

$$\mu_n = \frac{(n-1) \times \mu_{n-1} + M_t{}^i}{n}$$

where μ_n and μ_{n-1} are the coordinates of the center of the hot-spot for n and $n-1$ detection respectively.

Due to the system mainly searches damaged PV-cells, the threshold is directly determined with the PV-cell width measured in pixels. This parameter is determined in off-line mode.

The new covariance matrix associated with the hot-spot is computed as:

$$\Sigma = \begin{pmatrix} \left(\sqrt{\Sigma^i_{M\langle 1,1\rangle}} + \rho_1\right)^2 & \Sigma^i_{M\langle 1,2\rangle} \\ \Sigma^i_{M\langle 1,2\rangle} & \left(\sqrt{\Sigma^i_{M\langle 2,2\rangle}} + \rho_2\right)^2 \end{pmatrix} \tag{3.8}$$

where $\Sigma^i_{M\langle k,m\rangle}$ is the element (k row, m column) of the covariance matrix of the detected characteristic.

3.1.3.3 False Hot-Spot Extraction

The inspection system detects false hot-spots from reflections by analyzing the statistical behavior of the hot-spots.

Once there are not new measurements related to a previously detected hot-spot, it is necessary to verify if this hot-spot is a consequence of module defects. An internal hot-spot always appears in the same placement in an image, regardless of the camera position. In this work, since the camera moves around the y-axis, false hot-spots will be located in different position on each image. To differentiate between a false hot-spot and a true hot-spot, the system computes the difference between the hot-spot covariance matrix Σ and the covariance matrix of the last hot-spot detection Σ^{last}_M. Frobenius distance is used, as shown in Equation (3.9).

$$d_{mat} = \sqrt{Tr\left(\left(\Sigma - \Sigma^{last}_M\right) \times \left(\Sigma - \Sigma^{last}_M\right)^T\right)} \tag{3.9}$$

If this distance d_{mat} is less than a threshold, which is determined as 10% of the value of the PV-cell width squared, the hot-spot is a consequence of external radiation sources.

3.1.3.4 3D Reconstruction

The suite of images (both RGB and infra-red) must be attached to a common global reference frame, to achieve a complete view of the PV-structure. The system incorporates an algorithm based on image matching methods, perspective correction techniques, norm cross-correlation, and Hough transform to fully characterize the PV-structure. Briefly:

1. The matching algorithm delivers a panoramic view of all PV-structure and the camera's locations for each image respect to the first image.
2. The perspective distortion of the panoramic view is corrected with the homogeneous transformation matrix. The binary corrected mask is applied to this corrected panoramic view, obtaining the photovoltaic surface viewed from a parallel plane.

3. The normalized cross-correlation provides the number of PV-panels in the analyzed images and the location of each PV-module. The algorithm takes advantage of the PV-module shape and determines the width and height of each panel by comparing the distance between boxes determined in the images and the real distances of the PV-module.

4. The algorithm eliminates false hot-spots and replaces their area with the estimated temperature of the PV-cell T_c. Finally, it returns the 3D fully characterization of the PV-structure and the location of the camera.

3.2 Experimental Results

A suite of experiments was conducted in field environments. The experimental part consisted of the acquisition of visual and thermal images from an array with eight PV-modules, under variable lighting and environmental conditions. The thermographic measurements took place in the city of Valparaíso, Chile, by three daily sets, i.e., January 14, 15 and 16 of 2018, under variable sky conditions. Each set included three instant measurements, according to the time: (i) 08:00 hs, power on of modules; (ii) 12:00 hs, steady-state conditions; and (iii) 18:00 hs, power off of modules. To determine the algorithm robustness regarding variations of camera position, the images were acquired at two distances from the PV-structure: at 3 m (on January 14th) and 4 m (on January 15th and 16th). An overview of the recorded environmental conditions is shown in Table 3.2. Ambient air temperature, wind velocity and humidity were obtained by a local weather station and a portable temperature sensor. The solar irradiance flux is measured using a pyranometer. The illuminance values were measured using a conventional luxometer.

Figure 3.5: Proposed architecture to carry out the analysis of the hot-spot detection. (Menéndez et al., 2018) © 2018 MDPI Energies.

Figure 3.5 shows a picture of the tripod facing the PV-structure tested here. The complete system was positioned in front of an array of monocrystalline silicon PV-modules.

The panel dimensions are 1675 mm long and 1001 mm wide. The panel consists of 60 PV-cells (156.75 mm side). To obtain the entire PV-structure, the system was displaced in a straight line path, equidistantly to PV-structure, maintaining the camera plane fixed. Each set consists of the acquisition of 50 images (both thermal and visual). The condition of the tested photovoltaic modules is in proper operating condition. Under this state, four hot-spots were generated in the structure by shading two PV-cells.

Table 3.2: The environmental conditions for the field thermographic measurements. (Menéndez et al., 2018) © 2018 MDPI Energies.

Day	January 14th			January 15th			January 16th		
Hour	08:00	12:00	18:00	08:00	12:00	18:00	08:00	12:00	18:00
Air temp ° C	15	19	16	15.5	18	16	16.5	19	17
Rel. humidity %	78	78	78	78	78	78	78	78	78
Wind speed $\frac{km}{h}$	7.9	10	7.9	9	9	8	8	10	10
Illuminance $klux$	18	24	32	7	22	20	15	24	32
Irradiance flux $\frac{w}{m^2}$	200	980	60	205	977	100	206	960	50

3.2.1 Photovoltaic Module Segmentation

Figure 3.6 presents the resultant images in all four stages of the PV-module detection approach, with regards to: (**a**) Photovoltaic array analysed at 8:00, the system was positioned at 3 m with respect to PV-structure; (**b**) Photovoltaic array analysed at 18:00, the system was positioned at 4 m with respect to PV-structure; and (**c**) Photovoltaic array analysed at 12:00, the system was positioned at 4 m with respect to PV-structure.

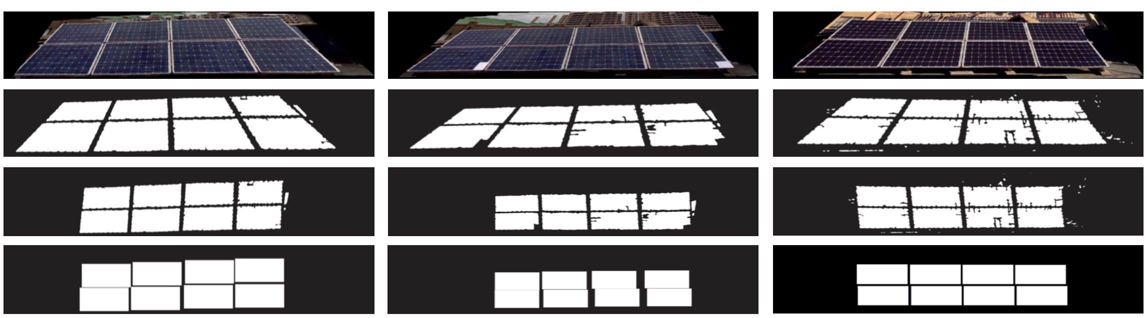

(a) (b) (c)

Figure 3.6: Results of PV-module detection algorithm applied to: (**a**) January 14th, 08:00, d = 3 m; (**b**) January 15th, 18:00, d = 4 m; (**c**) January 16th, 12:00, d = 4 m. (Menéndez et al., 2018) © 2018 MDPI Energies.

Figure 3.6, in all cases, depicts the merged image. The raw merged image is subjected to thresholding condition, which is based on the image saturation and a color filter. The thresholds are determined by analysing the histograms of the gray scale image and the saturation image in off-line mode, as shown in Figure 3.7. For the first case, the usual range for module detection factor is [30, 85], as shown in Figure 3.7a. The usual range of the saturation in this experiments for each analysed image is [0.6, 0.8], as shown in Figure 3.7b.

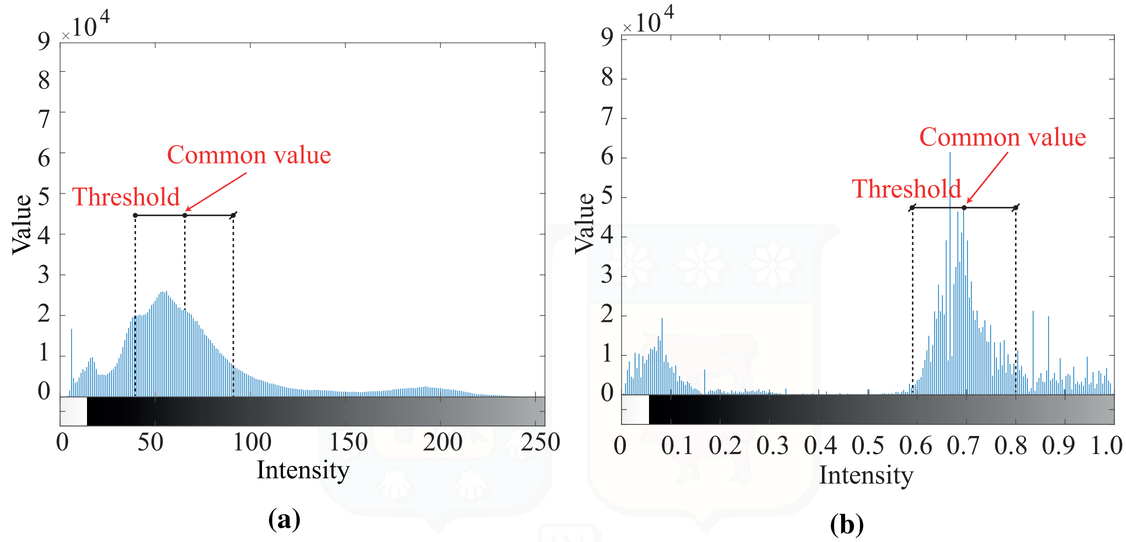

Figure 3.7: Determination of thresholds for binarization of image. (**a**) Histogram of the gray scale image. (**b**) Histogram of the saturation image. (Menéndez et al., 2018) © 2018 MDPI Energies.

The use of Hough transform enables to correct the perspective distortion, as shown in third image row of each case. In addition, this step returns the homogeneous transformation matrix. The segmentation is refined by finding the maximum values in the Normalized 2D cross-correlation, as shown in Figure 3.8. This step provides us the location of each panel in the general image, as shown in Figure 3.9. The resultant images from this stage provide a valuable sum of binary data, overly clear from possible erroneous variation. These data, in the form of the images with the location of each PV-module, constitute the mask of all images.

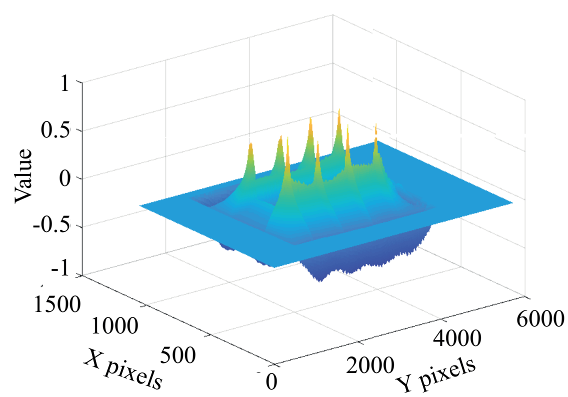

Figure 3.8: 2D cross-correlation between image and external pattern. (Menéndez et al., 2018) © 2018 MDPI Energies.

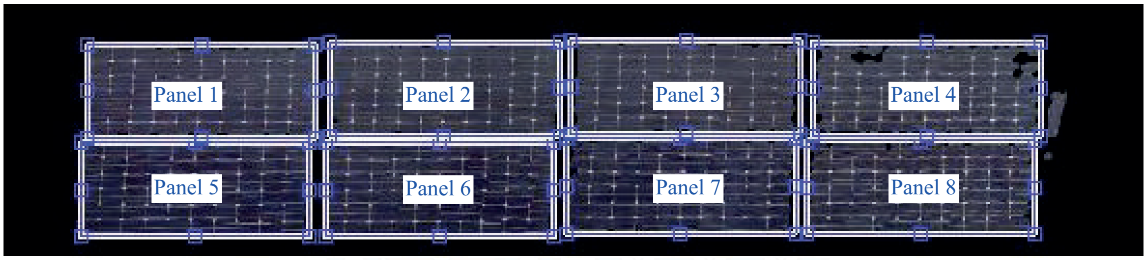

Figure 3.9: Photovoltaic module detection. (Menéndez et al., 2018) © 2018 MDPI Energies.

The PV-surface detection is an important action in order to guarantee the true detection of hot-spots. The algorithm in its first part applies image processing tools and develops a cropped module image with only cell regions, isolating the PV-module from the rest of the environment, as shown in Figure 3.10.

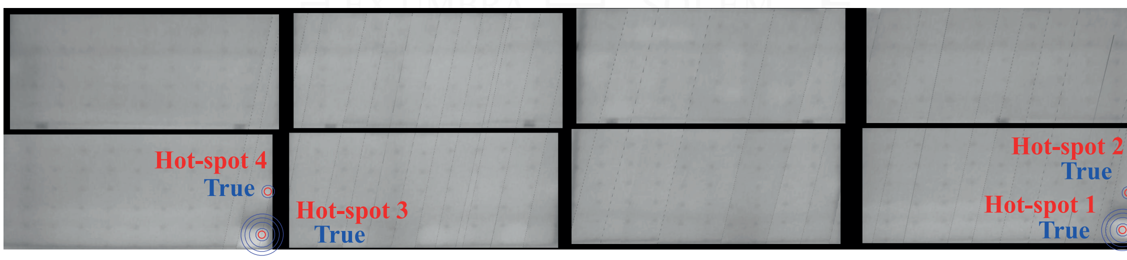

Figure 3.10: Results of the hot-spot detection: The system searches for two hot-spots over the analysed photovoltaic module. The camera is positioned facing the PV-structure at 3 m. (Menéndez et al., 2018) © 2018 MDPI Energies.

Four measures are used to evaluate the obtained results quantitatively. On the one hand, the numbers of correctly detected pixels, either belonging to the object or to the background, are respectively called true positives (TP) and true negatives (TN). On the other hand, the numbers of incorrect detection are, respectively, called false positives (FP) for background pixels included into the object or false negatives (FN) for object pixels included into the background. These different measures are used in the computation of six parameters, two special parameters: Dice coefficient (DIC) and Jaccard index (JCD), as well as the four traditional parameters: precision, sensitivity, specificity, and accuracy.

$$DIC = \frac{2 \times TP}{FP + 2 \times TP + FN} \tag{3.10}$$

$$JDC = \frac{TP}{FP + TP + FN} \tag{3.11}$$

Table 3.3 shows the statistical analysis of the photovoltaic module detection algorithm. It is worth noting that the proposal's accuracy rises up to 96.33% in the best case and 94.05% in the worst case, whereas its precision is 95.93% and 92.86% for the best and worst case respectively.

Table 3.3: Statistical analysis of photovoltaic module detection algorithm. (Menéndez et al., 2018) © 2018 MDPI Energies.

Day	**January 14th**			**January 15th**			**January 16th**		
Hour	**08:00**	**12:00**	**18:00**	**08:00**	**12:00**	**18:00**	**08:00**	**12:00**	**18:00**
Precision %	95.80	**95.93**	95.59	94.90	94.91	94.44	93.53	**92.86**	93.05
Accuracy %	95.59	96.31	**96.33**	95.05	95.22	95.02	94.56	94.10	**94.05**
Sensitivity %	**97.60**	98.61	**99.01**	97.68	97.93	98.15	98.40	98.68	98.13
Specificity %	91.54	**91.84**	91.13	90.07	90.11	89.16	87.54	**86.39**	86.59
DIC %	96.71	97.25	**97.27**	96.27	96.39	96.26	95.90	95.54	**95.52**
JCD %	93.63	**94.69**	94.68	92.81	93.04	92.79	92.13	91.46	**91.43**

3.2.2 Hot-Spots Detection

Once the system isolates the PV-modules from the rest of the environment, the algorithm identifies the position of hot-spots on each PV-module. Four hot-spots were generated in the PV-structure by shading two cells, which generated a temperature change in the cell surface and two punctual hot-spot above of each one. The results of hot-spot detection are shown in Figure 3.10. It is possible to see that the covariance matrix –coloured circles– is maintained constant when the system detected a true hot-spot, and it wraps the area of the hot-spot. In addition, the mean value of the estimated hot-spot –red circle– was approximately located in the center of the real hot-spot.

As previously mentioned, the performance of the algorithm is analysed through four measures: the number of correctly detected pixels belonging to TP, TN, FP and FN. These different measures are used in the computation of three parameters: precision, sensitivity and accuracy. The statistical analysis for each experiment is shown in Table 3.4. It is possible to note that the algorithm is able to detect surfaces affected by hot-spots with a precision of 98.0% and accuracy of 97.1% in the worse cases respectively.

Table 3.4: Statistical analysis of hot-spot detection algorithm. (Menéndez et al., 2018) © 2018 MDPI Energies.

Day	**January 14th**			**January 15th**			**January 16th**		
Hour	08:00	12:00	18:00	08:00	12:00	18:00	08:00	12:00	18:00
Precision %	96.52	96.1	95.5	95.9	95.92	**96.55**	96.24	95.23	**95.12**
Sensitivity %	94.21	94.32	94.67	94.01	94.05	**93.04**	93.11	**95.21**	95.13
Accuracy %	95.24	**94.19**	94.58	94.52	95.58	**96.12**	95.41	94.88	95.86

3.2.3 False Hot-Spots Detection

Three hot-spots associated with the linear edge shunt (see [111]) in a monocrystalline photovoltaic module are simulated to evaluate the system's performance. Likewise, one false hot-spot is generated in the PV-surface using an external radiation source, as shown in Fig. 3.11. Data acquisition consisted on taking thirty visual and thermal images in order to completely scan the PV-module. The complete system was located facing the PV-structure at a distance of approximately one meter to ensure that the cameras acquired all PV-module in each frame. This distance was determined by performing a first scan and then manually verifying that the entire PV-module was acquired on each frame. The angle between to ground and PV-module planes is approximatly 80°, in order to generate the false hot-spot associated with the external source radiation used.

Figure 3.11: Proposed architecture to carry out the analysis and detection of false hot-spots. (Menéndez et al., 2018) © 2018 MDPI Energies.

Initially, each acquired image was pre-processed using the photovoltaic module detection algorithm. Figure 3.12 shows the results of the fusion algorithm and the results of the hot-spot detection algorithm. It is possible to note that the covariance matrix –color circles– is maintained constant when the system detected a true hot-spot, and it wraps the area of the hot-spot. In addition, the mean value of the estimated hot-spot –red circle– was approximately located in the center of the real hot-spot. On the other hand, it is possible to note that the covariance matrix increased for false hot-spots, wrapping a greater area than the area of detected hot-spot. In this case, the mean value of estimated hot-spot was located outside of the real hot-spot.

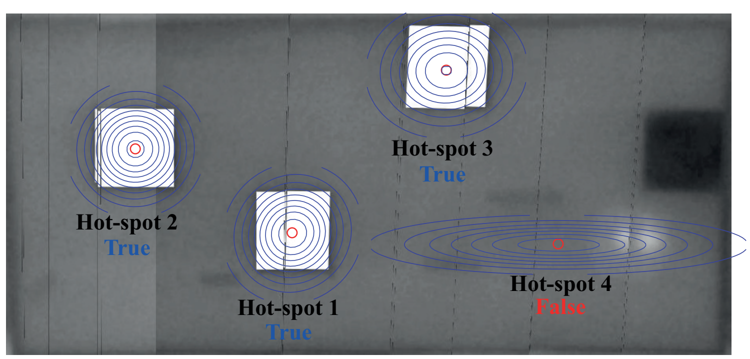

Figure 3.12: Results of the hot-spot detection: The system searches five hot-spots over the analyzed photovoltaic module. (Menéndez et al., 2018) © 2018 MDPI Energies.

The fault diagnostic of each detected hot-spot is shown in Table 3.5. The system returns the location of each hot-spot respect to upper border of PV-module, the damaged surface and the reason the possible failure.

Table 3.5: Estimated values of detected hot-spots. (Menéndez et al., 2018) © 2018 MDPI Energies.

Hot-Spot	Mean mm	Covariance mm^2	Damaged area mm^2	Main Reason
1	$(440, 568)$	$\begin{pmatrix} 4305 & -142 \\ -142 & 4580 \end{pmatrix}$	13950	Damaged cell
2	$(275, 255)$	$\begin{pmatrix} 4622 & -381 \\ -381 & 4263 \end{pmatrix}$	13945	Damaged cell
3	$(113, 873)$	$\begin{pmatrix} 5255 & -89 \\ -89 & 4449 \end{pmatrix}$	15190	Damaged cell
4	$(460, 1101)$	$\begin{pmatrix} 34542 & 17 \\ 17 & 873 \end{pmatrix}$	17252	External radiation source False hot-spot

3.2.4 3D Reconstruction

The system provides the 3D visual and thermal reconstruction of PV-modules, as shown in Figure 3.13, which offers a complete morphological characterization of each PV-module.

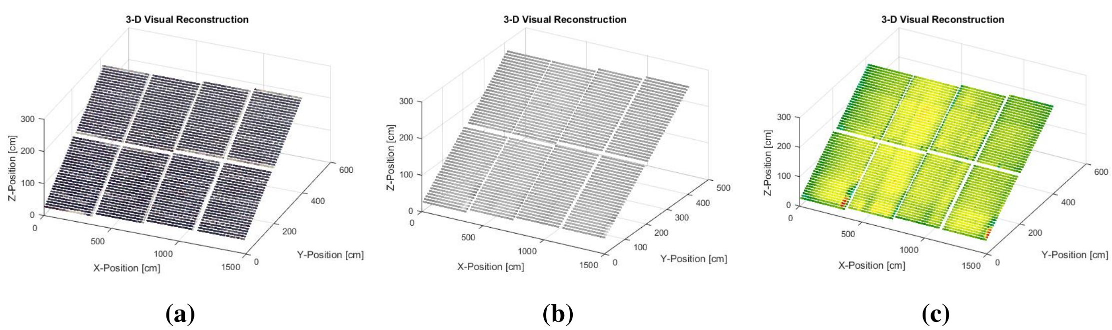

Figure 3.13: Full 3D thermal reconstruction of a photovoltaic module. (**a**) Visual reconstruction. (**b**) Thermal reconstruction (Gray scale mode). (**c**) Thermal reconstruction (High contrast mode). (Menéndez et al., 2018) © 2018 MDPI Energies.

If the system detects false hot-spots, the surfaces associated with false hot-spots are replaced with average temperature from PV-module in good condition. Figure 3.14a,b respectively show the results of 3D-thermal reconstruction with and without false hot-spots.

3.2.5 Comparison with existing approaches

Three different techniques are proved [112, 113, 114]. in order to evaluate the effectiveness of the proposed system against other previously published. However, the contrasting methods have two limitations: (i) they extract manually the regions of interest (PV-modules). Hence, it is necessary to apply the PV-module segmentation algorithm with these techniques;

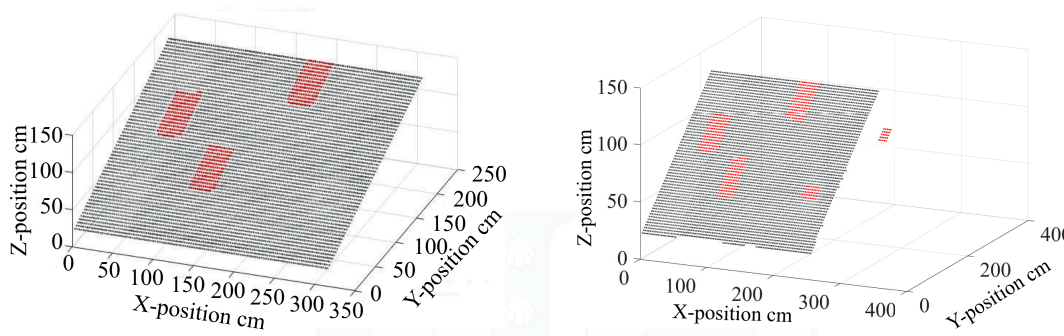

(a) **(b)**

Figure 3.14: Full 3D thermal reconstruction of a photovoltaic module. (**a**) Without false hot-spots. (**b**) All hot-spots detected by inspection system. (Menéndez et al., 2018) © 2018 MDPI Energies.

(ii) the three methods cannot detect false hot-spots, they are limited to true hot-spots. The three methods are evaluated with the metrics described previously. The comparison is shown in Table 3.6

Table 3.6: Statistical analysis of hot-spot detection algorithm. (Menéndez et al., 2018) © 2018 MDPI Energies.

Method	Proposed System	Color Segmentation and k-Means	LPA and IHA	Canny Edge Detector
Precision %	96.52	84.06	91.38	92.18
Sensitivity %	94.21	82.56	92.67	91.09
Accuracy %	95.24	86.75	92.53	90.54

It is worth noting that there is a 12% increase in the algorithm precision with respect to other existing methods, improving the thermal monitoring of the PV structure. Furthermore, an attractive characteristic of the system described in this chapter is the capacity of filtering the false hot-spots automatically. In addition, the system has a particular characteristic that makes it more attractive for industrial applications: its detection time is less than 2.7 s, which compared to other methods has significant improvements (e.g., the algorithm based on color segmentation [112] took 25 s).

3.3 Contributions

This chapter put forward and experimentally assessed a PV-module fault diagnosis algorithm based on infra-red thermography. The algorithm consists of two-stages: PV-module segmentation and PV-module inspection. Concerning the PV-module detection algorithm, the system was capable of finding the PV-module with a precision of 92.86% and an accuracy of 94.05% in the worst case. On the other hand, the system had a precision of 95.12% and an accuracy of 94.19% in hot-spots detection. In addition, our system was capable of filtering false hot-spots due to the analysis of hot-spot position in each frame and the proper segmentation provided by the detection algorithm. Experimental results showed that the quality of the output depends on the accuracy in the classification and segmentation of the module in the RGB camera readings and the thermal image, respectively. Misclassification produced due to the mixed pixels problem could lead to incorrect conclusions about the thermal status. This work pushed forward some artificial vision methods applied to the exploitation of information provided by different sensors. Table 3.7 summarizes the main contribution of the proposed systems, comparing with other methods analyzed.

Table 3.7: Potential benefits of the proposed system. (Menéndez et al., 2018) © 2018 MDPI Energies.

Task	Proposed system	Color Segmentation and k-Means	LPA and IHA	Canny Edge Detector
Hot-spot detection	Very High	Medium	High	Very High
False hot-spots detection	Automatically	—	—	Manually
Computational cost	Low	Medium	Medium	Low
Hot-spot resolution	High or Very high (limited by camera's accuracy)	Low	Medium	Medium
Photovoltaic module detection	Yes	No	No	No
Can be mounted on a robot?	Yes	No	No	Yes

The publication derived from the research work presented in this chapter is:

- O. Menéndez, M. Pérez and F. Auat Cheein, "Photovoltaic Modules Diagnosis Using Artificial Vision Techniques for Artifact Minimization," Energies, 2018, 11, 1688. doi: 10.3390/en11071688. **Impact Factor:** 2.676

Chapter 4

VISUAL NAVIGATION SYSTEM FOR POWER-LINE FOLLOWING

This chapter describes the development and implementation of a transmission lines detection system, focusing on autonomous drone flight. The system extracts geometric patterns associated to the transmission line design and based on such patterns, it is possible to obtain the position and attitude of the aerial platform, allowing to locate the drone over an electric network without using GNSS receiver. A novel two-stage visual navigation algorithm is proposed which can be mounted on any manual, teleoperated or robotic platform due to its flexibility. The transmission detection is an important action in order to guarantee the positioning of the platform. In this context, the algorithm in its first part applies image processing tools and develops a cropped power grid image, isolating the power-lines from the rest of the environment. An important challenge is related to perspective distortion, the system addresses this issue using texturing filtering and perspective correction algorithm. In addition, texturing filtering can simultaneously remove the background noise of power lines as well as generate edge maps. Hough transform is applied to edge maps in order to detect straight lines in images that can be related to power-lines. Finally, the system determines power-lines by taking advantage of the regular characteristics of power lines. Additionally, the system uses the prior information of platform position in order to reduce the computational cost and to improve the power line detection. The second stage determines the distance to wires and the robot position using Bayesian methods. The system merges sensor information (IMU and GNSS) with visual information provided by our system using Maximum Likelihood Estimation. This information would allow the equidistant flight over the transmission lines.

This chapter is organized as follows: Section 4.1 present in details the methodology, hardware and software to test the positioning algorithm; Section 4.2 shows the results obtained when tested the proposed approach on transmission lines under different environmental and lighting conditions. Finally, Section 4.3 summarizes the contributions of the case studies presented in this chapter.

4.1 Experimental Setup

A drone with six rotors was designed, implemented, and tested for the autonomous inspection of transmission lines, as shown in Fig. 4.1a. The robotic platform can be described in general terms as follows:

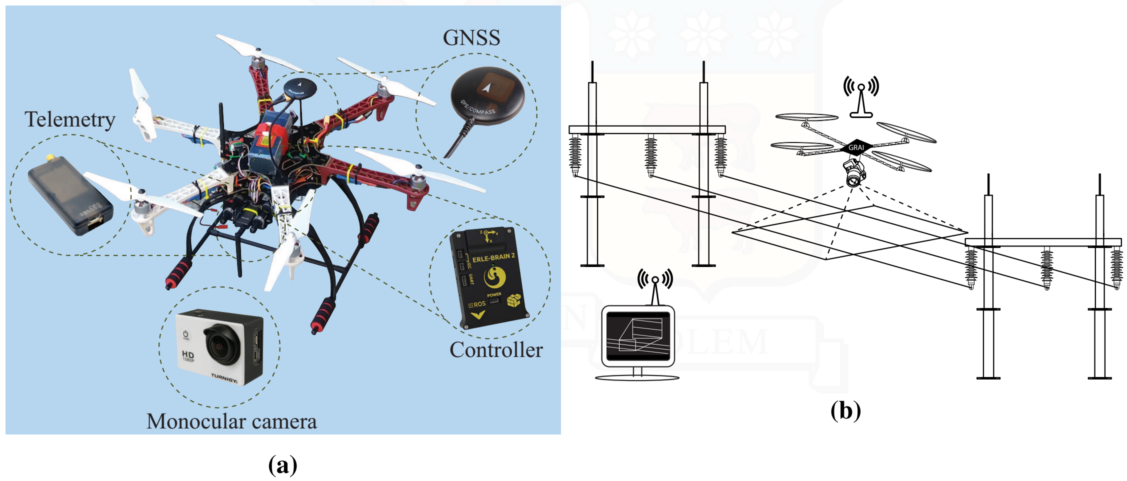

Figure 4.1: Unmanned aerial vehicle used for inspection of transmission lines. **(a)** Hardware. **(b)** Methodology. (Menéndez et al., 2019) © 2019 MDPI Applied Science.

- The drone deployed in real applications has a flight controller (Type Erle Brain 2 with a 900MHz quad-core ARM Cortex-A7 CPU processor), which has a flight control unit - a computer that provides basic flight controls and a companion computer - computational system in charge of image processing and image broadcasting. Additionally, the controller has an inertial measurement unit (IMU), an integrated altimeter and an embedded Kalman Filter for the treatment of signals. The UAV also has a GNSS antenna with an absolute error of 1 meter.

- Visual data is acquired with the SJ4000 Turnigy HD ActionCam 1080P Full HD video camera. According to the manufacturer, the visual camera in TV mode has a resolution of 1920×1080 pixels.

- The monocular camera has been previously calibrated to find the focal point and to estimate its parameters. Additionally, the camera is aligned with a gimbal that compensates the fast dynamic rotation of the hexacopter and controls the image plane to stay horizontal and parallel to power-lines. This process is essential for smooth target tracking in the image. The visual information is sent to a computational device that is in charge of higher-level behaviors, in an embedded form, such as the image processing and image broadcasting.

- The information extracted is stored locally in a 16 GB internal memory and sent as a data packet at regular intervals to a companion computer to prevent problems occurrence. In order to perform this process, the drone is equipped with a communication system based on a transmitter/receiver 433 MHz and WIFI connection

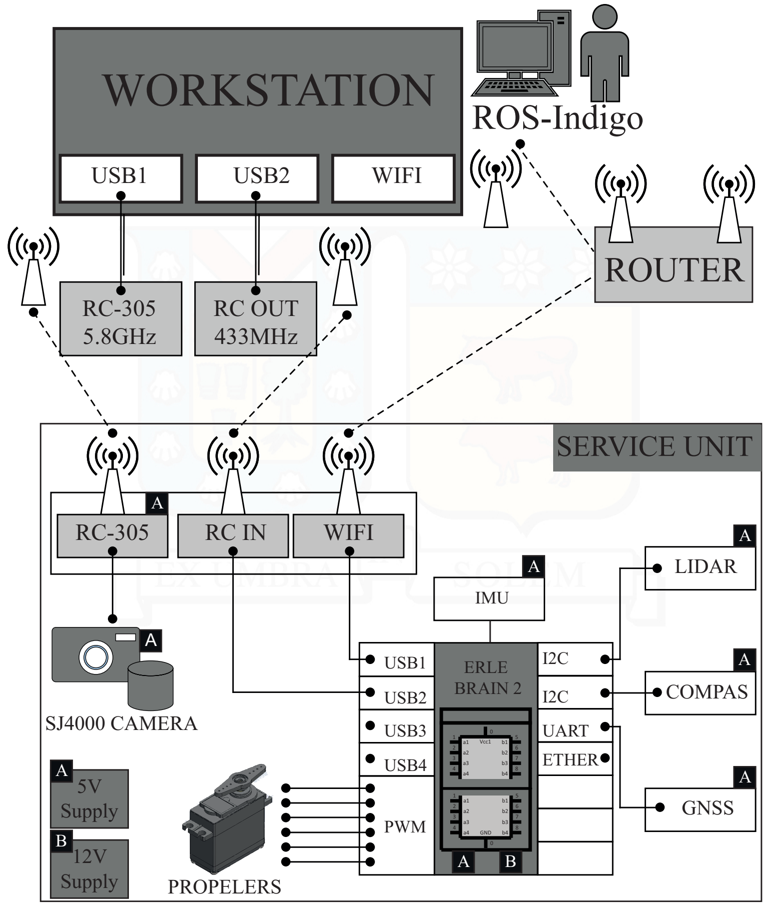

Figure 4.2: General diagram of the hardware developed in the robotic platform. (Menéndez et al., 2019) © 2019 MDPI Applied Science.

employed for telemetry operations, and transmitter/receiver 5.8 GHz employed for image broadcasting.

- The UAV works with the Robot Operating System (ROS-Indigo) [115], adapted to the specifications of this problem.

The general scheme of the sensory and processing system embedded in the UAV is shown in Fig. 4.2.

4.1.1 Sensing System

The proposed visual-based positioning system enables to locate and maneuver a commercial drone over a transmission grid. As shown in Fig. 4.1b, in the proposed approach the UAV acquires visual images of the conductors using a monocular camera and sent each image to a ground station. The system position is estimated and the navigation commands are send back to the UAV in order to maintain the position respective to the transmission lines.

1. The UAV is manually positioned over a transmission grid. The distance from the UAV to conductors varies depending on the safety, lighting conditions and camera

characteristics; requiring at least 1 m between the conductors and the vehicle.

2. The exteroceptive information is acquired with a monocular camera, which is mounted at bottom of the UAV.

3. To avoid the direct incidence of sunlight, a two axis hand-held gimbal changes the camera vision point to avoid sensor saturation.

4. The positioning process computes the placement of the camera based on conductors geometric design. Furthermore, the system is able to store a compressed image, with geo-referenced information as a backup and as support to future inspection work.

5. The latest version for the positioning system only performs the flight over three-phase transmission grids with conductors approximating straight lines without interruption. Its operating system is flexible in order to add other features. The system is able to detect transmission lines with other distribution using Hough transform variations due to the fact that the system takes advantage of geometric patterns.

6. The navigation process around transmission lines consists of two stages: (i) Power-line detection (ii) Electrical tower detection. Our visual positioning system is focused on the first goal. Hence, the system is automatically disabled when the UAV is near an electrical tower, changing to manual mode. The maximum speed is 75 $\frac{km}{h}$. In this chapter, the velocity is limited to 25 $\frac{km}{h}$ in order to increase the probability of power-lines detection and to reduce blurring effects.

7. The flight autonomy of the drone is18 minutes (empirically determined). If the drone detects a low-energy level of its batteries, the vehicle selects between two flight modes: land (attempts to bring the UAV straight down) or return to the launch (the UAV navigates from its current position to hover above the home position), depending on the distance to the starting point.

8. The drone performs inspection tasks along a length of about 10 km in one-hour intervals (Battery charging time).

9. The proposed drone operates in a dry ambient, ideally at a standard environment of 20 °C and 50 % humidity. However, the aerial platform can be also placed on rugged ambient, whose temperature shall not be less than 5 °C or more than 40 °C and whose humidity shall not be more than 80 %. The apparatus cannot be directly exposed to rain and it is capable of facing wind gusts of up to 10 $\frac{km}{h}$.

4.1.2 Visual-based positioning system

This section presents the mathematical formulation of the proposed positioning algorithm. The algorithm consists of three stages: image pre-processing, transmission line detection and spatial positioning of the UAV, summarized in Fig. 4.3.

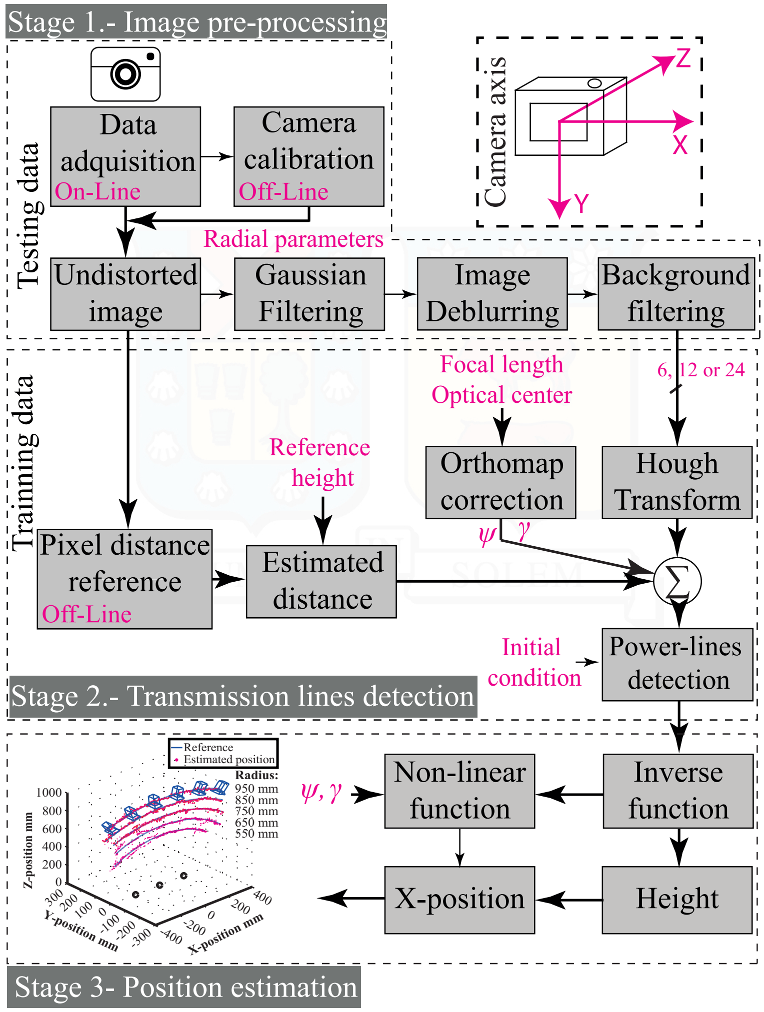

Figure 4.3: Processing architecture of the power-lines detection system. (Menéndez et al., 2019) © 2019 MDPI Applied Science.

4.1.2.1 Image pre-processing

Lens distortion and the noise directly disturb acquired images, decreasing the detection of power conductors on these. Therefore, the system must be capable of filtering out these phenomena in order to measure the separation between conductors in world units and to determine the drone's location in the work-space. With this aim, traditional camera calibration method estimates the intrinsic and extrinsic parameters and distortion coefficients, while the digital signal processing algorithms -presented herein- reduce the noise, correct image defects and remove blurry distortion, guaranteeing the transmission lines detection [116].

On the other hand, each pre-processed image has several extra objects, which are not related to the transmission grid. These objects from the scene must be attenuated or removed, or otherwise, the system must be intensified the pixels related to the transmission lines, in order to isolate the three-phase transmission lines from the image background. With this goal, the image is subjected to anisotropic Gaussian filtering [117], that improves the texture quality of transmission lines and remove irrelevant data, regardless of line location in the image, as well as their length and slope.

The filter bank consists of an edge filter, at 6, 12 or 24 orientations and one scale $\left(\sigma_x, \sigma_y\right) = (1, 3)$. The orientations are selected based on the computational time and the image size. The resulting image in each filtering process is filter with the Sobel detector, in order to intensify the edges and to obtain a binarized version with the probable power wires. The system delivers a tensor with 6, 12 or 24 binarized images.

A fixed pattern in the transmission grid, mainly on its conductors, is the symmetric geometric design. The system looks for patterns with similar characteristics to conductor in each binarized image. In this work, the UAV flies over transmission grids with conductors approximating a straight line, without interruption. Hough transform can be successfully used to solve this problem, since this method identifies the section of the binarized image where high probability of finding straight lines exits [108].

The Hough transform defines a straight line as a co-linear set of points, mapping $\mathbb{R}^2$ into the function space of sinusoidal functions defined by:

$$f : (x, y) \rightarrow \rho = x\cos(\theta) + y\sin(\theta) \tag{4.1}$$

where ρ, θ are the perpendicular distance of the line ℓ_i to the center of the coordinates and the angle between the normal of this line and x-axis, respectively.

In this context, the algorithm returns a data set with all lines (ρ_i and θ_i), that meet with previous specifications related to the geometric design of the transmission grid for each binarized image. Then, all measurements related to same line are merged using Fuzzy C-Means algorithm.

4.1.2.2 Transmission line detection

Transmission lines detector uses the geometric design and uniformity of transmission lines to establish the power wires in each image. At this stage, the purpose is to find a set with three or more straight lines, that fulfill with parallelism and equidistance of transmission lines. Using the parameters ρ (the distance between the line and the origin) and $\tan(\theta)$ (slope), that are provided by Hough transform, it is possible to prove these conditions. However, topographic relief and camera tilt disturb the equidistant line recognition process, as shown in Fig. 4.4a. These negative events were corrected using an image orthorectification process.

The image orthorectification process corrects the adverse effects using the geometric relation between different angles and known distances, such relation is displayed in Fig. 4.4b, where each parameter is described as follows:

- α_1, α_2 is the angle between the real point of the power-line and focal point;
- γ is the draft angle of the camera around $x-$axis;
- ψ is the field of view (FOV);

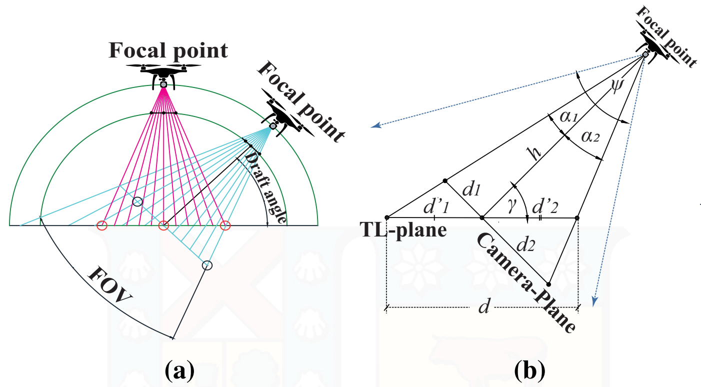

Figure 4.4: Analysis of the camera attitude -including the main angles for mathematical expressions. **(a)** Effect of the topographic relief and the camera tilt in the acquisition of images. **(b)** Necessary angles for orthogonal correction. (Menéndez et al., 2019) © 2019 MDPI Applied Science.

- d_1 and d_2 are the distorted distances measured in pixels between power-line in the center and power-line left and right respectively;
- d, d'_1 and d'_2 are the real distances measured in pixels between transmission line phases, when the camera plane is parallel to power-lines plane;

Using geometry, it is possible to solve this problem and to compute the distance d'_1 as a function of d_1 as:

$$d'_1 = d_1 \times \left(\frac{\cos(\gamma)}{\tan(\gamma - \alpha_1)} + \sin(\gamma) \right) \tag{4.2}$$

and d'_2 as function of d_2 as:

$$d'_2 = d_2 \times \left(\frac{\cos(\gamma)}{\tan(\gamma + \alpha_2)} + \sin(\gamma) \right) \tag{4.3}$$

The system acquires several images at fixed height h_{ref} above the transmission lines in order to determine the relation between image units and world units. In this chapter, power wires are manually extracted in each image, and the separation between them is directly measured in the image. The estimated reference distance $\hat{d}$ is determined using a consistent estimator of the mean. This will ensure to determine the measurement of the separation between power wires and help us to determine the drone position, as shown in the next section.

4.1.2.3 Estimation of the position based on visual data

The estimated height is determined by applying an inverse linear function that relates the measured distance, the reference distance and reference height to the camera height. The height is defined as:

$$\hat{h} = \frac{h_{ref} \times \hat{d}}{d'_1 + d'_2} \times \sin(\gamma); \tag{4.4}$$

where:

- $\hat{h}$ is the estimated drone height to transmission lines;
- h_{ref} is the reference height;
- $\hat{d}$ is the reference distance in the image in number of pixels;

As explained above, during off-line mode is established the reference separation $\hat{d}$. Hence, it is possible to compute the x-position and y-position of the camera in relation to the center-line transmission system as:

$$\hat{x} = \frac{\hat{h}}{\tan(\gamma - \alpha)} \times \cos(\delta) \tag{4.5}$$

$$\hat{y} = \frac{\hat{h}}{\tan(\gamma - \alpha)} \times \sin(\delta) \tag{4.6}$$

where:

- $\hat{x}$, $\hat{y}$ is the estimated x-position and y-position of the camera in relation to the center power conductor, respectively;
- δ is the rotation angle of the camera around the z-axis;

Visual-based positioning cannot be applied if the transmission lines are not visible since any outcome can be returned by the system under such circumstances. However, the robotic platform has two additional sensors (IMU and GNSS receiver), with different probability density functions (*pdf*), estimating the spatial positioning of the UAV. This information can be used with any Bayesian method to estimate the system placement. With this aim, in this work was implemented the maximum likelihood estimation [118], associating a Gaussian probability density function to each sensor. The corresponding analysis presented in (7) and (8), reveals that the new estimation $\hat{\theta}$ is a weighted average and the new uncertainty ${\sigma_\theta}^2$ can be generated through addition of the reciprocals:

$$\hat{\theta} = \frac{z_1{\sigma_2}^2{\sigma_3}^2 + z_2{\sigma_1}^2{\sigma_3}^2 + z_3{\sigma_1}^2{\sigma_2}^2}{{\sigma_1}^2{\sigma_2}^2 + {\sigma_2}^2{\sigma_3}^2 + {\sigma_1}^2{\sigma_3}^2} \tag{4.7}$$

$${\sigma_\theta}^2 = \frac{{\sigma_1}^2{\sigma_2}^2{\sigma_3}^2}{{\sigma_1}^2{\sigma_2}^2 + {\sigma_2}^2{\sigma_3}^2 + {\sigma_3}^2{\sigma_1}^2}$$

$${\sigma_\theta}^{-2} = {\sigma_1}^{-2} + {\sigma_2}^{-2} + {\sigma_3}^{-2} \tag{4.8}$$

where z_i is the measurement of each sensor and ${\sigma_i}^2$ denotes its variance (in this work, the parameters z_1, ${\sigma_1}^2$ are related to IMU, z_2, ${\sigma_2}^2$ are related to GNSS and z_3, ${\sigma_1}^3$ are related to our system).

4.2 Experimental Results

A set of experiments were conducted in laboratory, simulation and field environments. The proposed approach was simulated using the GAZEBO software [119] and linking this with ROS [115] and MATLAB [120]. Finally, field tests in private facilities, in the Valparaiso Region, Chile were carried out.

4.2.1 Laboratory validation

A scale model 1:8 of a three-phase distribution system with power-lines, approximating a straight line and without interruption was used in the laboratory validation. The model was wrapped with camouflage at the bottom to simulate the different objects which could be found in a transmission grid environment. The UAV movement was simulated by a KUKA robotic arm model KR-6.

Laboratory experiments were conducted in the *Centro Integrado de Manofactura y Automatización* (CIMA) at the Universidad Técnica Federico Santa María, located in Valparaíso, Chile. The procedure can be summarized in six main steps:

1. The positioning system was mounted in the clamp of robotic arm to simulate the UAV attitude.
2. The parameter reference separation by the acquisition an image set (30 images) at a fixed attitude in off-line mode was proposed.
3. The operator set up the robot height with respect to wires of the model, and the path to be followed by the robot.
4. The robotic arm automatically moves on the pre-determinate path, recording a video sequence.
5. Visual data was analyzed in MATLAB programming environment (MathWorks, USA). The robotic arm position provided by the software from the manufacturer was used as the reference in each experiment.
6. The estimated placement of the camera was shown in a graphical user interface (GUI).

Three experiments were carried out to prove the algorithm behavior: straight line path, circular path, and circular variable path. Figure 4.3 shows schematics of experiments developed in indoor tests.

The first experiment consisted of moving the positioning system in a straight line path at three different heights, maintaining the camera plane fixed and parallel to the power-lines plane, as shown in Fig. 4.5a. A database with 600 visual images was analyzed to

Table 4.1: Transmission line parameters in GAZEBO environment. (Menéndez et al., 2019) © 2019 MDPI Applied Science.

Parameter	Transmission Line 500 kV
Height	20 m
3ϕ-Separation	10.50 m between phases
Distribution	Horizontal

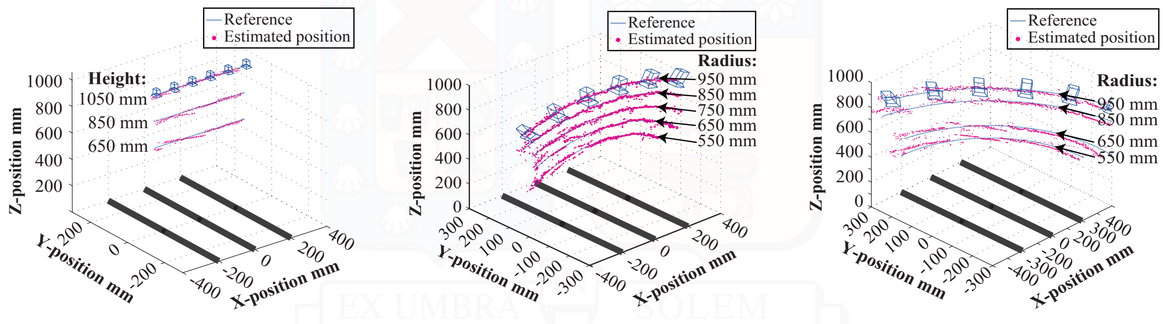

(a) (b) (c)

Figure 4.5: Laboratory results: Comparative analysis between pre-established path and estimated path by our approach (blue boxes represents the spatial position of the camera). **(a)** Straight line path. **(b)** Circular path. **(c)** Circular variable path. (Menéndez et al., 2019) © 2019 MDPI Applied Science.

investigate the behavior of the positioning system in each trail. It is possible to observe that the camera positioning –magenta dots– converges to the reference –blue dots– in Fig. 4.5a for each studied height. In terms of the root medium squared error (RMSE), our approach was within this tolerance limit for this type of applications [121, 122]. Furthermore, The algorithm accuracy was higher than 90.35% in the three-phase system detection, as shown in Table 4.2.

Table 4.2: Statistical analysis of different developed experiments: Straight line path. (Menéndez et al., 2019) © 2019 MDPI Applied Science.

Height mm	650	850	1050
Analyzed frames	600	600	600
True positives	543	575	573
Accuracy %	90.35	95.67	95.53
RMSE mm	18.94	13.81	10.30

The second experiment consisted of moving the positioning system in a circular path. The camera plane rotated around the power-lines plane, as shown in Fig. 4.5b. The second set of data acquired from the visual sensor allowed to analyze the accuracy and reliability of relative positioning from five different radius by processing more than 1000 visual images in each trail. Results of absolute positioning are shown in Fig. 4.5b where the blue line is the height reference and the magenta line is the camera positioning and the statistical analysis is tabulated in Table 4.3. Moreover, the algorithm accuracy was higher than 78.5% in the three-phase system detection.

Table 4.3: Statistical analysis of different developed experiments: Circular path. (Menéndez et al., 2019) © 2019 MDPI Applied Science.

Height mm	650	850	1050
Analyzed frames	600	600	600
True positives	543	575	573
Accuracy %	90.35	95.67	95.53
RMSE mm	18.94	13.81	10.30

Finally, an experiment, called circular variable path, was developed. This test gathers the first two cases, as shown in Fig. 4.5c. The camera plane rotates around the power-lines plane as it is not aligned with the power-lines direction. It is interesting to note that the camera positioning, in magenta color, converges to its reference in blue color and positioning errors were within expected and suitable ranges for this application, as shown in the statistical analysis developed in Table 4.4. The algorithm accuracy was higher than 90.4% in the three-phase system detection.

Table 4.4: Statistical analysis of different developed experiments: Circular variable path. (Menéndez et al., 2019) © 2019 MDPI Applied Science.

Radius mm	550	650	850	950
Analyzed frames	1003	1143	1247	1174
True positives	973	1061	1128	1093
Accuracy %	96.9	92.7	90.4	93
RMSE mm	58.81	60.97	59.32	47.12

4.2.2 Simulation results

Gazebo software was used to study the behavior of a simulated UAV, equipped with our system. The working environment consisted of three-phase transmission grid, whose main characteristics are summarized in Table 4.1, a simulated UAV and a simulated visual camera. In addition, the pre-calibrated algorithm was programmed in C/C++ under Ubuntu 16.04 operating system, in order to reduce the processing time. The procedure can be summarized in three main steps:

1. First, the parameter reference separation by the acquisition an image set (30 images) at a fixed attitude in off-line mode was proposed.

2. Then, the simulated UAV automatically flies on the pre-determinate path, acquiring the visual data.

3. Finally, our approach analyzed the data and returned the estimated placement of the UAV in real time. At the same time, the results were plotted in a GUI, developed in MATLAB programming environment.

Two experiments were developed in the simulated environment. First, the UAV attitude was maintained all the time. The corresponding results are shown in Fig. 4.6a. It is possible to see that the estimated placement converges to the simulated configuration and the absolute error of the positioning system was less than 1%.

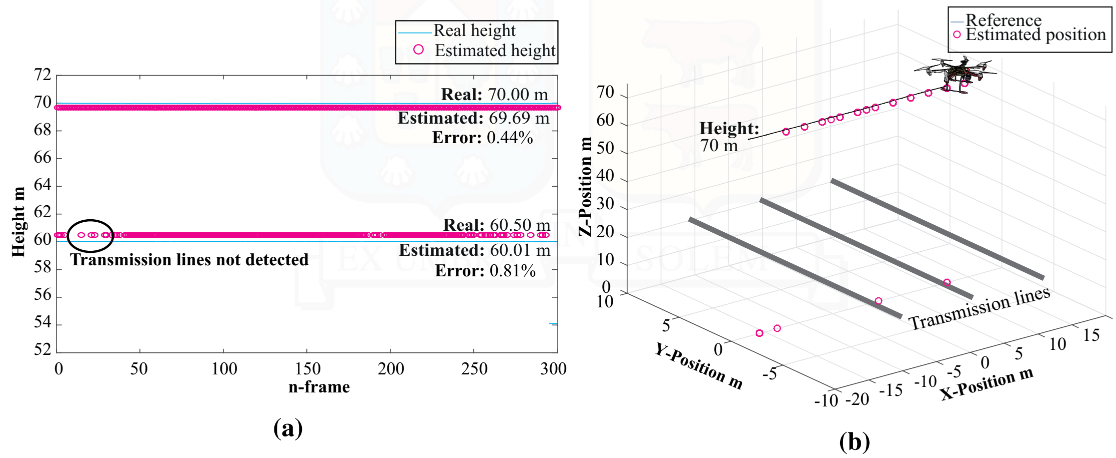

Figure 4.6: Results of the simulation: **(a)** Stationary flight of the UAV (flight altitude: 55 m, 60 m and 70 m to conductors) with frames where transmission lines were not detected; **(b)** Comparative analysis between pre-establish path and estimated path by our approach (Straight line path). (Menéndez et al., 2019) © 2019 MDPI Applied Science.

Under the same conditions, the simulated UAV was maintained at constant height and flew it over the simulated transmission lines, as shown in Fig. 4.6b. It is possible to see that the estimated placement converges to the simulated configuration, provided that the transmission lines are visible in the analyzed images. Otherwise, the system is able to delete the false estimations, providing better performance.

4.2.3 Transmission line detection algorithm

Each acquired image has additional objects, which are not related to the transmission lines. These objects from the scene have to be filtered or eliminated to isolate the conductors. First, the color constraint is applied to obtain a gray-scale image. Then, the image brightness is corrected to highlight power conductors. Finally, the delivered image is filtered using Gabor filters, that simultaneously remove the background noise of power lines as well as generate edge maps. It is worth noting that the system highlights power conductors. However, the delivered image is noisy due to complex and irregular ground coverage. This disadvantage increases the risk of the positioning system returns erroneous measurements. Figure 4.7 shows resultant images in each stage of the transmission line detection approach, regarding: (**a**) Images are analyzed under ideal lighting conditions; (**b**) The image brightness is increased in 20%; (**c**) The image brightness is increased in 60%; and (**d**) The image brightness is reduced in 50%.

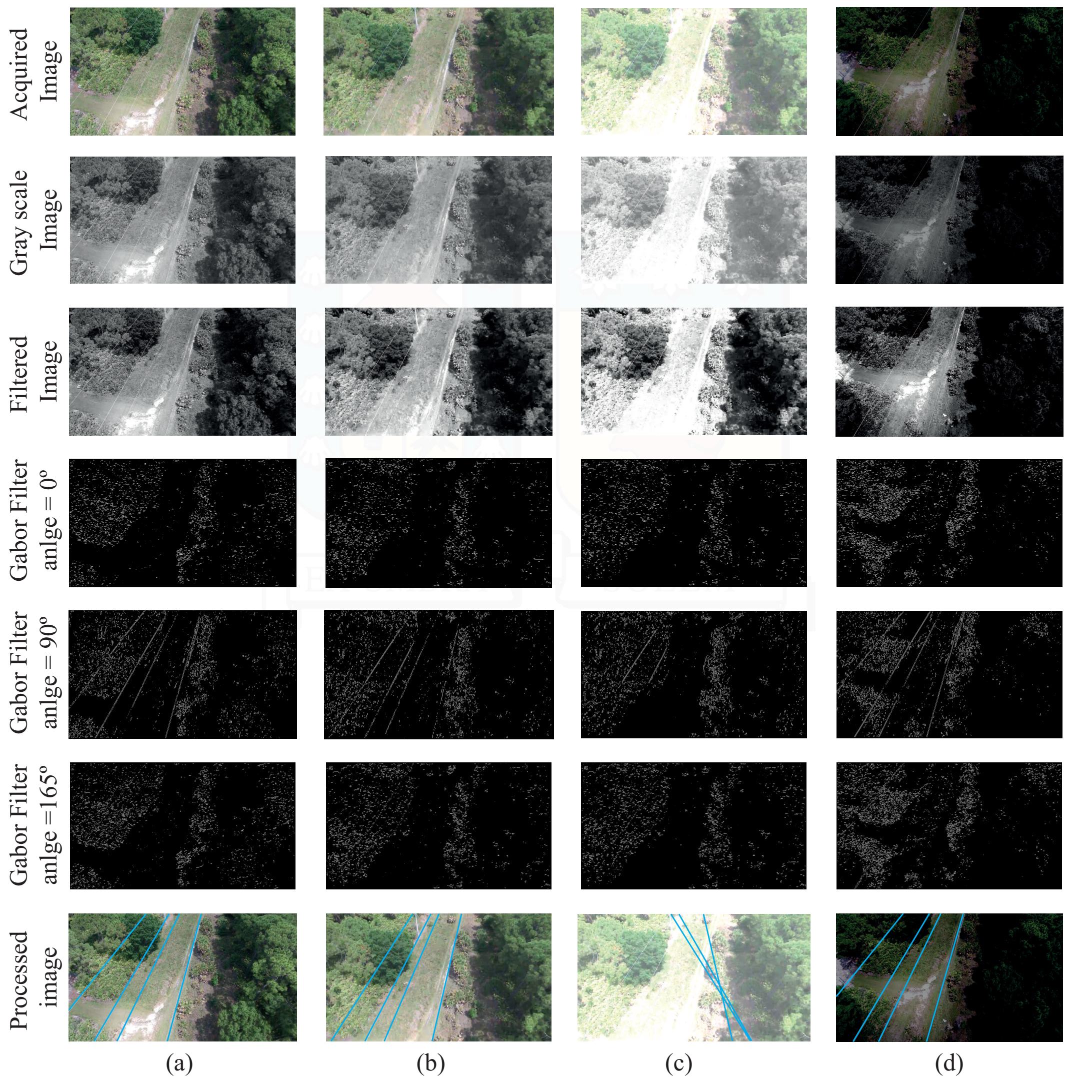

Figure 4.7: Comparison of power line detection results **(a)** Ideal lighting conditions; **(b)** Brightness increase of 20%; **(c)** Brightness increase of 60%; and **(d)** Brightness reduction of 50%. (Menéndez et al., 2019) © 2019 MDPI Applied Science.

The direct bright sunshine can affect the positioning system, due to the system could not detect wires and conductors, as shown in Fig. 4.7b and Fig. 4.7c. Therefore, the system is not able to find and isolate power-lines in the image. On the other hand, the system can operate under reduced visibility conditions but no in darkness, as shown in Fig. 4.7d.

4.2.4 Field experiment results

The positioning system was mounted on a commercial UAV (HJ-5000), and equipped by the UTFSM Robotics Research Group (GRAI). The complete system was positioned over a transmission system, which main parameters are summarized in Table 4.5. The estimate based on the embedded Kalman Filter was used as a position reference of the UAV. The corresponding results are shown in Fig. 4.8a and Fig. 4.8b. It is interesting to note that the estimated position shown as a magenta dashed line, converges to reference in black line, provided that the transmission lines are visible in the acquired images, as shown in Fig. 4.8a and Fig. 4.8b. Otherwise, the system compensates poor estimations using Bayesian methods. In this context, the estimator described in 4.7 and 4.8 is applied to reduce this negative effect. Table 4.6 compares the results obtained in the position estimation, after applying two approaches: simple when the system returns the position and hybrid when the sensor fusion expression only with the IMU, GNSS, and our approach data.

Table 4.5: Structural characteristics of the transmission grid. (Menéndez et al., 2019) © 2019 MDPI Applied Science.

Parameter	Transmission Line 68 kV
Height	12 m
3ϕ-Separation	2.4 m between left and right wire 1.6 m between left and center wire 0.8 m between right and center wire
Distribution	Horizontal

The impact of this solution is shown in Fig. 4.8a and Fig. 4.8b, as a cyan dashed line, where it is worth noting that the system determined the UAV position in the hybrid case despite not seeing wires, giving the robustness to the system. In terms of the RMSE, the two approaches show similar results although the hybrid method proposed here is slightly smaller and the positioning errors were respectively less than 66.02 cm (x estimation) and 26.29 cm (z estimation) in the simple case and 25.77 cm (x estimation) and 10.26 cm (z estimation) in the hybrid case. Results shows a proper behavior for aerial applications. On the other hand, the algorithm accuracy was 91.44% in three-phase system detection. These findings show that the system serves to locate any robotic platform in a transmission grid, under variable lighting conditions or GNSS restrictions.

4.2.5 Consistency test

Consistency tests following the guidelines presented in [123], were performed to evaluate the visual based transmission line positioning system. Figure 4.9 shows the consistency of the estimation of the x and z coordinates of the drone flying over the transmission lines, in Figs. 4.9a and 4.9b, respectively. As can be seen, the error in both coordinates remains bounded by two times its standard deviation. The data acquired by the GNSS

Table 4.6: Field results: Statistical analysis of different developed experiments. (Menéndez et al., 2019) © 2019 MDPI Applied Science.

Frames	True Positives	False Positives	Efficiency	RMSE X Estimator m	RMSE Z Estimator m
549	502	47	91.44%	0.2577	0.1026

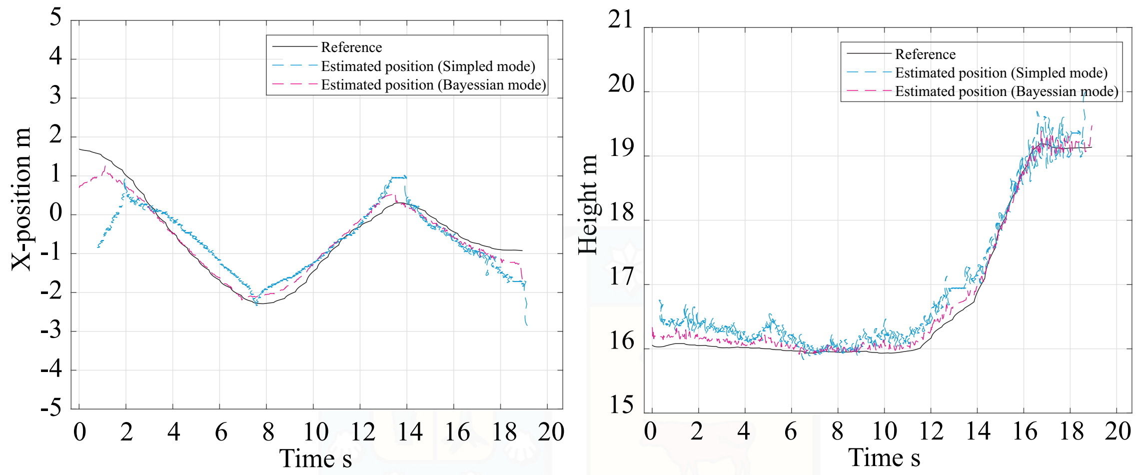

(a) (b)

Figure 4.8: Field results: **(a)** Positioning of our UAV over transmission grid: X-position; **(b)** Positioning of our UAV over transmission grid: Z-position (height). (Menéndez et al., 2019) © 2019 MDPI Applied Science.

positioning system described in Section 4.1 was used as ground truth (and only with the aim of performing the consistency tests).

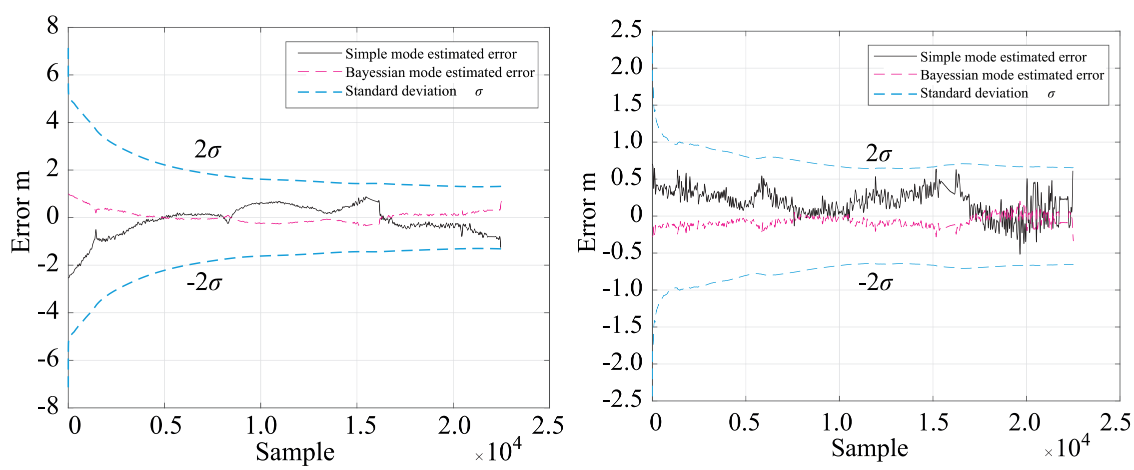

(a) (b)

Figure 4.9: Consistent tests. Figure 4.9a shows the consistency of the error in the x coordinate, whereas Fig. 4.9b shows the consistency of the error in the z coordinate. (Menéndez et al., 2019) © 2019 MDPI Applied Science.

4.3 Contribution

Aerial remote sensing based on unmanned aerial vehicles is a promising and emerging alternative to develop inspection task in power systems. Robotic platforms can be used for monitoring of electrical equipment, as a result of the ergonomics, flexibility, and reliability, of the new platforms and their high availability to access in inhospitable areas. This chapter put forward some artificial vision methods applied to the exploitation of information provided for the different sensors. Likewise, the performance of a low-cost visual positioning system for aerial platforms was analyzed and tested. The experimental findings show that the location accomplishes a high precision with respect to transmission lines, achieving 1.5 centimeter and 27 centimeters are the worse cases in laboratory and field tests, respectively. Further, the system can operate under different lighting conditions and on GNSS-denied areas. The proposed system was tested over a distribution grid located in the agriculture environments due to the irregular surface is an imperative challenge for vision-based systems. Although results are very promising, there is still some test to be performed in order to have a complete guarantee. It is worth noting that experiments showed a very proper performance in the platform positioning, behaving similarly in all experiments and within expected and suitable ranges for this application. Although the system was specially designed for UAVs, its operating system is flexible to add on other platforms since it did not depend on the platform type.

The publications derived from the research work presented in this chapter are:

- O. Menéndez, M. Pérez and F. Auat Cheein, "Visual-Based Positioning of Aerial Maintenance Platforms on Overhead Transmission Lines," Applied Science, 2019, 9, 165. doi: 10.3390/app9010165; **Impact Factor:** 1.689
- O. Menéndez, M. Pérez and F. Auat Cheein, "Vision based inspection of transmission lines using unmanned aerial vehicles," 2016 IEEE International Conference on Multisensor Fusion and Integration for Intelligent Systems (MFI), Baden-Baden, 2016, pp. 412-417. doi: 10.1109/MFI.2016.7849523
- O. Menéndez, M. Pérez and F. Auat Cheein, "Vision based inspection of transmission lines using unmanned aerial vehicles," 3rd International Seminar on Energy Management in Mining, Santiago-Chile, 2016, chapter 3.

Chapter 5

MAXIMUM ELECTRIC FIELD ENERGY HARVESTING

As stated in Chapter 1, the monitoring of complex dynamical behavior of power systems is based on a hybrid system that merges two leading technologies: robotics and smart-sensor nodes. Robotic platforms are used to perform the routine inspection of electrical assets. On the other hand, smart-sensor nodes measure the critical variables of the power system in real-time. Smart-grid (SG) technologies include a suite of operation and energy measures that enable a deeper distributed generation diffusion, encourage the introduction of renewable energies and afford improved management of loads with storage ability such as electric vehicles [124]. The smart-grid concept contains a large number of distributed sensor nodes at different levels: power layer (generation, storage, and converters), electronic layer (sensors, smart meters, communication systems) and data link and transport layer (control, optimization, management of the generation/demand). In this regards, SG sensors stand as promising devices for continuous monitoring of power system vital parameters (e.g. voltage, current, power flows and temperature) and for the detection and diagnosis of failures [15]. In particular, transmission line (TL) sensors enable to assess the condition and status of transmission system components, such as power conductors, insulators, guard cable, and other assets. However, to energize these large number of nodes is an important task in order to guarantee the proper and autonomous operation of sensors. In this context, energy harvesting systems are a robust, simple and cost-effective energy source to power these nodes.

To complement the robotic inspection and the applications described before, this chapter describes a novel, non-contact option for electric field energy harvesting, which takes advantage the capacitive coupling (parasitic capacitance) between energized wires and a metallic electrode in low-voltage applications. The system is designed to power smart-sensors nodes that can be mounted on both the power-line or robotic platforms. However, although the electric field induction on objects in proximity to energized conductors at power frequencies is a cost-effective power supply, the power output is very low. In this context, electric field harvesters require the design of ultra-low power logic circuits, efficient power management circuits that are able to extract the maximum power available out of the energy harvesters, and optimal coupling designs that are capable of increasing the induced power. Hence, a low-power design methodology to reduce power dissipation and to increase the harvested power has to be implemented, considering the electric field scarcity in household applications and a variety of challenging design issues.

This chapter is presented as follows: Section 5.1 presents a comprehensive review of energy harvesting technologies used in power systems, with special emphasis on electric field energy harvesting. The main conclusions from this section are: **(i)** electric field energy harvesting is a particularly attractive option for energy scavenging either low (homemade) and high(transmission lines) voltage applications; **(ii)** the goal of electric field harvester is to efficiently extract energy from transmission lines or energized wires. Section 5.2 presents the demonstration and validation of the proposed technique, focusing on the optimization of the harvested power. The theoretical analysis identifies specific loading and operating conditions that allow maximum power transfer. Likewise, it analyses the basic requirements to extract the maximum power available out of the energy harvesters using different power electronic converters. Section 5.3 explores the feasibility of increasing the power available by modifying the geometric design of the harvester. In addition, it presents a new two-plate harvester prototype capable of maximizing the extracted power of the harvester by varying the separation of the electrodes and using a maximum power point tracking algorithm. Finally, Section 5.4 summarizes the contributions of the case studies presented in this chapter.

5.1 Energy Harvesting Sensor Nodes

Nowadays, smart-grid (SG) technologies enable a deeper distributed generation diffusion, encourage the penetration of renewable energies and provide improved management of loads with storage ability such as electric vehicles [124]. A general smart-grid architecture basically comprises of three main layers: the application layer, the power layer, and the communication layer [124]. Figure 5.1 shows the components of all of the smart-grid layers. Briefly, each stage can be defined as follows,

1. *Application Layer:* It includes advanced applications providing inter-operability among different stages of power systems. This layer operates and manages the technical and commercial functioning of a power system, as well as, interconnections between power systems, under security, top-quality and minimal cost standards.

2. *Power Layer:* Two important advantages of the SG concept are related to the integration of renewable energy sources in a power system and the bidirectional flow of information between power companies and customers. A smart-grid aims to mitigate the impact of penetration of renewable energy sources in a traditional power system, guaranteeing maximum power system's standards (quality, reliability, stability, and security). On the other hand, a two-way communication between the customer and the utility enables to find an optimal balance between demand and the available power.

3. *Communication Layer:* It is the heart of the SG system by providing interconnections between all of the systems and devices of the mains. The communication layer

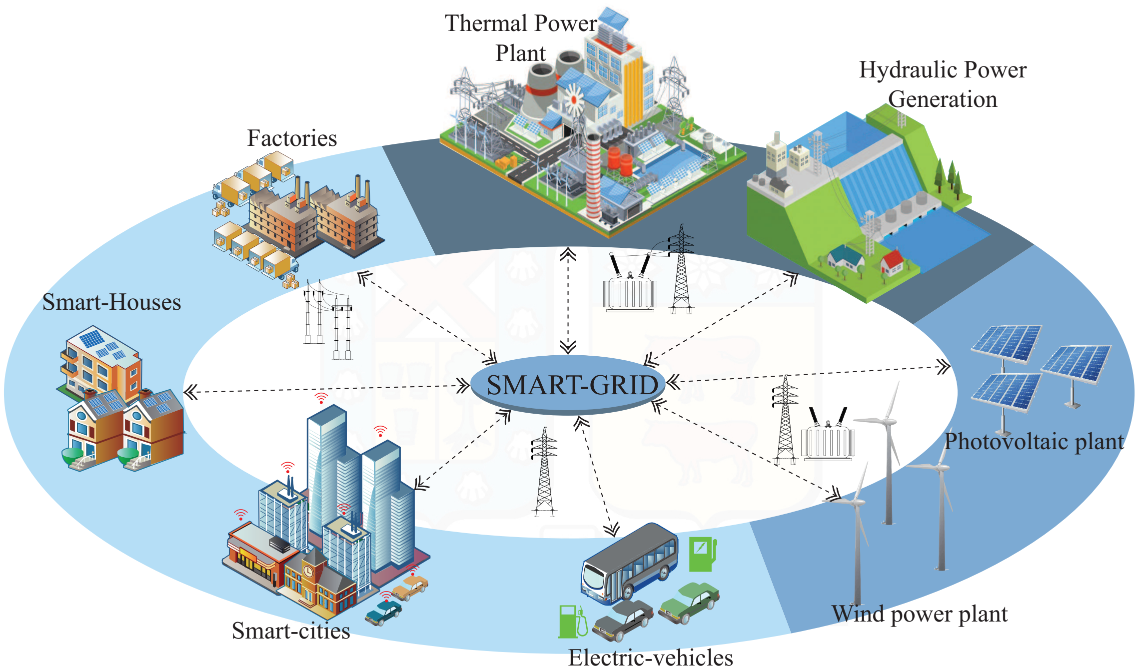

Figure 5.1: Robotic technology applied in power systems for maintenance tasks.

consists of three transmission categories: wide-area (WAN), field-area (FAN), and home-area (HAN) networks. Wide-area networks provide bidirectional communication between power generators and substations. Further, they deliver the information on high-voltage transmission lines. Field-area networks analyze the behavior of the power distribution systems. Finally, home-area networks help to optimize the customer's electricity consumption.

Information and communication technologies (communication layer) represent a fundamental element in the growth and performance of SGs. Smart-grid concept contains a large number of distributed sensor nodes at different levels: power layer (generation, storage, and converters), electronic layer (sensors, smart meters, communication systems) and data link and transport layer (control, optimization, management of the generation/demand). Smart-grid sensor nodes with wireless communication are promising and emerging devices, which enable a more reliable and safe grid and ensure high quality and reliability of electric power supplied to commercial and industrial customers. In this regards, SG sensors stand as sophisticated security mechanisms for continuous monitoring of power system vital parameters (e.g. voltage, current, power flows, temperature, etc.) and for the detection and diagnosis of failures [15].

Smart-grid sensor nodes consist of an embedded system, a power supply, and a wireless communication device for data transmission. Figure 5.2 shows the basic structure of a sensor node used to monitor transmission lines, which is energized with an electric field energy harvesting system. Typically, these sensors are used to sense and collect data for application specific analysis. To ensure the integration between power grid infrastructure and advance communication infrastructure, sensors should be deployed in the order of

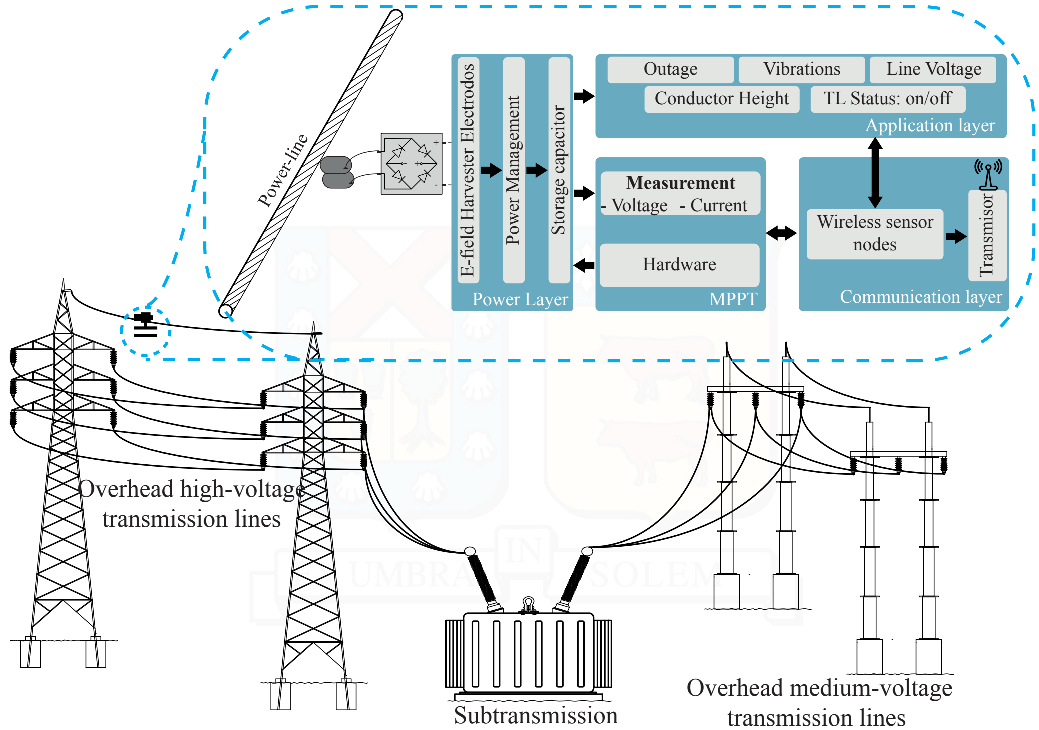

Figure 5.2: Practical model diagram of EFEH sensor nodes deployed on the overhead power lines.

thousands. In this context, the development of economic, portable, lightweight and self-sustainable sensors is a necessity.

An important objective of the SG concept is related to the reliability, flexibility, efficiency, economic, and secure power use, focusing on the improvement of the sensor autonomy and reduction of the human interaction [124]. The availability of large power supplies could be an adequate solution to develop auto-sustainable sensors. However, it is dangerous and inefficient due to the increment of the sensor weight and size, and usage constraints in several environments. In this context, harvesting methods based on heat [125, 126], electromagnetism [127, 128, 129], and kinetic energy [130] have emerged as a viable solution to run sensors autonomously. Energy harvesting refers to harnessing energy from the environment and converting it to electrical energy. Despite the fact that those energy harvesting methods have highly improved in terms of cost, autonomy, and flexibility, the supplied power might not be continuous, and its magnitude may vary strongly depending on ambient factors, and the harvesting method.

5.1.1 Existing Energy Harvesting Techniques

The energy source performance can be evaluated according to the design parameters, power density, controllability, and predictability [131]. Design parameters concern dimensions, weight, and materials of the harvester. These parameters are important due to the fact that transmission line design specifications limit the ability to assemble a sensor node. The power density enables to determine if a potential harvestable source is able to supply

Table 5.1: Comparison of energy harvesting methods

Type	Power Density	Characteristics	Advantages	Disadvantages
Mechanical [130, 132, 133]	375 $\mu W/cm^2$	TL power, uncontrollable, unpredictable	Integrated system, high power density, environmental, continuous output	Complex materials, charge leakage, highly variable power
Thermal [125, 134, 135]	50 $\mu W/cm^2$	Ambient power, TL power, uncontrollable, unpredictable	Environmental, low maintenance	Low efficiency, complex modeling, limited availability, grid dependent
Solar [126, 136, 137]	10-100 $\mu W/cm^2$	Ambient power, uncontrollable, predictable	High power density, continuous output, independent of the grid, simple modeling	Low efficiency, brittle materials, limited availability, storage unit needed
RF waves [138, 139, 140, 141]	0.3 $\mu W/cm^2$	TL power, partially controllable	High availability, allows mobility, reliable	Distance dependent, low power density, impractical modeling, fluctuating density
M-field [142, 143]	150 $\mu W/cm^3$	TL power, fully controllable	High power density, compact configuration, easy implementation	Depends on current flow in the conductor, direct contact, requires of a decou_ pling system
E-field [144, 145, 128, 142]	0.02-26 $\mu W/cm^3$	TL power, partially controllable	High availability, allows mobility, voltage dependent, can be in contact or not with the conductor	Distance dependent, corona discharge, design constrains, depends on the grid

continuous energy to a load. Furthermore, harvesting sources are broadly categorized as uncontrolled and predictable, uncontrolled and unpredictable, fully controllable and partially controllable in this work. By regarding this separation and the frequency of preference, some leading harvesting technologies are discussed, and a detailed comparison is shown in Fig. 5.3 and the main characteristics are summarized in Table 5.1.

5.1.1.1 Mechanical Energy Harvesting

The vibrational harvesters use one of three methods: piezoelectric, electrostatic or micro-generator to convert mechanical vibrations to electrical energy.

- Piezoelectric method - is based on the vibration of piezoelectric transducer due to the low-level vibrations in a power system. Harvesters can be integrated on a chip due to compact configuration and simple design. In addition, harvesters have a high output impedance, that enables to provide continuous output power, about 375 $\mu W/cm^2$ [130, 146]. However, this method has a fluctuating power density due to high variations of the low-level vibration in a power system.

- Micro-generators - are inductive spring-mass systems that take advantage of Faraday's

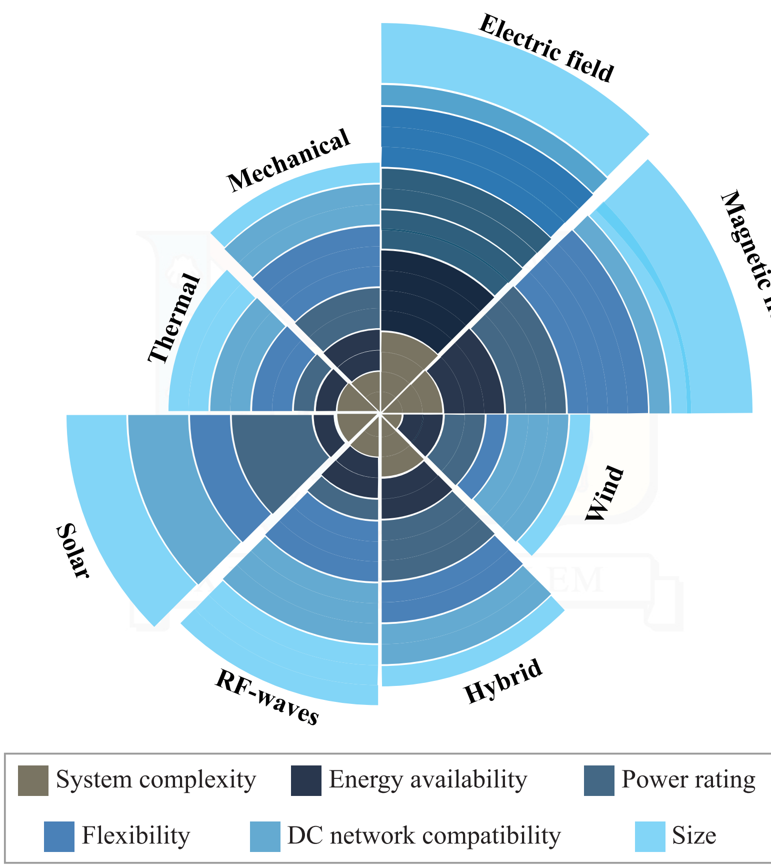

Figure 5.3: Comparison of the existing harvesting technologies

law (electromagnetic induction). The harvester consists of a magnet attached to a spring inside a coil. The power grid vibrations stimulate the magnet, entailing an induced voltage in the coil. The limited voltage below 100 mV is an important constraint [147].

- Electrostatic generation - relies on changing the capacitance of a vibration dependent variable capacitor. Micro-electromechanical systems (MEMS) function with this principle [147].

  The harnessed energy can be defined by,

$$E_H = \frac{1}{2}Kx^2 \tag{5.1}$$

where K is the stiffness-constant and x is the displacement of the harvester.

5.1.1.2 Thermal Energy Harvesting

Thermo-generators are harvesters that scavenge the energy due to the temperature difference [146]. In power system environments, these harvesters take advantage of the heat flux between the power line and environment. The power density in reported wireless sensor node applications is approximately 50 $\mu W/cm^2$. However, the Carnot cycle enforces an important constraint to the maximum efficiency at which energy can be harvested from a temperature gradient. The efficiency decreases substantially for small temperature gradients [146]. This is a fundamental limitation since in the mild-weather the temperature differences in conductors will not exceed 10 °C [148]. Moreover, the harvesting source reliability is not guaranteed because this method is strongly dependent on environmental conditions, and predicting the temperature patterns is impractical.

5.1.1.3 Solar Energy Harvesting

Photovoltaic panels convert sunlight into electricity. This harvesting method is characterized by a high power density (10-100 $\mu W/cm^2$) and a reduced complexity. These outstanding characteristics make them an ideal tool to power autonomous field devices [146, 126]. Furthermore, the optimization of the energy harvesting process is possible, due to the fact that harvester models are highly accurate, and the predictive errors can be reduced using environmental parameters [126]. However, these harvesters have very low efficiency (8-16%) and are highly dependent on sunlight conditions [130]. Since the system can only supply power to a load while there is sunlight, the harvesting system should be equipped with a storage unit in order to provide sustainable energy during a day [136]. In addition, harvesters need an additional circuit in order to provide sustainable power to load systems (Harvesters cannot connect directly to load).

5.1.1.4 Electromagnetic Wave/RF Energy Harvesting

The growing of global systems for mobile communications (GSM) and the increase of wireless devices in both rural and urban areas, indoor and outdoor, have influenced the development of RF-waves harvesters, called rectenna [146]. The power density of electromagnetic waves is given by

$$W = \frac{\mathbf{E}}{Z_r} \tag{5.2}$$

where $\mathbf{E}$ is the value of the electric field and Z_r is the radiation resistance of the free space (377 Ω). Although these systems offer adequate solutions in terms of complexity and availability, harvesters show low energy density (about 0.3 $\mu W/cm^2$) and directly depends on distance to transmitters. Besides, the maximization of harvested energy is a complex task since a large number of electromagnetic sources are present in the environment, preventing system modeling [138, 139, 140, 141].

5.1.1.5 Magnetic Field Energy Harvesting

The magnetic field around the power-line in which an AC current flows can be used as an energy source by taking advantage of the electromagnetic induction phenomenon in a nearby coil (current transformer principle). Because of the high power density (150 $\mu W/cm^3$) and the system compact configuration, this technology has been highly adopted for the power line monitoring [142, 143] . However, the system needs a core clamped around to power-line, since its efficiency drastically reduces with the distance to the power-line. Therefore, harvesters should have insulation and decoupling systems for proper and safe operation. In addition, the exploitation of magnetic field energy harvesting (MFEH) inherently imposes constraints on the possible target applications, since this technology needs high currents through the conductor. Magnetic field energy harvesting method cannot operate when the transmission grid suffers an outage or power line is off.

5.1.1.6 Electric Field Energy Harvesting

The electric field induction on objects in proximity to energized conductors at power frequencies can be exploited as a power supply. This method is called electric field energy harvesting (EFEH). Electric field energy harvesting devices have the capability of operating while there is a voltage in the transmission grid. The power density is variable (0.02-25 $\mu W/cm^3$) and depends on the distance to the power line, the harvester design, and technical characteristics of transmission lines [145, 142] . Since electric field harvesters exploit strong electric field radiated by power-lines, these systems can be either in contact or not with the line. This characteristic has great potential in electromobility applications such as charging systems of power line inspection robotics [144, 128] . The harvester behavior can be easily predicted due to the fact that voltages and frequencies of a power system are regulated. However, the modeling and calibration of harvesters may be difficult several times because there are so many electric field sources in a transmission grid.

5.1.2 EFEH Solutions

By analyzing the most developed harvesting technologies, it is possible to conclude that harvesters based on EFEH have high applicability in power systems process [142]. Electric field energy harvesting source principle is based on the exploiting of the contained energy in a radial electric field emitted by an energized conductor [149]. Electric field energy harvesting systems have several advantages and are promising technologies to provide energy to SG sensors, due to their climate-resilient characteristics, low complexity, sufficient power rating, and low cost. Topologies for EFEH harvesters can be categorized into two groups: cylindrical and two-plate.

The cylindrical topology has been widely studied and applied both to high and medium voltage overhead transmission lines (MV/HV) [144, 128, 150] and low voltage conductors (LV) [142, 151, 152]. *Institute of Electrical Measurement Signal Processing of Graz University*, in 2008, introduced the EFEH concept using a cylindrical topology [153, 144]. Figure 5.4a shows the basic structure of the cylindrical topology. The prototype was equipped with a high voltage transformer and shunt regulator to maintain a voltage of 9 V on the secondary side. The harvester was presented as part of a sensing system capable of determining the temperature, distance to the ground, and degree of icing in power-lines in order to reduce the failure occurrence related to sags and increased vibrations of conductors.

The energy is usually harvested from the capacitor C_1 (direct contact with the power line) [144, 154], requiring sophisticated systems to ensure safety and protection of the device. In this regards, the *Research Center of Sensors and Instruments* developed a multi-layer

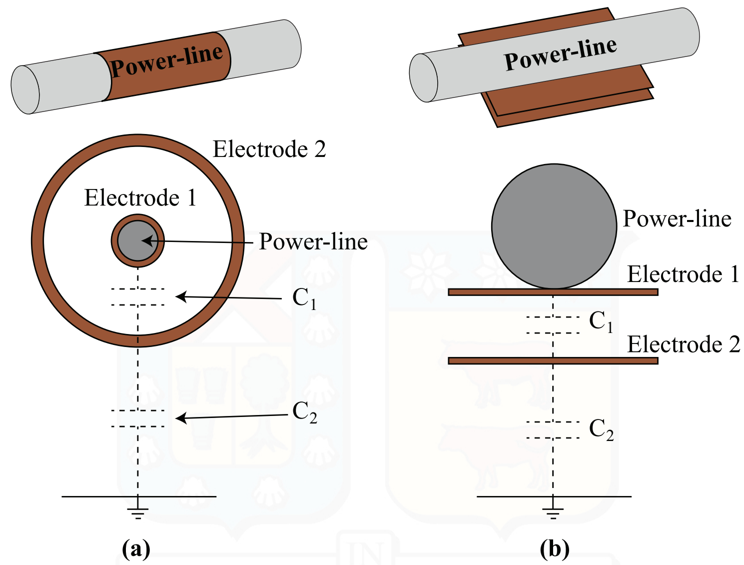

Figure 5.4: Topologies for EFEH harvester (3D view and cross section). **(a)** Cylindrical; **(b)** Two-Plate

cylindrical harvester, where the energy is extracted between two concentric electrodes around the energized conductor [155]. With the same aim, the *School of Electrical and Electronics Engineering* of theChung-Ang University studied the performance of a non-contact cylindrical harvester in a 765 kV three-phase power system [150]. In this case, the energy was extracted from the capacitor C_2 (floating capacitor). On the other hand, a modification of cylindrical geometry based on two concentric electrodes around the power lines is presented in [151, 152]. The main goal of this approach was to avoid direct contact with the transmission line. Also, a double-layer capacitor to harvest the energy from wireless networks was proposed in [142].

The Department of Electrical and Computer Engineering of the Ohio State University presented a cylindrical prototype, which can be used to harvest energy from high voltage direct current (HVDC) power lines [128]. The harvester works as a wind generator, where the HVDC transmission line is considered as the stator and a mobile rectangular winding is considered as the armature. The average output power of the linear generator is 1 mW.

The maximizing of the harvested energy is an important challenge for EFEH technology. *Chemnitz University of Technology* presented a multi-layer concept [156]. This new approach was conceived in order to satisfy the variable power needs of the specialized network elements. The basic cylindrical harvester and the theoretical analysis of the energy available was analyzed in [157]. Likewise, the basic conditions to get the maximum power from the harvester was presented in [158].

On the other hand, the two-parallel electrodes topology was first proposed in [159]. The basic structure of this topology is shown in Fig. 5.4b. In a similar way to cylindrical topology, the power is harvested from the capacitive coupling between the power conductors and electrodes. Loads may be connected to either capacitor C_1 [159, 127] or C_2 [160, 161]. Finally, a variation to this topology based on a non-contact two-plate harvester was proposed in [135].

Table 5.2: Comparison between Electric Field Energy Harvesting methodologies

Work	Power Density $\mu W/cm^3$	Harvested Power/Energy mW - mJ	Voltage Level kV	Harvester volume m^3	Characteristics	Main Application
[162]	111.29	23.6	12.7	2.12×10^{-4}	Cylindrical; non-contact; self-triggered flyback converter; medium voltage applications	Wireless sensor networks to measure transmission line variable
[145]	26.29	17	35	6.47×10^{-4}	Two plates; line contact; resistor divider; semi-conductors; medium voltage applications	Voltage sensor for high voltage power lines
[163]	10.38	16.3	110	1.57×10^{-3}	Cylindrical;line contact; transformer tap; high voltage applications	Smartgrid monitoring networks
[144]	9.52	370	150	3.89×10^{-2}	Cylindrical;line contact; transformer tap; high voltage applications	Online condition monitoring of high voltage power lines
[135]	$148 \mu J/cm^3$	—	400	3.14×10^{-3}	Two plates; line contact; transformer tank; high voltage applications	Wireless sensor networks to measure substations variables
[164]	0.056	0.18	7	3.14×10^{-3}	Two plates; non-contact; switching plates in short circuit	Wireless sensor networks to measure substations variables
[142]	—-	12	220 V	—	Double-layered cylindrical; low voltage applications;	Smartgrid monitoring networks

5.2 Electric Field Energy Harvesting

According to basic principles of electrostatics a time varying electric field produces a displacement current given by

$$I_d = \varepsilon \frac{d\Phi_E}{dt}, \tag{5.3}$$

where ε is the permittivity of the dielectric material between power-line and plate, I_d is the displacement current and Φ_E is the electric flux. This displacement current can be used to charge a parasite capacitor. The stored energy is given by

$$E = \frac{1}{2} C V^2, \tag{5.4}$$

where E is the energy stored, C is the capacitance of the parasite capacitor, and V is the voltage collected. Due to this method exploits the electric field, it is called electric field energy harvesting.

In traditional EFEH generators, the electrodes located at different distances to the energized conductors create an electrical grid that can be seen as a capacitive voltage divider. Figure 5.5 shows the electric field distribution of an energized wire (3-wires, Phase-Ground-Neutral), and the effects of putting a two-plate harvester on this field. Capacitor C_{PS_i}, C_{NS_i} and C_{GS_i} are defined as the coupling among the i-th electrode and the power-line, neutral wire and ground reference respectively. The value of different capacitors depends

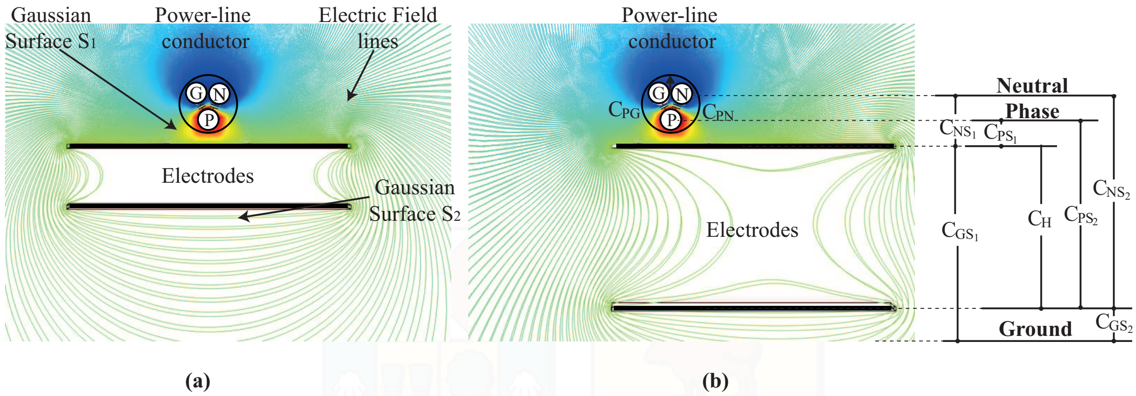

Figure 5.5: Electric field energy harvesting from a power-line. **(a)** The electrodes separation is 2 cm and the harvester is centered with the power-line; **(b)** The electrodes separation is 4 cm and the harvest is positioned at the right of the power-line.

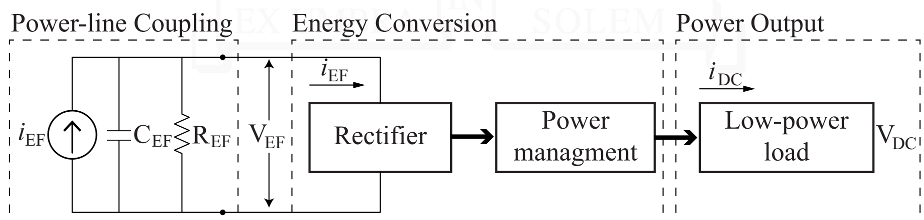

Figure 5.6: A full electric field energy harvesting system.

on both the electric field magnitude in the power line and the geometry of the complete coupled systems, and it can be expressed as

$$C = \frac{\varepsilon \oiint_S \mathbf{E} \cdot d\mathbf{S}}{\int_a^b \mathbf{E} \cdot d\mathbf{l}}, \tag{5.5}$$

where **E** is the electric field intensity, **S** is the electric-flux-coupling Gaussian surface, **l** is length differential between the electrode and the power line and ε is the permittivity of the dielectric material between power-line and electrode.

An electric field energy harvesting system aim is to deliver an appropriate power supply to a final load, it consists of four basic stages, as shown in Fig.5.6, which aim is to deliver sustainable energy to the load. Briefly, each harvester stage can be defined as follows:

- *Power-line Coupling:* It is the representation of the capacitive network that can be formed by one or several electrodes and one or several power-lines. The energy is harvested by connecting different circuits to terminals of any parasitic capacitor.
- *Energy Conversion:* The power output by the electric field harvester cannot be directly used by the load circuits as micro-controllers, wireless nodes, etc. The alternating current and voltage across the harvester's capacitor need to be conditioned

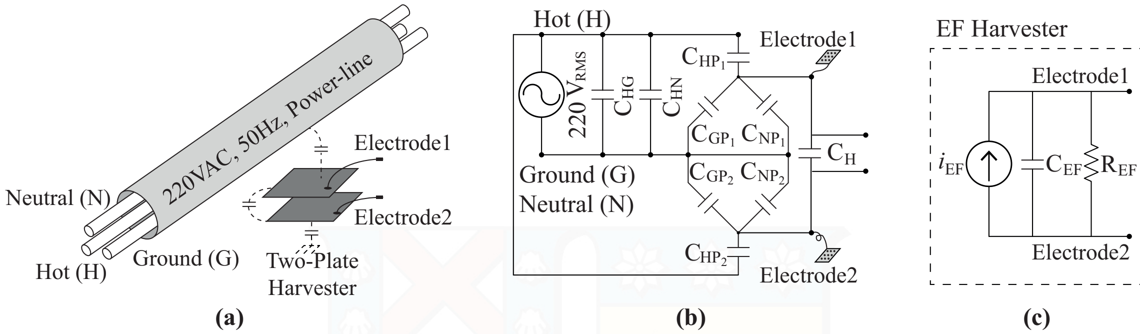

Figure 5.7: Schematic diagrams of EFEH. **(a)** Schematic of two-electrodes concept and the capacitive voltage divider dispersion; **(b)** Equivalent circuit of the EFEH system, showing parasitic capacitances; **(c)** Single-capacitor model of an EFEH device.

and converted to appropriately current and voltage levels that can be used by the load's circuits.

- *Power Output:* Electronic schemes in charge of efficiently matching the low power harvested to the consumption of the load, within some limited operation schedule.

5.2.1 Electric Field Energy Harvesting Concept

The main objective of the model given in Fig. 5.7a is to collect the available energy in the capacitive network by deviating the displacement current from the conductor to a load. The capacitive network based on two electrodes located near to an energized wire (3-wires, Phase-Ground-Neutral) is depicted in Fig. 5.7b, where each capacitance represents the coupling between two different elements of the electrical grid. As shown in Fig. 5.7c, the capacitive divider has been replaced with Norton equivalent. The harvester can be modeled as a sinusoidal current source in parallel with a capacitance C_{EF} and resistance R_{EF}. For the sake of this analysis, assume that R_{EF} is despicable. Therefore, the input equivalent impedance (which is a simple capacitor) is given by,

$$C_{EF} = \frac{(C_{GS\,1} + C_{NS\,1} + C_{PS\,1})\,(C_{GS\,2} + C_{NS\,2} + C_{PS\,2})}{C_{PS_1} + C_{GS_1} + C_{NS_1} + C_{PS_2} + C_{GS_2} + C_{NS_2}} + C_H, \tag{5.6}$$

Capacitors $C_{GS\,i}$, $C_{NS\,i}$ and $C_{PS\,i}$ depend only on the geometry of the harvester. Regarding to C_H, although its minimum value depends on the geometry of the harvester, any element connected across its terminals affects the capacitance, thus it cannot be considered constant.

The Thevenin equivalent voltage source is given by

$$V_{EF} = \frac{V_{line}}{C_{eq} + C_H}\left[\frac{C_{PS_1}\,(C_{GS_2} + C_{NS_2}) - C_{PS_2}\,(C_{GS_1} + C_{NS_1})}{C_{PS_1} + C_{GS_1} + C_{NS_1} + C_{PS_2} + C_{GS_2} + C_{NS_2}}\right] \tag{5.7}$$

where,

$$C_{eq} = \frac{(C_{GS\,1} + C_{GN1} + C_{PS\,1})\,(C_{GS\,2} + C_{GN2} + C_{PS\,2})}{C_{GS\,1} + C_{GN1} + C_{PS\,1} + C_{GS\,2} + C_{GN2} + C_{PS\,2}}. \tag{5.8}$$

The Norton equivalent current source is given by

$$i_{EF} = \omega_{EF} C_{EF} V_{EF} \sin(\omega_{EF} t), \tag{5.9}$$

where ω_{EF} is the angular frequency.

5.2.1.1 Theoretical Maximum Power Extraction

The maximum power can be extracted from a harvester if the power converter and the load present a conjugate impedance match to the harvester ($Z_L = R_{EF} + j/\omega_{EF} C_{EF}$). The theoretical generalized maximum power is given by

$$P_{RECT\,(max)} = \frac{{I_{EF}}^2 R_{EF}}{8} = \frac{{\omega_{EF}}^2 {C_{EF}}^2 {V_{EF}}^2 R_{EF}}{8}. \tag{5.10}$$

Unlike conventional power supplies and commercial batteries, which have relatively low internal impedance, the EFEH generators internal impedance is very high. This high internal impedance restricts the amount of output current that can be driven by the EFEH source to the micro-amperes range. Likewise, the inductance needed to present a conjugate match is impractical due to the fact that the harvester's capacitance is very small (tens of pF), which implies a high inductance (tens of henries). In addition, the power output by the electric field harvester cannot be directly used by electronic devices, it needs to be conditioned and converted to a form usable by the load circuits. In this context, a large number of practical load circuits (e.g. voltage doubler, full-bridge rectifier, switch-only rectifier, DC-DC converters) could replace the resistive loads.

5.2.1.2 Resistive load analysis

The AC circuit steady state analysis of the capacitor divider shown in Fig. 5.7c was performed with a resistor R_L connected between electrodes. The average power delivered P_{RECT_R} is given by

$$P_{RECT,R} = \frac{R_L {\omega_{EF}}^2 {C_{EF}}^2 {V_{EF}}^2}{1 + {\omega_{EF}}^2 {R_L}^2 {C_{EF}}^2}. \tag{5.11}$$

Hence, the load resistor R_L, the harvester's capacitor C_{EF} and the harvester's voltage V_{EF} are the freedom degrees, which can be modified in order to maximize the power output. When $\partial P_{RECT,R}/\partial R_L = 0$ the optimal load resistor $R_{L_{opt}}$ can be computed by 5.12. Therefore, the maximum power $P_{RECT,R_{max}}$ can be obtained with $R_{L_{opt}}$, as shown in 5.13. On the other hand, $P_{RECT,R}$ increases directly with the increment of C_{EF} and V_{EF}.

$$R_{L_{opt}} = \frac{1}{\omega_{EF} C_{EF}}. \tag{5.12}$$

$$P_{RECT,R_{max}} = \frac{\omega_{EF} C_{EF} {V_{EF}}^2}{2} \tag{5.13}$$

In order to test the behavior of the EFEH system under resistive load, an energized wire (3 wires, Phase-Ground Neutral) was wrapped with an aluminum foil of 30 cm and different resistors R_L were connected between the harvesting electrode (aluminum tube) and the ground reference, as shown in Fig. 5.8a. The diagram showing parasitic capacitance between the metallic sheath and the energized wire is shown in Fig.5.8b. The equivalent circuit of the measurement circuit, shown in Fig. 5.8b, can be reduced by assuming that the power-line is symmetric. In other words, the capacitors between the surrounding aluminum sheet and the three wires (phase, ground and neutral) are the same $C_{PG} = C_{PN} = C_{PH}$. Furthermore, the parasite capacitors between wires are the same $C_{HG} = C_{HN}$. However, both capacitors do not influence the analysis. According to [152], the measured C_{PH} is 1.65 pF per unit centimeters of the surrounded power line.

A simulation of the experimental circuit was implemented using the PSIM software package. Figure 5.8d shows the simulated results of the available average power, varying the tube's length. It is possible to note that the maximum power available increases with the aluminum tube length. However, the harvested power is very low (tens of microwatts).

The development of experimental tests has several limitations related to the high input impedance of the harvester and the influence of the measurement systems in the load system. The input impedance of the harvester's capacitor at line frequency is in the range of several Mega-ohms. Therefore, reliable measurements cannot be obtained when the load's impedance is lower than the harvester's capacitive impedance since the load voltage drop is very low and could be affected by the instrument's tolerance. On the other hand, the use of high impedance loads is affected by the impedance of the measuring device. Hence, modeling the measuring device is imperative to analyze the behavior of the circuit.

Figure 5.8e shows the comparison between theoretical, simulated and experimental results. It is possible to observe that the theoretical results –solid blue line– have a similar behavior than simulated results –magenta x– when the measuring device effects are despised. However, experimental results –green asterisks– have a considerable variation. In this context, a simulation of the experimental circuit, taken into account all the impedances present in the experimental test was developed. A voltage probe model RP1300H is employed to acquire the voltage measurements, which technical characteristics are summarized in Table 5.3. The voltage probe can be modeled as a resistor with a parallel capacitor. The simulated results –black dash line– shows similar behavior to experimental results.

5.2.1.3 Experimental Validation

The proposed approach performs a two-stage conversion system in order to provide both a safe voltage and current to the load, as shown in Fig. 5.9a. The equivalent circuit of the proposed EFEH system and the Norton equivalent are shown in Fig. 5.9b and Fig. 5.9c, respectively. The first stage is based on a full-bridge rectifier with a smoothing capacitor,

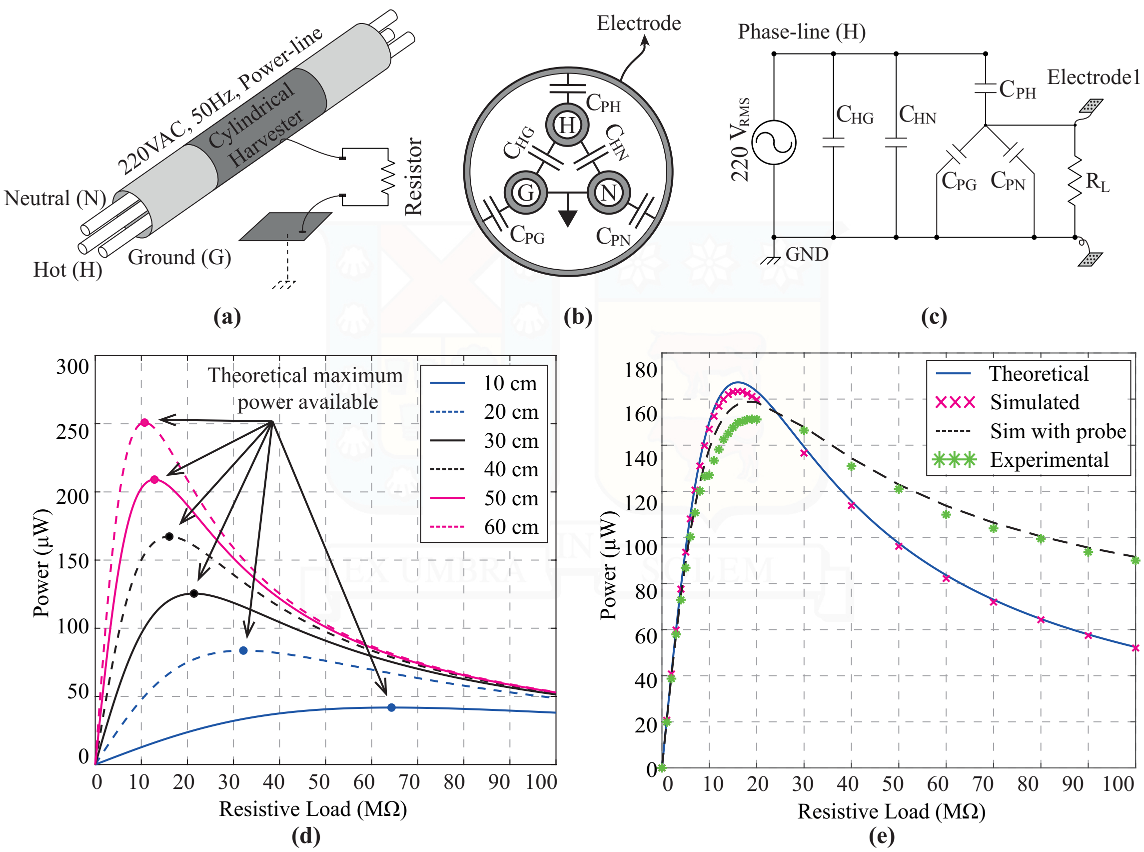

Figure 5.8: Harvester behavior under resistive load. **(a)** Schematic diagram of experimental setup; **(b)** The depiction of sheath wrapping resultant stray capacitors; **(c)** Equivalent circuit of the EFEH system; **(d)** Simulation results of available power against load resistance; **(e)** Experimental validation results of the proposed EFEH system under resistive load

which rectifies the induced voltage (50 Hz, AC) in the electrodes. The storage capacitor is of 1 μF in order to reduce the charging time. The system cannot be connected to the load all the time, due to the fact that the energy transfer rate to the load is much higher than the power flow from the AC side. In other words, the DC bus is discharged and its voltage falls. On the other hand, the second stage controls the power transfer between the harvester and load through the control of switch S_1. This stage is focused on the stabilization of the DC bus voltage and the exchanged power. The operation can be briefly summarized as follows,

1. The switch S_1 is initially turned off. At this time, the voltage and current in the load Z_L is zero and the energy harvested from the electric field is stored in C_S increasing its voltage.

2. When the DC bus voltage charges up to a predefined trigger voltage, S_1 is turned-on with a pulse. At this time, the power is discharged in Z_L, increasing both its voltage and current in the load and reducing the voltage in the DC bus.

3. Finally, S_1 is turned-off and another energy-pulsed transfer cycle is initiated, generat-

Table 5.3: Technical specifications of voltage probes used in this work.

Voltage probes	Technical Specifications	
RP1300H Rigol	Bandwidth:	DC to 300 MHz
	Input Capacitance:	5.5 pF
	Input resistance:	100 MΩ
	Maximum Input Voltage:	2000 V
TPP010x Tektronix	Bandwidth:	DC to 100 MHz
	Input Capacitance:	12 pF
	Input resistance:	10 MΩ
	Maximum Input Voltage:	300 V

ing a voltage pulse train in the load.

Figure 5.10a shows the storage capacitor voltage when the electrodes were in contact or separated 2 cm from the no-load/open circuit AC power line. The distance between electrodes was of 3 cm and the triggered voltage was of 5 V. Figure 5.10b shows the load voltage for both previous cases. It is worth noting that the frequency exhibits a variable behavior in the load voltage (contact: 0.2017 Hz; non-contact: 0.3368 Hz), which depends on the distance between electrodes. In other words, the harvester powers intermittently the load.

5.2.2 Energy Conversion

The power output by the electric-field harvester is not in a form which can directly be used to load circuits. The voltage and current output by the harvester must be conditioned and converted to a form usable by the load circuits. The low-power management systems (conditioning and converting circuits) should be capable of extracting the maximum power available out of the electric field harvester.

5.2.2.1 Voltage-doubler

In low voltage applications, the voltage doubler topology has been highly used. The simple diode-capacitor circuit consists of only two diodes and two capacitors (harvester's capacitor and storage capacitor), as shown in Fig. 5.11a. The output voltage V_{DC} can be two times the maximum voltage V_{TH}. In other words, the array of diodes and capacitor works in such a way that it doubles the input voltage. The voltage and current waveforms associated with this circuit are shown in Fig. 5.11b. For the purposes of this study, we assume that the value of C_S is large compared to C_{EF} and that the output voltage V_{DC} is practically constant. Additionally, the voltage drop across the diode is defined as V_D. Every positive half-cycle of the input current can be divided into two regions. In the interval between $t = t_{on}$ to $t = t_{off}$ the current flows through the harvester's capacitor C_{EF} to charge it. Since both diodes are reverse-biased, the storage capacitor is not charged. This condition occurs while the harvester voltage V_{EF} is less than the storage capacitor voltage $V_{DC} + V_D$.

When V_{EF} is greater than $V_{DC} + V_D$, interval between $t = t_{off}$ to $t = t_{\pi}$, the diode

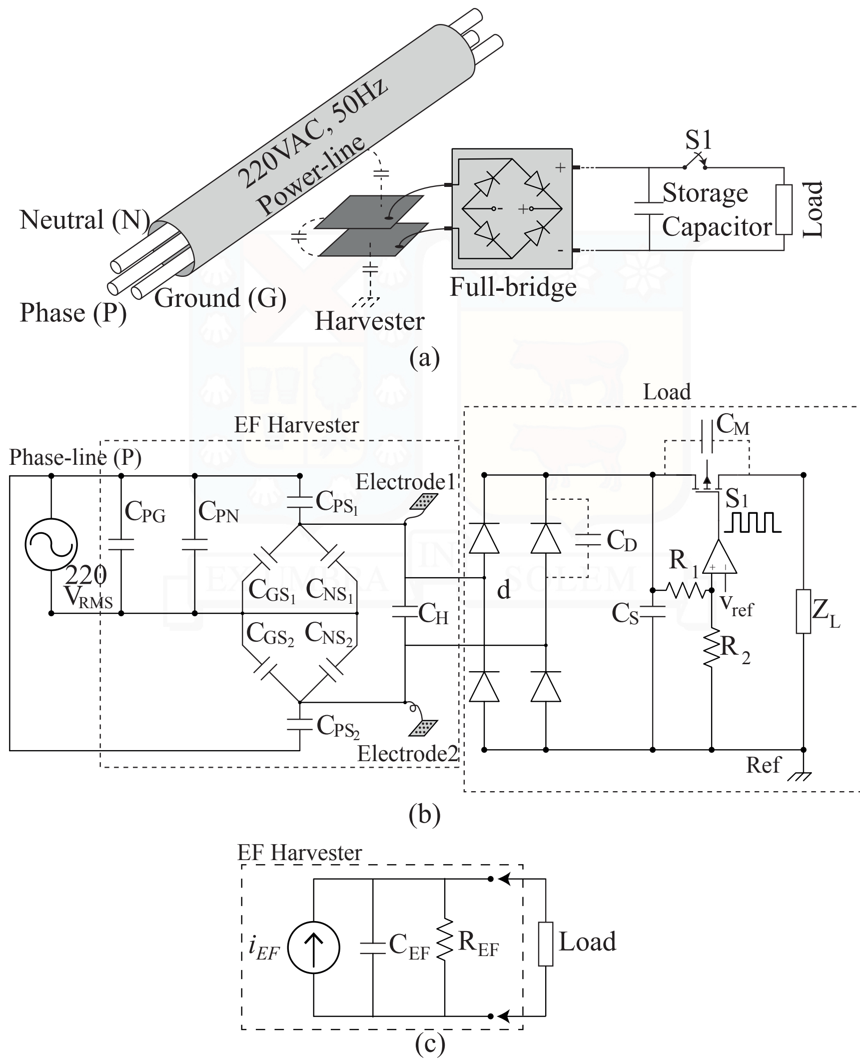

Figure 5.9: Schematic diagrams of EFEH. **(a)** Schematic of two-electrodes concept and the capacitive voltage divider dispersion; **(b)** Equivalent circuit of the EFEH system, showing parasitic capacitances; **(c)** Single-capacitor model of an EFEH device.

D_1 turns on and the harvester's current flows into the storage capacitor. This condition continues until the harvester's current changes the direction. During the negative half cycle of the sinusoidal input waveform, diode D1 is forward biased and the harvester's voltage is $-V_D$ Likewise, the storage capacitor current is zero. The total value of charge available for the electric field harvester in one period time T is given by

$$Q_{av,T} = \int_0^{2\pi} I_{EF} \sin(\omega_{EF} t) d(\omega_{EF} t) = \frac{4I_{EF}}{\omega_{EF}} = 4C_{EF} V_{EF} \tag{5.14}$$

Every positive half-cycle, the harvesters current need to charge C_{EF} from $-V_D$ to $V_{DC} + V_D$ before diodes turn on. The amount of charge lost every positive half-cycle can be

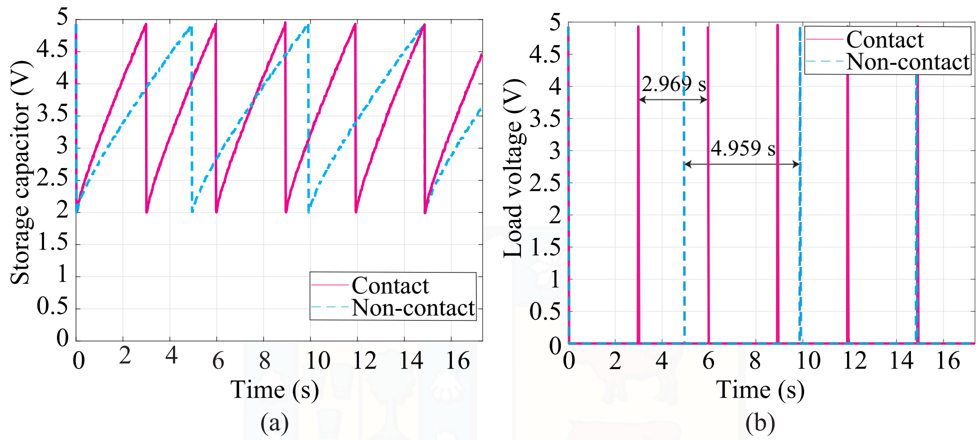

Figure 5.10: Experimental results of the harvester. One electrode is both in contact and non-contact with the electrical wire. **(a)** Storage capacitor voltage; **(b)** Load voltage.

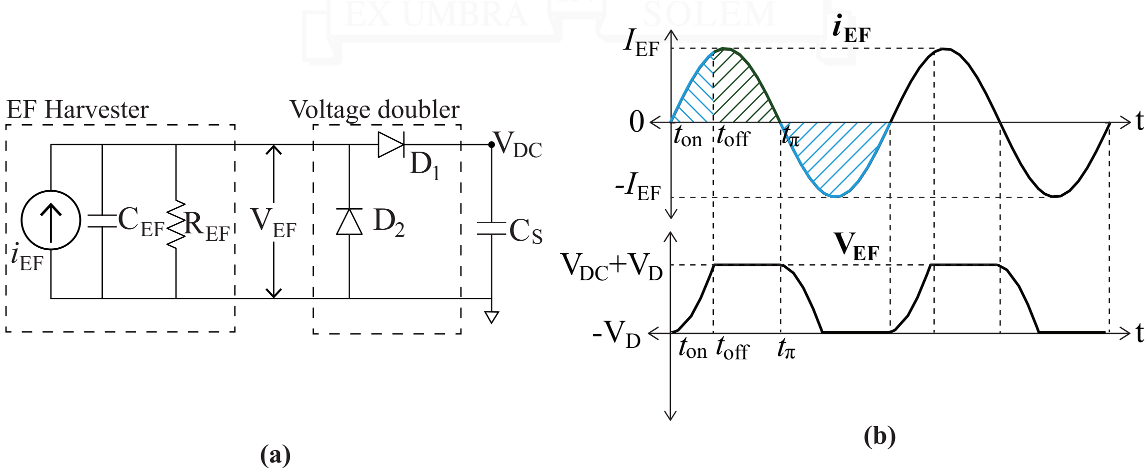

Figure 5.11: Voltage-doubler analysis **(a)** A voltage-doubler circuit to extract power from a electric field energy harvester; **(b)** Current and voltage wavesforms for a voltage-doubler circuit connected to electric field energy harvester.

computed by

$$Q_{loss,T+} = C_{EF}\left(V_{DC} + 2V_D\right) \tag{5.15}$$

Due to the fact that the diode does not conduct in a negative cycle, the amount of charge lost every negative half-cycle can be computed by

$$Q_{loss,T-} = \int_{\pi}^{2\pi} I_{EF}\sin\left(\omega_{EF}t\right)d\left(\omega_{EF}t\right) = 2C_{EF}V_{EF} \tag{5.16}$$

The difference between charge available and charge lost every positive and negative half-cycle represents the charge that flows into the storage capacitor C_S. This can be given by

$$Q_{RECT,T} = Q_{av,T} - Q_{loss,T+} - Q_{loss,T-} = 2C_{EF}V_{EF} - C_{EF}\left(V_{DC} + 2V_D\right) \tag{5.17}$$

The energy delivered can be computed by

$$E_{RECT,T} = Q_{RECT,T}V_{DC} = C_{EF}V_{DC}\left(2V_{EF} - V_{DC} - 2V_D\right) \tag{5.18}$$

The cycle repeats at grid frequency $f_{EF} = \omega_{EF}/2\pi$. The power delivered to the output by the voltage-doubler circuit is

$$P_{RECT,VD} = C_{EF}V_{DC}f_{EF}\left(2V_{EF} - V_{DC} - 2V_D\right) \tag{5.19}$$

The output power depends on the rectified voltage in the storage capacitor V_{DC}. It is possible to note that at low values of V_{DC}, most of the charge available flows from the harvester into the output but the voltage is low. On the other hand, if the V_{DC} is high, very little charge flows into the output. When $\partial P_{RECT,VD}/\partial V_{DC} = 0$ the optimal voltage rectified is $V_{DC_{opt}} = V_{EF} - V_D$ and the maximum power delivered can be given by

$$P_{RECT,VD(max)} = \frac{\omega_{EF}C_{EF}(V_{EF} - V_D)^2}{2\pi} \tag{5.20}$$

Figure 5.12 shows a comparison between theoretical and simulated results. A diode 1N4007 is simulated, whose value of voltage drop is 0.7 V, according to the manufacturer.

A cylindrical harvester was used to perform all the measurements reported in this section. The cylindrical capacitor has a length of 60 cm and is in contact with the insulator of an energized wire. Figure 5.13 shows oscilloscope waveforms of the output voltage of the electric field harvester for the different rectifier scenarios. The amplitude of the open-circuit voltage of the electric field harvester was 103 V for this measurement. It is worth noting that the acquired waveforms are consistent with developed analysis. In addition, it is important to note that the circuit requires barely two electronic components (two diodes). The maximum power is achieved when V_{DC} is equal to the maximum value of the open-circuit voltage. However, the circuit is not efficient in every negative half-cycle (the current does not flow into the output).

5.2.2.2 Full-bridge rectifier

A full-bridge rectifier, as shown in Fig. 5.14a is one of the most commonly used rectified systems to convert the electric field harvester AC output into a DC voltage. In this topology, a smoothing capacitor C_S is connected to the rectifier's output. For the purposes of this study, we assume that the value of C_S is large compared to C_{EF} and that the output voltage

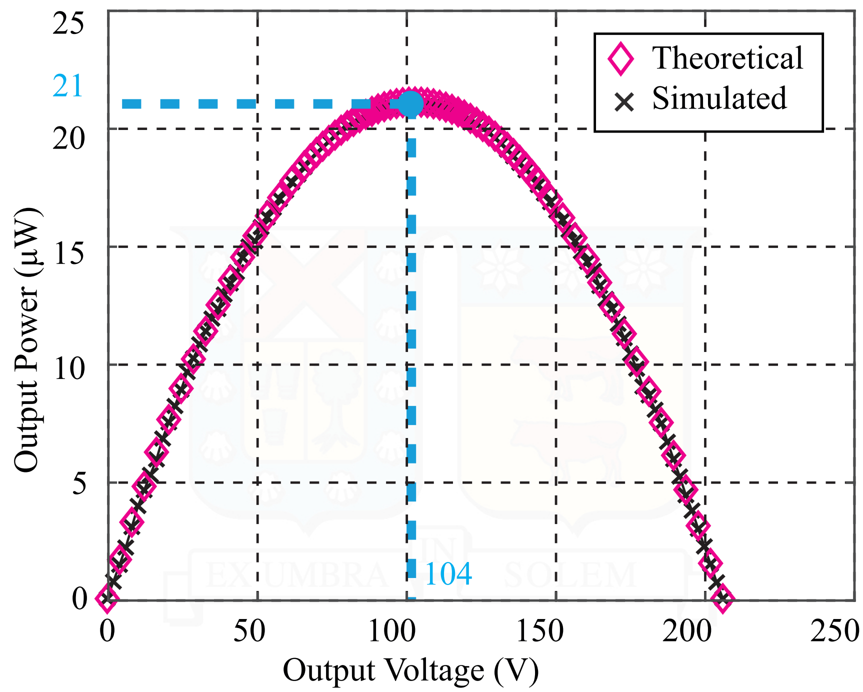

Figure 5.12: Theoretical and simulated maximum output power considering a voltage doubler circuit.

V_{DC} is practically constant. The voltage and current waveforms associated with this circuit are shown in Fig. 5.14b. This topology cannot ensure that the energy always flows from the electric field harvester to the storage capacitor.

Unlike the voltage doubler topology, the harvester's current flowing to the storage capacitor occurs every half-cycle. Initially, the current charges the harvester's capacitor C_{EF} in the interval between $t = t_{on}$ to $t = t_{off}$. The current does not flow to the storage capacitor C_S due to the fact that the diodes are reverse-biased. When the harvester's voltage V_{EF} is equal to the storage capacitor voltage $V_{DC} + 2V_D$, the diodes D_1 and D_4 are forward-biased. This condition occurs continuously until the current changes the direction. In the negative half-cycle, the harvester has a similar behavior. All diodes are initially reverse-biased as long as the V_{EF} is less than the V_{DC}. If V_{EF} is equal to $V_{DC} + 2V_D$, the pair of diodes D_2 and D_3 are forward-biased, and the current flows to the load. Similarly, the total amount of charge available is given by 5.14.

Every cycle, electric field harvester current has to charge C_{EF} from $-V_{DC} - 2V_D$ to $V_{DC} + 2V_D$ and vice-versa before the diodes turn on. The amount of charge lost every cycle can be defined by

$$Q_{lost,T} = 2C_{EF}\left((V_{DC} + 2V_D) - (-V_{DC} - 2V_D)\right) = 4C_{EF}\left(V_{DC} + 2V_D\right) \quad (5.21)$$

The charge that flows into the storage capacitor is possible to define as the difference

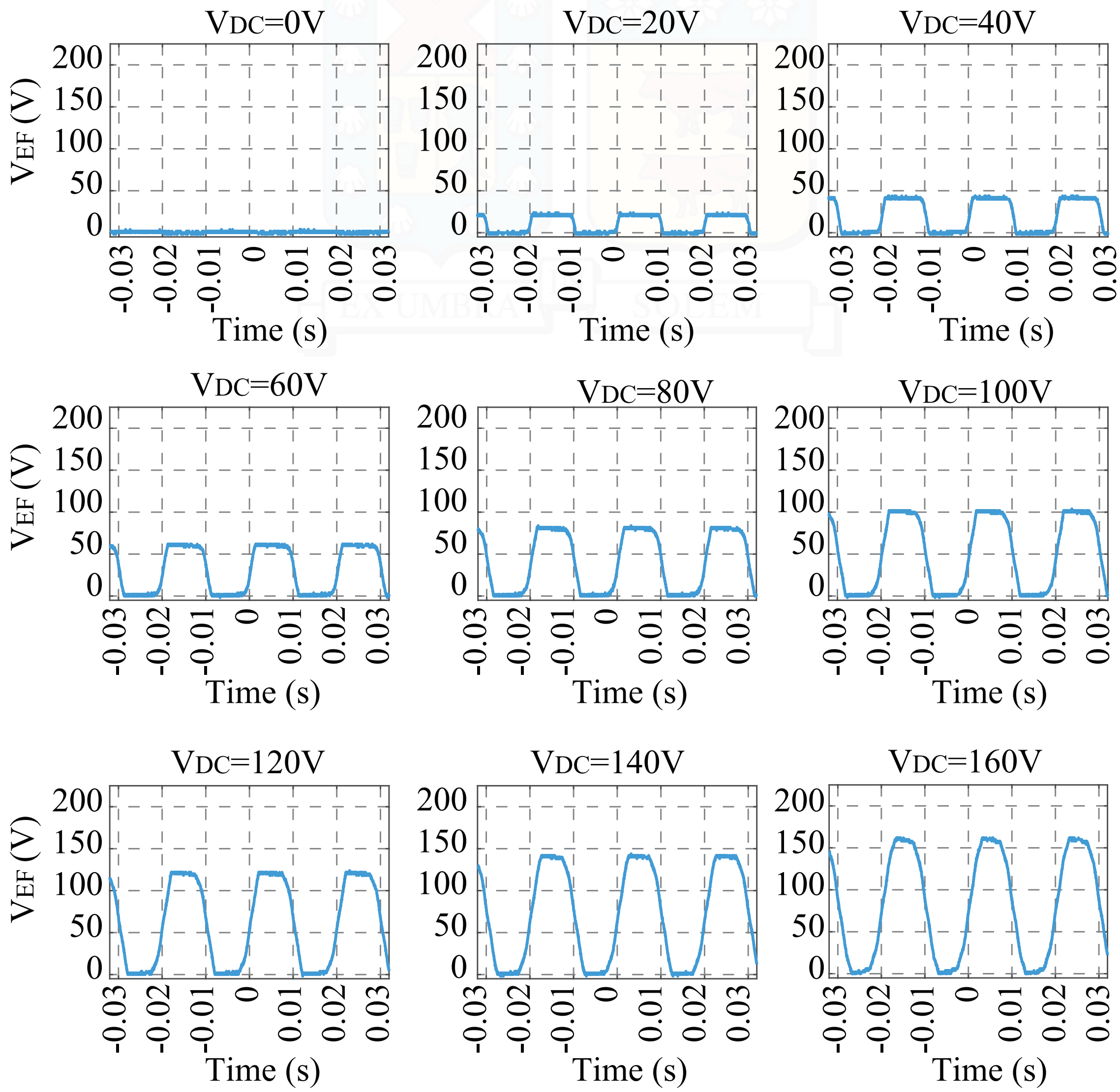

Figure 5.13: Measured waveforms of the output voltage across the electric field harvester for the voltage-doubler case

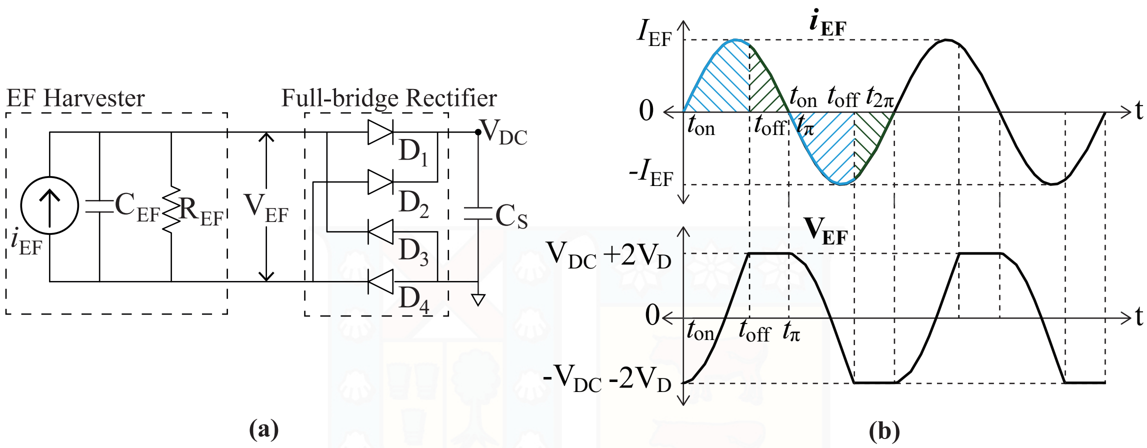

Figure 5.14: Full-bridge analysis. **(a)** A full-bridge rectifier circuit to extract power from a electric field energy harvester; **(b)** Current and voltage wave-forms for a full-bridge rectifier circuit connected to electric field energy harvester.

between charge available and charge lost. This can be given by

$$Q_{RECT,T} = Q_{av.T} - Q_{lost,T} = 4C_{EF}\left(V_{EF} - V_{DC} - 2V_D\right) \tag{5.22}$$

The energy delivered can be computed by

$$E_{RECT,T} = Q_{RECT,T}V_{DC} = 4C_{EF}V_{DC}\left(V_{EF} - V_{DC} - 2V_D\right) \tag{5.23}$$

The cycle repeats at grid frequency $f_{EF} = \omega_{EF}/2\pi$. The power delivered to the output using the full-bridge rectifier circuit is

$$P_{RECT,VD} = 4C_{EF}V_{DC}f_{EF}\left(V_{EF} - V_{DC} - 2V_D\right) \tag{5.24}$$

When $\partial P_{RECT,FB}/\partial V_{C_S} = 0$ the optimal voltage rectified is $V_{DC_{opt}} = V_{EF}/2 - V_D$. The maximum power that can be obtained using the full-bridge rectifier, considering ideal diodes is given by

$$P_{RECT,FB(max)} = \frac{\omega_{EF}C_{EF}(V_{EF} - 2V_D)^2}{2\pi}. \tag{5.25}$$

Figure 5.15 shows a comparison between theoretical and simulated results. A diode 1N4007 is simulated, whose value of voltage drop is 0.7 V, according to the manufacturer.

To validate the full-bridge rectifier, a cylindrical harvester was used, whose length is 60 cm and was located in contact with the insulator of an energized wire. The harvester has an open-circuit voltage of 103 V in this application. Figure 5.16 shows oscilloscope waveforms of the output voltage of the electric field harvester for the different full-bridge rectifier

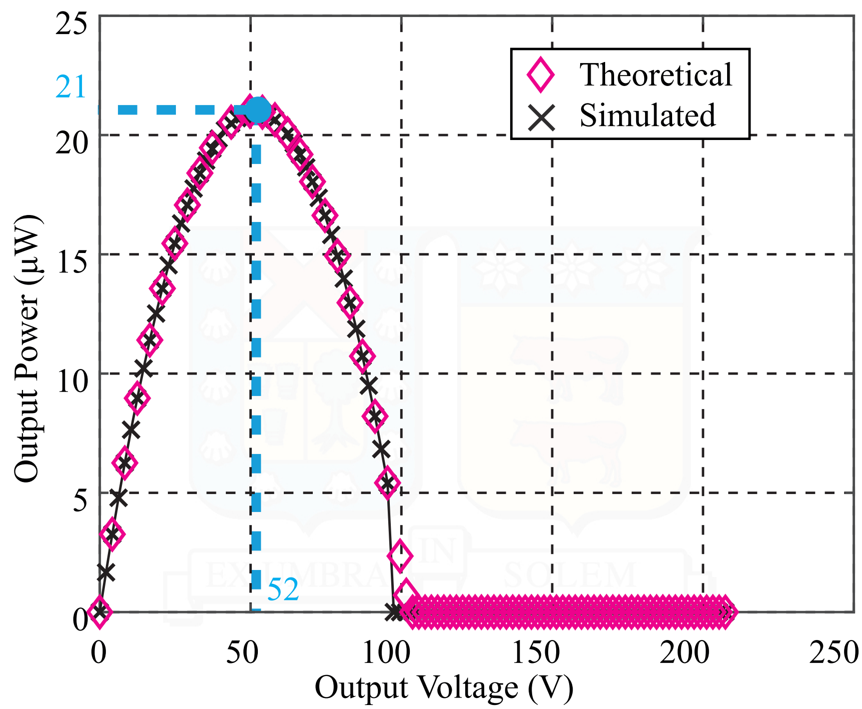

Figure 5.15: Theoretical and simulated maximum output power considering a full-bridge rectifier.

scenarios. Unlike to voltage doubler circuit, full bridge rectifier needs two additional diodes. However, the maximum power that can be extracted is the same as that obtained using a voltage-rectifier circuit. In addition, full-bridge rectifier reduces the maximum voltage to half. Since the full-bridge rectifier operates two times every cycle, the amount of charge lost is reduced.

5.2.2.3 Parallel switch-only rectifier

The theoretical analysis of the voltage doubler and the full-bridge rectifiers shows that both these circuits can deliver the same amount of maximum output power. The main difference lies in the fact that the voltage doubler provides two times the maximum voltage (maximum power) and only needs two diodes. However, both circuits present high losses related to the charging and discharging of the harvester's capacitor, constraining the capability of harvesting the maximum available power.

As shown in Fig. 5.17, the parallel switch-only rectifier merge both circuits by adding a bidirectional parallel switch S_1 to a traditional full bridge rectifier in order to harness the advantages from the previously analyzed rectifiers: **(i)** the full-bridge, the current flows into the output load every half-cycle and **(ii)** the voltage-doubler has a parallel-diode that helps in the pre-discharging of the harvester's capacitor to the ground.

In the beginning, the switch S_1 is turned off and the circuit functions similarly to the full-bridge rectifier. In other words, the harvester's current flows into the harvester's capacitor to charge it. When the V_{EF} is equal to $V_{DC} + 2V_D$, the harvester's current flows to output. The zero-crossing of the harvester's current briefly turns on the S_1, discharging the

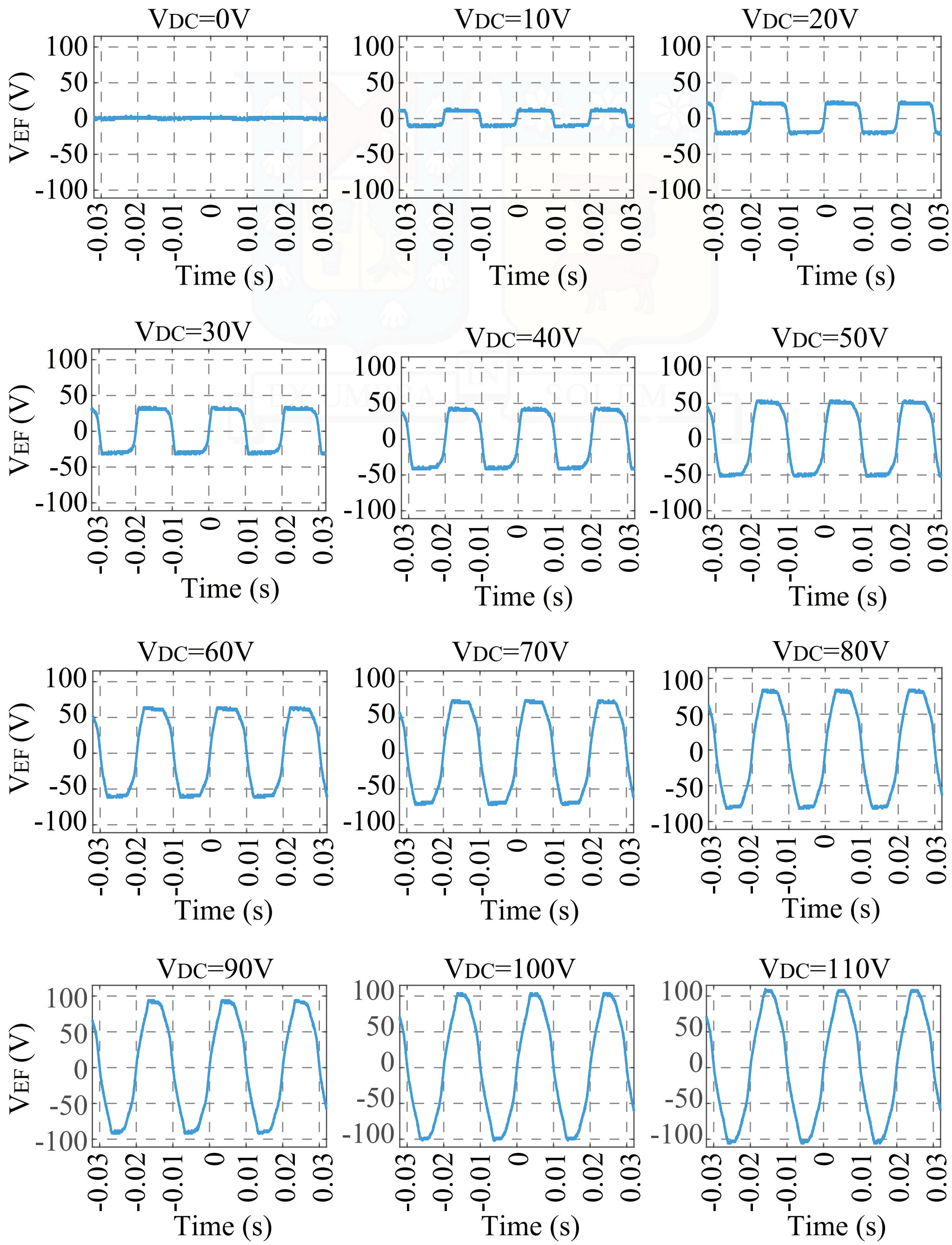

Figure 5.16: Measured waveforms of the output voltage across the electric field harvester for the full-bridge case

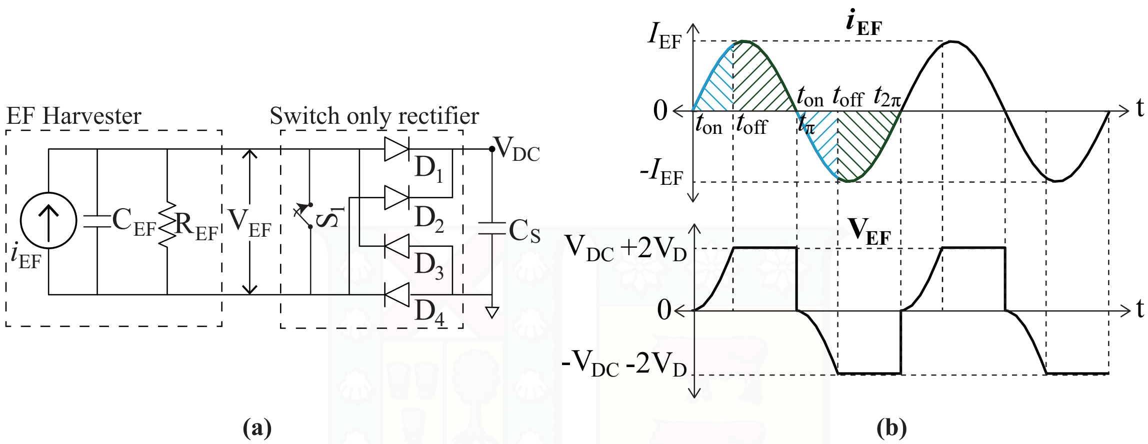

Figure 5.17: Switch only rectifier analysis. **(a)** A switch-only rectifier circuit to extract power from a electric field energy harvester; **(b)** Current and voltage wave-forms for a switch-only rectifier rectifier circuit connected to electric field energy harvester.

harvester's capacitor to ground. Therefore, the current only has to charge up the harvester's capacitor from 0 to $\pm(V_{DC}+2V_D)$ before it can flow into the load. The amount of charge lost every cycle is defined by

$$Q_{loss,T} = 2C_{EF}\left(V_{DC}+2V_D\right) \tag{5.26}$$

The total charge that actually flows into the storage capacitor C_S is computed by the difference between the total charge available and the charge lost,

$$Q_{RECT,T} = 2C_{EF}\left(2V_{EF}-V_{DC}-2V_D\right) \tag{5.27}$$

The power delivered to the output using the parallel switch-only rectifier circuit is

$$P_{RECT,PSO} = 2C_{EF}V_{DC}f\left(2V_{EF}-V_{DC}-2V_D\right) \tag{5.28}$$

When $\partial P_{RECT,FB}/\partial V_{C_S} = 0$ the optimal voltage rectified is $V_{DC_{opt}} = V_{EF} - 2V_D$. The maximum power that can be obtained using the full-bridge rectifier, considering ideal diodes is given by

$$P_{RECT,PSO_{max}} = \frac{\omega_{EF}C_{EF}(V_{EF}-2V_D)^2}{\pi} \tag{5.29}$$

It is possible to observe that the parallel switch-only rectifier provide two times the amount of maximum power that was provided by the full-bridge rectifier or voltage-doubler circuit. In addition, the optimal rectifier's voltage is equal to the voltage-doubler analysis, as shown in Fig. 5.18.

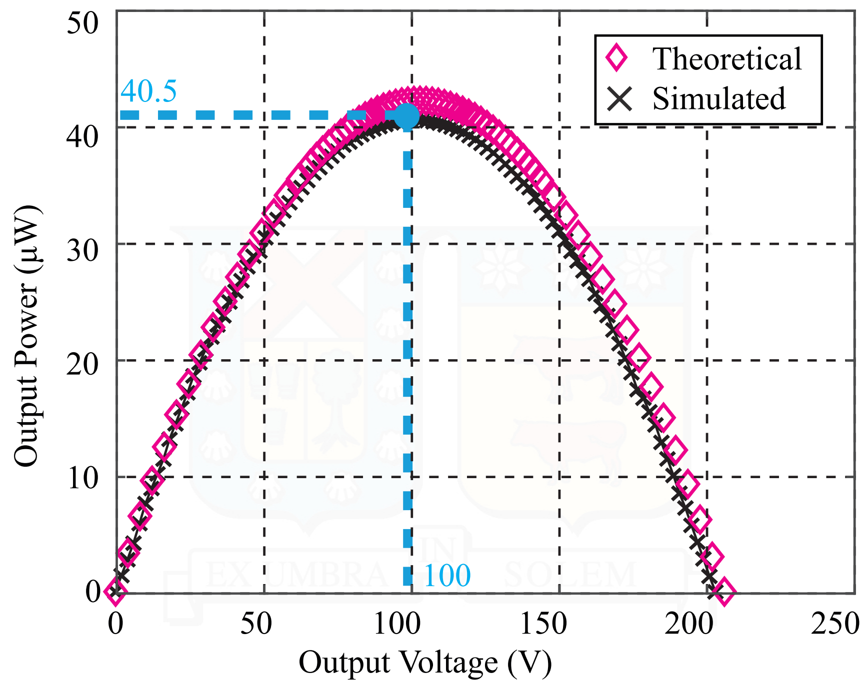

Figure 5.18: Theoretical and simulated maximum output power considering a parallel switch-only rectifier.

5.3 Maximum power transfer based on power-line coupling

The harvester's output power increases both with the value of the harvester's capacitor and the square of the harvester's voltage for the previously analyzed cases. Therefore, the design of efficient harvesters and the selection of effective energy conversion strategies are important elements in the attainment of the optimal power. This section presents the analysis of the power available as a function of the capacitive coupling designs.

5.3.1 Power-line Coupling

As shown in Section 5.2, the available energy is mostly limited, mainly, in low-voltage and non-contact applications. Since the amount of energy consumed by the wireless sensor node is related to its lifetime, the use and development of high-performance systems in each sensor node stage is a necessity. In this context, the new technologies should be focused on the usage and development of ultra-low power, high-performance micro-controllers, low-loss regulators, and efficient embedded systems. It is also essential to enhance both energy harvesting and energy storage capabilities.

The objective of this section is to provide an empirical study of the geometric design of electric-field harvesters and their influence in the harvesting process. Three configurations including two traditional topologies and one multi-layer structure were analyzed.

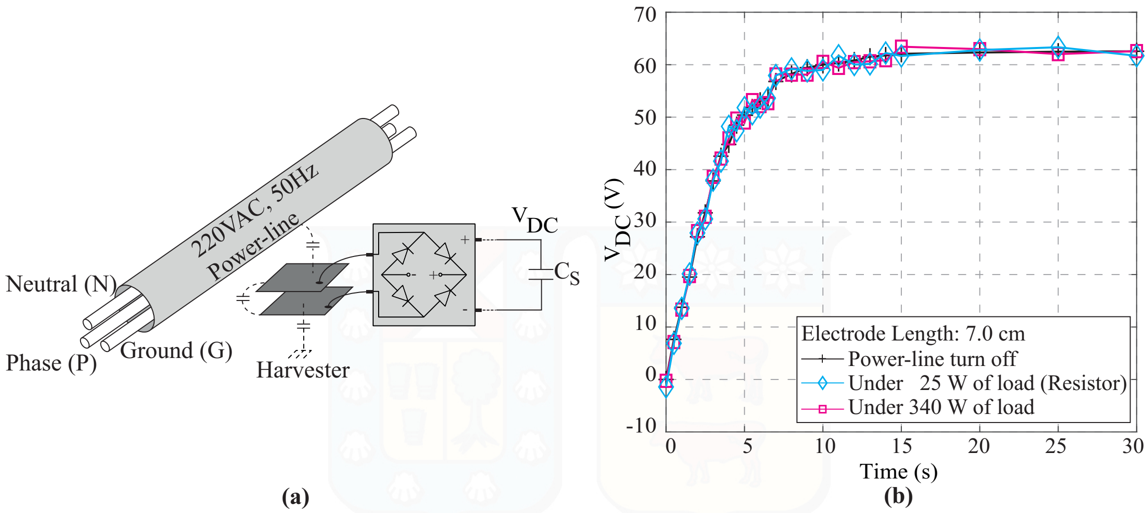

Figure 5.19: Two-plate topology analysis. **(a)** Low-voltage EFEH concept; **(b)** Charging pattern of the storage capacitor C_S with respect to the attached loads

5.3.1.1 Two-Plate Topology

The two-plate topology has several advantages, mainly in non-contact applications. This technology can be used in mobile applications, where the device is able to change its position. The principle EFEH can operate on even a no-load/open-circuit AC power line. In such a case, the two-plates harvester may be an outstanding technology to operate wireless sensor nodes without constraints. The corroborative results are shown in Fig. 5.19b, where the voltage gathered increases evenly both in open-circuit and energized power-lines. This advantage makes those electric-field harvesters are an attractive option to energize circuit in power system environments.

The material that forms the harvester's electrodes directly influences on the maximum power available, as shown in Fig. 5.20a. The experimental findings show that the performance of copper electrodes is better than aluminum electrodes because the harvesting performance is directly associated with the electrical characteristics of the material. The measurement results show that copper outperforms aluminum by collecting more charges, approximately 30% more, in the same charging cycle. This improvement can be exploited in order to reduce the energy transmission process between the harvester and the loading system. On the other hand, the measurement results in Fig. 5.20b and Fig. 5.21a show that the power available depends on the harvester's length and the distance between electrodes and power-line. It is possible to see that there is a reduction of more than 80% when the electrodes are separated to the power line at 3 mm. However, the energy reduction is fast to the first centimeters and it becomes slow in accordance with the increment of the distance between the harvester and the power-line, as seen in Fig. 5.21b.

5.3.1.2 Cylindrical Topology

In the literature, the most common configuration of the electric-field harvester is based on the cylindrical topology. An important advantage is related to its tubular geometry, which

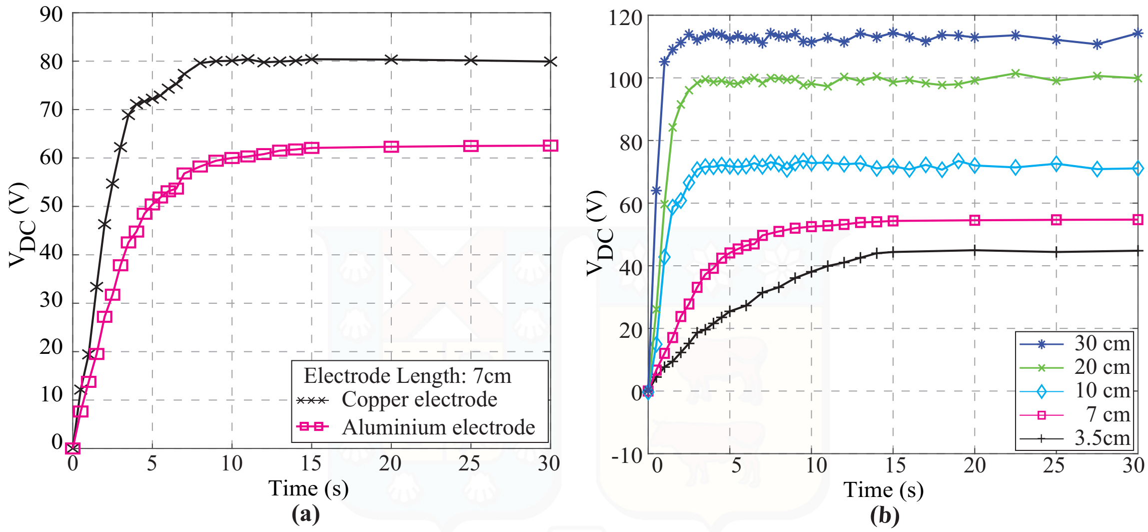

Figure 5.20: Two-plate topology analysis. **(a)** Charging pattern of the storage capacitor C_S with respect to electrode material; **(b)** Charging pattern of the storage capacitor C_S with respect to aluminum plate length, under the open-circuit condition.

enables to easily adapt the device to the power-line. In middle/high voltage applications, this characteristic causes important constraints, due to the fact that the mechanism is directly mounted on the power line, requiring more sophisticated protection systems. In low-voltage applications, the main restriction is related to energized wires distribution at home, and the possibility of accessing to them.

To evaluate the performance of the cylindrical topology, the experiment, shown in Fig. 5.22a, was developed. A variable section of the energized wire (3 wires, Phase-Ground-Neutral) was wrapped with aluminum, creating a cylindrical structure. The main objective of the model is to drain I_d and collect the charges in the storage capacitor C_S. The storage capacitor is of 1 μF in order to reduce the charging time. The analysis was developed under no load (open circuit condition). The empirical findings show that harvesting considerably more energy depends on the harvester's length, as shown in Fig. 5.22b. The measuring results in Fig. 5.22b show that a harvester of 30 cm out-performs a harvester of 7 cm by collecting more charges, approximately 100 percent more, in the same charging period.

5.3.1.3 Multi-harvesters based on cylindrical topology

As Fig. 5.22b suggests, the harvester's length should be increased as much as possible to extract more power from the electric field. However, this is often impractical due to the fact that energized wires are not fixed and may be distributed quite irregularly in the homemade. As a solution, the harvester may be split into several smaller harvesters, which can be independently connected to the energy conversion system, as shown in Fig. 5.23a. This configuration aims to maintain the amount of available energy, as shown in Fig. 5.23c. However, the main disadvantage is related to the wiring between the harvester and rectifier circuit, which significantly increases, and sometimes is unfeasible.

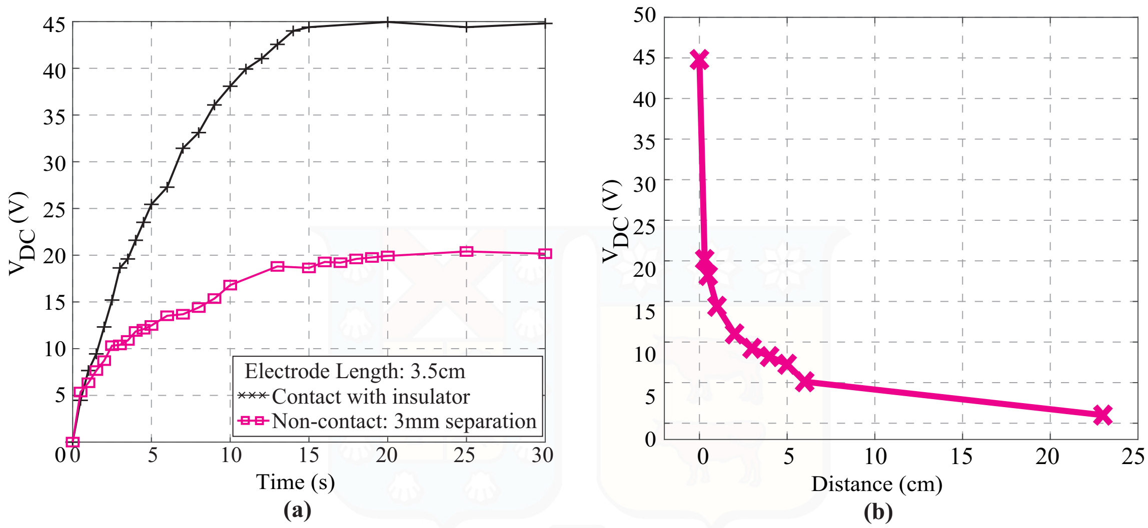

Figure 5.21: Two-plate topology analysis. **(a)** Comparison of the maximum voltage V_{DC} based on distance to power-line; **(b)** Charging pattern of the storage capacitor C_S with respect to the power-line distance, under the open-circuit conditions.

Therefore, the configurations based on a horizontal increment of the harvester's length are not always applicable because of previously analyzed limitations. These constraints inspire the idea of vertical expansion instead of horizontal increment. With this aim, a multi-layer configuration was developed, as shown in Fig. 5.23b. Figure 5.23d shows the charging pattern on the storage capacitor C_S of the multi-layer harvesters. It is possible to note that the double-layer harvester collects more than 47% of the voltage collected by the single-layer harvester. In other words, the double-layer concept has an increment of 118% in the stored energy in C_S. Therefore, the empirical results show that the multi-layer harvester can harvest considerably more energy with reduced volume. Although the energy increases with the number of layers, the empirical findings show that n-layers configuration does not have a significant impact on the available energy regarding the double-layer harvester. Finally, based on the amount of material used, it is possible to observe a reduction of 50% in the stored energy by the double-layer harvester.

5.3.2 Energy Harvested Based on Electrode Separation

The storage capacitor's charging time may vary depending on the electric field distribution and the positioning of electrodes. In other words, the system delivers power to the load with a variable frequency. This frequency is related to the power stored in the electrodes and the charging current of the storage capacitor. Figure 5.24a shows the behavior of the storage capacitor's power when the device varies the electrodes separation in three different electric field distributions. Both the power and current of the storage capacitor in the charging stage have similar behaviors and vary depending on the electrodes separation for each test. The results are shown in Fig. 5.24b and Fig. 5.24c, respectively. Figure 5.24d shows the stored energy for one time period, all cases show a similar behavior due to the experiment characteristics. However, despite the similar results the frequency varies.

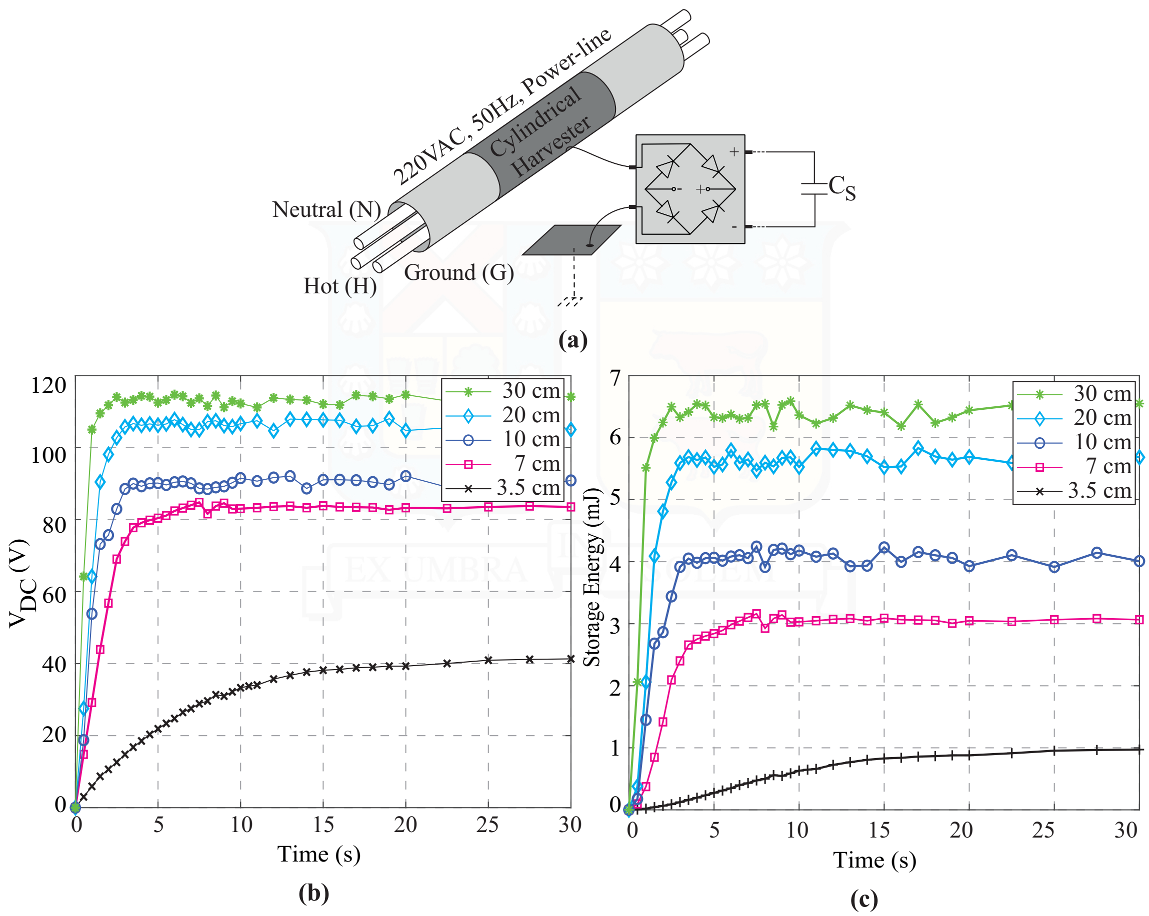

Figure 5.22: Cylindrical topology analysis. **(a)** Low-voltage EFEH concept; **(b)** Charging pattern of the storage capacitor C_S with respect to aluminum tube length, under the open-circuit condition.

The power obtained from the harvester depends on the separation of the electrodes and the electric field distribution. This section analyses the effect of resistive loads on the power transfer as a basis for understanding the system under loading. In addition, we provide the main conditions for power transfer maximization, analyzing a general case (an electronic converter is the load). The steady state AC circuit analysis of the capacitor divider shown in Fig. 5.9c was performed with a resistor R connected between electrodes. The average delivered power P_o is given by

$$P_o = \frac{R_L {\omega_o}^2 {C_{eq}}^2 {V_{eq}}^2}{1 + {\omega_o}^2 {R_L}^2 \left(C_H + C_{eq}\right)^2} \tag{5.30}$$

where,

$$C_{eq} = \frac{(C_{GS\,1} + C_{GN1} + C_{PS\,1})\,(C_{GS\,2} + C_{GN2} + C_{PS\,2})}{C_{GS\,1} + C_{GN1} + C_{PS\,1} + C_{GS\,2} + C_{GN2} + C_{PS\,2}}$$

$$V_{eq} = V_{line}\left(\frac{C_{PS_1}}{C_{PS_1} + C_{GS_1} + C_{GN_1}} - \frac{C_{PS_2}}{C_{PS_2} + C_{GS_2} + C_{GN_2}}\right)$$

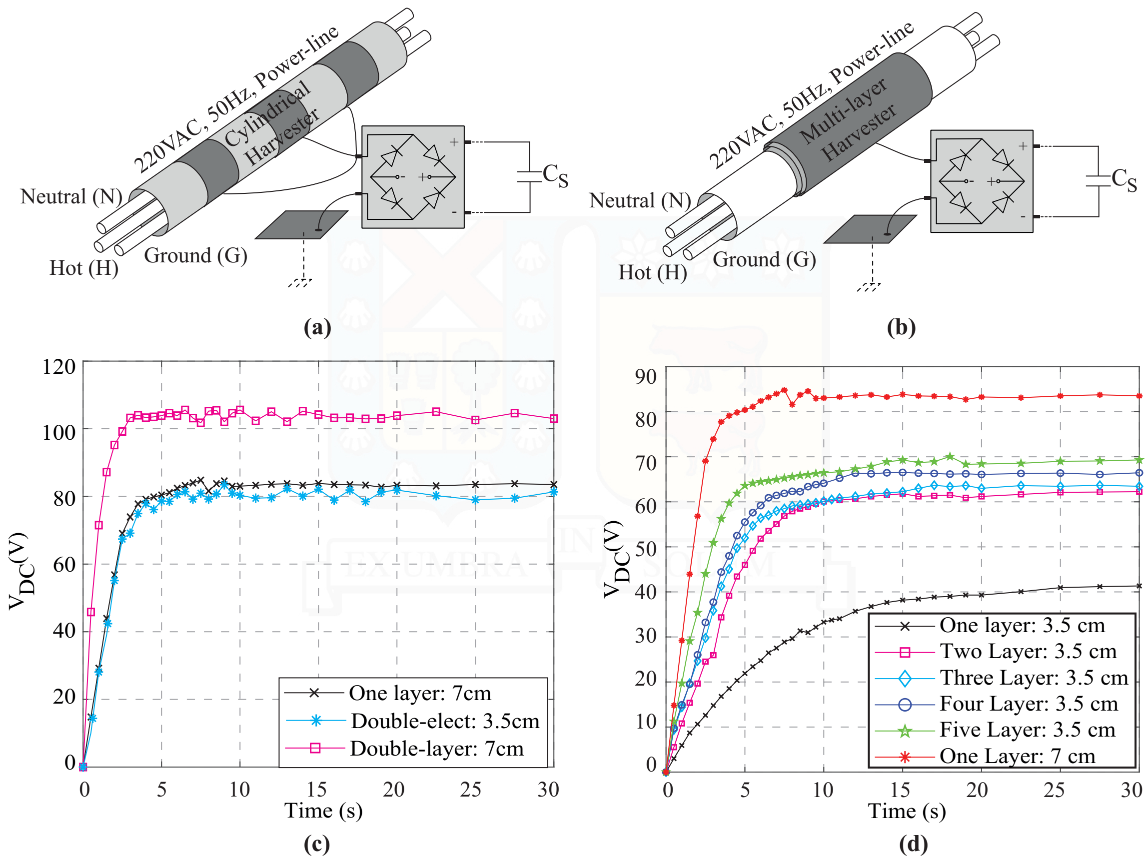

Figure 5.23: Multi-harvesters based on cylindrical topology: Multi-layer and Multi-electrodes **(a-b)** Low-voltage EFEH concept; **(c)** Comparison of single, double-layer and double-electrodes formations, under no load condition; **(d)** Charging pattern of the storage capacitor C_S with respect to aluminum tube length, under the open-circuit condition.

Capacitors $C_{GS\,i}$, $C_{GN\,i}$ and $C_{PS\,i}$ depend only on the geometry of the harvester as observed in (5.5). Regarding to C_H, although its minimum value depends on the geometry of the harvester, any element connected across its terminals affects the capacitance, thus it cannot be considered constant. Hence, the load resistor R and the capacitance of the harvester C_H are the freedom degrees for a fixed line-to-ground reference voltage V_{line}. In addition, the resistors could be replaced by a set of different electronic converters (e.g. diode, bridge, DC-DC converter). Therefore, it is necessary to find the maximum power point, by varying the freedom degrees.

Depending on the electric field distribution and the positioning of the harvester C_H, the storage capacitor charging time can vary. In other words, the system delivers power to the load with variable frequency. This frequency is related to the power stored in the electrodes and the charging current of the storage capacitor. Figure 5.24a shows the behavior of the storage capacitor power when the device varies the electrodes separation in three different electric field distributions. The power and current of the storage capacitor in the charging stage have a similar behavior, and vary depending on electrodes separation for each test. The results are shown in Fig. 5.24b and Fig. 5.24c, respectively. Figure 5.24d

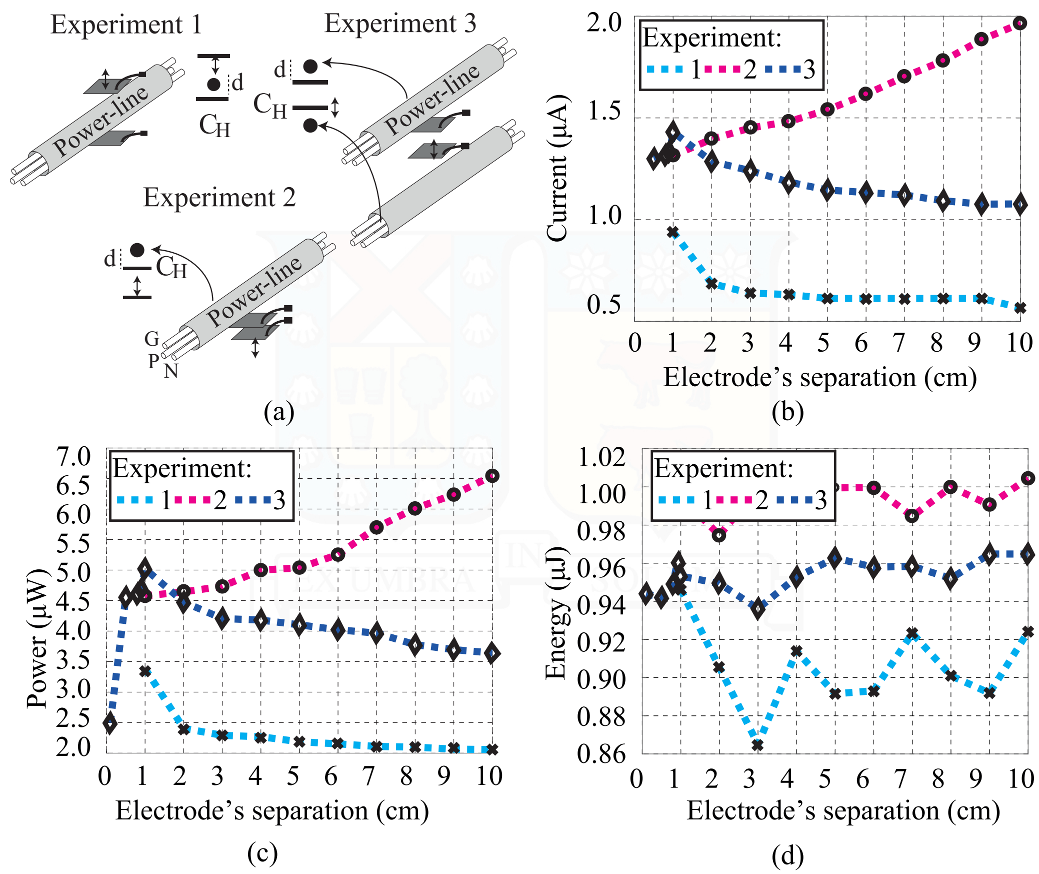

Figure 5.24: Experimental results of capacitive harvester located on different electric fields. **(a)** Experiment schematics; **(b)** Storage capacitor current; **(c)** Load power; **(d)** Energy in one period.

shows the stored energy for one time period, all cases show a similar behavior due to the experiment characteristics. However, despite the similar results the frequency varies.

5.3.2.1 Maximum Power Point Tracking

The modeling of an electric field harvester (C_{EF} and i_{EF}) and the calculation of the electric induction caused by a source from the electric field is extremely complicated because the feasibility to determine the maximum power point (MPP) is limited by the electric field irregular distribution. In this context, a variation of a Perturb and Observe (P&O) algorithm is proposed, which allows finding the maximum power point in a fast and simple manner. The proposed P&O algorithm measures the voltage v_{C_S} and the current i_{C_S} in the storage capacitor C_S in each instant time during a period. With this information, the algorithm estimates the instantaneous power and computes the average power. However, the measurement of the charging capacitor current is highly complex due to the fact that this current is very small (tens of nA). As a solution, the algorithm estimates the capacitor's current using the measured voltage and the Taylor approximation, as follows,

$$i_{C_S}(k) = C_S \times \frac{v_{C_S}(k) - v_{C_S}(k-1)}{\Delta T_1} \tag{5.31}$$

where C_S is the capacitance of the storage capacitor, $v_{C_S}(t)$ is the storage capacitor voltage at time k and ΔT_1 is the time between two measurements.

Although the voltage rectified V_{C_S} has exponential growth, it is possible to consider as a linear voltage in the full-bridge rectifier case, due to the fact that the maximum power point for the full-bridge rectifier is given at is $V_{C_{S\,opt}} = V_{EF}/2 - V_D$. In this case, it is worth noting that the storage capacitor's current is proportional to the time between two energy transfer cycles $i_{C_S}(k) = \frac{k_1}{\Delta T}$, where k_1 is a constant value and ΔT is the time between two energy transfer cycles. In addition, the variation of the power also directly depends on the frequency $\overline{P} = \frac{k_2}{\Delta T}$, where k_2 is a constant value and ΔT is the time between two energy transfer cycles. Depending on the average power, the device runs the corresponding action in electrodes. The procedure to find the MPP is summarized in general Algorithm 1.

Algorithm 1 Maximum power point tracking

1: Set the value of the perturbation $\Delta A = 0.25$ cm
2: **while** $S_1 = 0$ **do**
3: Measure the capacitor's voltage $v_{C_S}(k)$
4: Estimate the capacitor's current using $i_{C_S}(k) = C_S \frac{v_{C_S}(k) - v_{C_S}(k-1)}{\Delta T_1}$
5: Compute the instantaneous capacitor's power as $p(k) = v_{C_S}(k)\, i_{C_S}(k)$
6: **end while**
7: Compute the average power $P(k') = \frac{1}{\Delta T}\int_0^{\Delta T} p(t)\, dt$
8: **if** $P(k') > P(k'-1)$ **then**
9: **if** $A(k') > A(k'-1)$ **then**
10: $A^*(k') = A(k'-1) + \Delta A$
11: **else**
12: $A^*(k') = A(k'-1) - \Delta A$
13: **end if**
14: **else**
15: **if** $A(k') > A(k'-1)$ **then**
16: $A^*(k') = A(k'-1) - \Delta A$
17: **else**
18: $A^*(k') = A(k'-1) + \Delta A$
19: **end if**
20: **end if**

Briefly, the line of code (1) sets the perturbation step value ΔA, which is selected by analyzing the maximum oscillations around the MPP and the speed of convergence. Reducing the perturbation step size minimizes the oscillations. However, a small perturbation step reduces the algorithm's convergence speed. Lines of code (2)–(6) compute the instant output power between two energy transfer cycles. The MPPT algorithm periodically increments and decrements the separation between harvester plates. Lines of code (7)-(20) analyze the effect of perturbations in the output power. If a defined perturbation leads to an output power increment, then the next perturbation is applied in the same direction. Otherwise, if a given perturbation leads to an output power reduction, the subsequent perturbation is applied in the opposite direction. Once the system determines the MPP, the algorithm calculates the trigger voltage under these conditions and the servomotor is

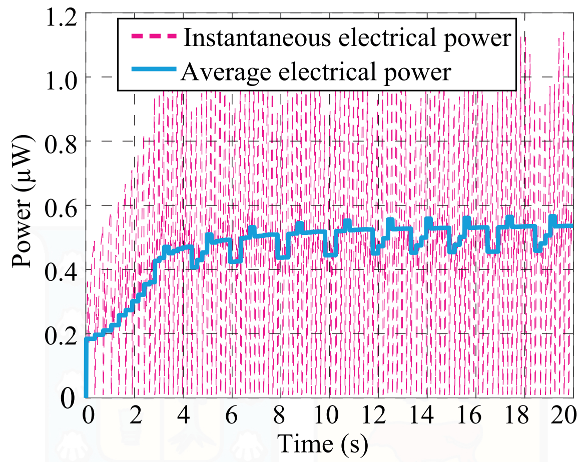

Figure 5.25: Power harvested with the proposed approach. The system is located at 2 cm from the wires.

disconnected. The behavior of the system, when the device is located at 2 cm is shown in Fig. 5.25. It is possible to note that the P&O algorithm once it detects the maximum power point, keeps oscillating around this point, due to the automatic variation of the separation between electrodes.

To verify the feasibility and measure the performance of the two-electrodes harvesting system, a system based on EFEH concept was prototyped. Unlike the predecessor device used to validate the concept, the new prototype has two mobile plates controlled by a servomotor. This characteristic provides more flexibility and robustness to the sensor against electric field variations. Figure 5.26 shows the sensor behavior when it is placed at a fixed position and change the electric field around it. We selected ΔA = 0.25 cm since the system should be able to achieve the MPP in the shortest amount of time. If we select $\Delta A < 0.25$ cm, the system could remain enclosed in a local maximum, thus impeding the MPP detection or increasing its detection time. Otherwise, if we select $\Delta A > 0.25$ cm, there is an increase in the possibility that the system cannot detect the maximum due to high variations.

The storage capacitor's voltage is shown in Fig. 5.26a. It is possible to note that the voltage oscillates between 1.1 V and 5.5 V due to the charging and discharging of the capacitor. An important disadvantage is related to negative storage capacitor currents that are related to noise effects. In this context, we filtered the current in order to reduce this phenomenon, as shown in Fig. 5.26b. Electric field variations affect the harvested power as shown in Fig. 5.26d, the system addresses this problem by adjusting the separation between electrodes, as shown in Fig. 5.26c. It is possible to note that the system extracts the maximum power all the time, as shown in Fig. 5.26d.

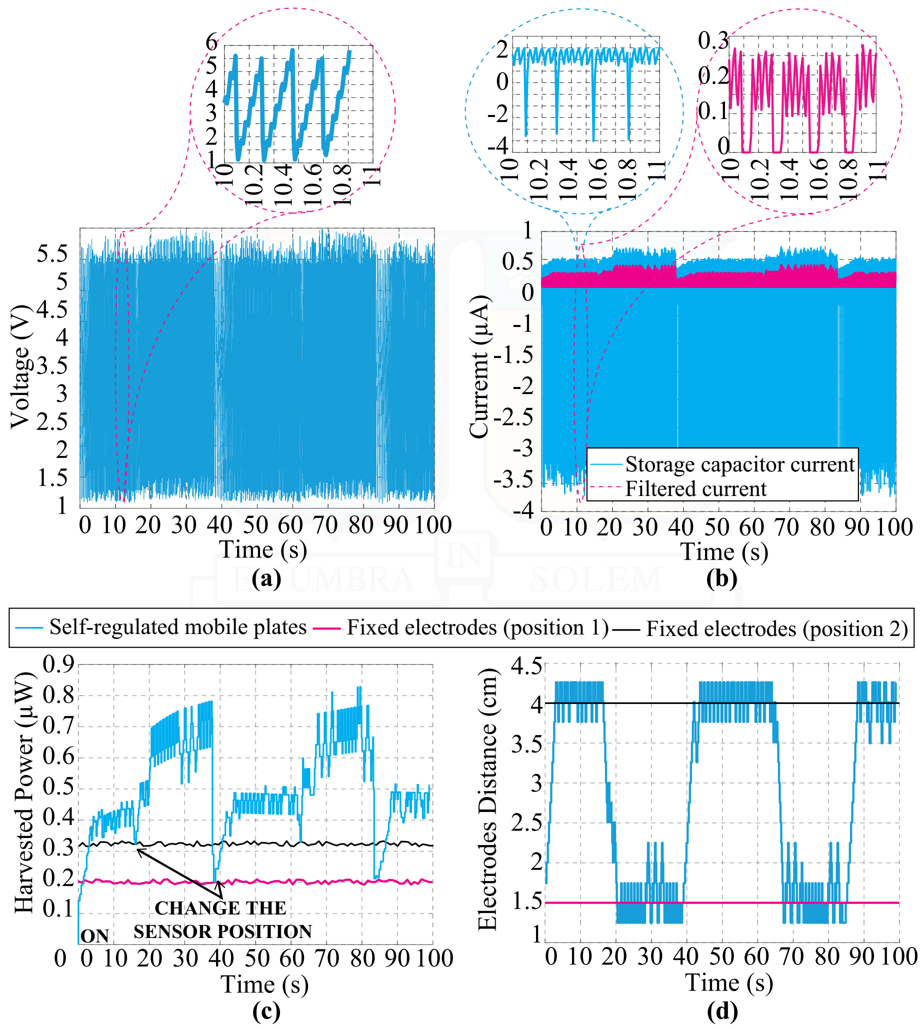

Figure 5.26: Power harvested with proposed approach. The system is located at different distances from the wires. **(a)** Storage capacitor voltage; **(b)** Storage capacitor current; **(c)** Separation between electrodes; **(d)** Power harvested.

5.4 Contributions

This chapter presented a comprehensive review of electric field energy harvesting proposal and focused on how to implement and optimize existing methods on low-voltage to enable self-sustainable smart drones and smart houses. A low-power design methodology to reduce power dissipation and to increase the harvested power, and corresponding guidelines have been providing for the design of a more enhanced harvesting procedure. In addition, this chapter presented the analysis of the maximum power available for different energy management circuits (full-bridge, voltage doubler, and parallel switch-only rectifier). Likewise, the impacts of the capacitive coupling design in the extracted energy. Experimental results imply that the electric field energy harvesting is a promising solution to built wireless sensor nodes with greater longevity, higher robustness, larger throughput, and improved flexibility, which opens up the potential of distributing more sensors and enabling more parameters to be gathered conveniently. In addition, a novel two-plate harvester provided with a mechatronized maximum power point system was presented. The system harvests the electric field around an energized wire. Experimental results imply that the proposed system is capable of positioning the electrodes in such a way that the device can work in the maximum power point, independently of the electric field distribution.

Chapter 6
CONCLUSIONS AND FUTURE WORK

6.1 Conclusion

The monitoring of power system asset –including conductors, protection systems, towers, transformers, and other electrical devices– plays a key role to address the growing need for sustainable energy worldwide. Despite their commercial immaturity, robots used in power systems are well positioned to serve both niche (e.g. inspection and maintenance of transmission lines) and more generalized applications. This thesis presented a meticulous analysis and several applications of robotic perception in for characterization, autonomous navigation, and self-sustainability in power system applications. The review of state-of-the-art enabled us to establish the main links and gaps between power systems and robotics, as well as, the most important challenges of the power system robots focused on inspection and maintenance practices.

Power system robotics can be equipped with a variety of advanced sensors (e.g. cameras, LIDAR, and dedicated sensors), which collect an assortment of data simultaneously. The robot must be capable of interpreting and characterizing the most representative artifacts associated with the power system functionalities using provided information by these sensors. To this end, a photovoltaic module fault diagnosis algorithm based on infrared thermography was proposed and experimentally assessed. The two-stage algorithm is able to detect hot-spots associated with PV-module failures and to eliminate false hot-spots in a suite of visual and infrared images acquired with a commercial thermal camera. On completion of the analysis, the system returns a 3D thermal and visual characterization of the PV-structure studied. Field testes enabled to validate the proposed system as a novel tool to assess the condition of modules with noninvasive sensors. The experimental findings showed an accuracy of 94.05% in the detection of PV-modules. On the other hand, the algorithm had an accuracy of 94.19% in the detection of hot-spots. Likewise, the proposed diagnostic approach can improve existing methods in 12% of effectiveness.

An important characteristic of robotic platforms used to monitor power systems is the capacity of performing inspection and maintenance practices in extreme situations, in which other methods cannot be used. However, the electrical environment can affect several sensing systems (e.g. GNSS), affecting critical processes such as navigation or localization.

This thesis has addressed this issue through the development and experimental validation of a visual-based navigation system for transmission grid inspection UAVs. The system incorporates a novel algorithm that determines the drone's position through the analysis of geometrical patterns associated with power-lines. Due to the fact that the proposed system analyzes the geometric patterns of power-lines, the previous training is not necessary. Among the other methodologies proposed in the literature for this application, the main contribution in this topic is the use of a low-cost sensor to get high accuracy targeting rates (approximately 91.44%) using a medium training data-set. Likewise, experimental results showed that the localization achieves a very high precision regarding transmission lines. The worst studied cases showed an error of 1.5 cm and 71 cm in laboratory and field test respectively. In terms of RMSE, significant improvements are achieved using the hybrid approach. The worst analyzed test showed an error of 27 cm.

On the other hand, the robotic platform must be capable of running during long working periods and do it autonomously. Among the most notable challenges, the energy constraints can be placed at the top. This thesis addresses this challenge through analysis of the electric field energy harvesting methods, focusing on the fundamental conditions for the optimization of the power extracted from an EFEH system. A novel methodology and corresponding guidelines have been provided for the design of more enhanced harvesting procedures based on capacitive coupling and rectifier improving. From the research regarding electric field energy harvesting, the most outstanding benefits obtained from theoretical, simulation and experimental evaluations are:

- The theoretical analysis has identified that the electric field harvester functions as an AC high impedance current source. The proposed model was validated through simulations and field tests.
- Electric field energy harvesting is the only technology that has the capacity of functioning both in open-circuit and energized power lines. Experimental findings showed that a cylindrical harvester (20 cm length) can store 7 mJ in approximately 5 minutes. On the other hand, a two-plate harvester (20 cm of side) can store 5 mJ in the same period of time. This energy can be used to intermittent power an ultra-low power wireless networking chipset.
- The amount of power available in for an electric harvester is related to its size. Because of the design and assembly constraints, the vertical expansion appears as a viable solution for more powerful harvesters. Empirical results showed that harvesting more energy with reduced volume is practically attainable.
- The empirical findings showed that a two-plate harvester (7 cm of side) in contact with the energized power line outperforms another one separated 3mm to the energized wire by collecting more charges, approximately 80%. In other words, contactless applications reduce considerably the power available.
- The merit of using electric field harvesters as a reliable power supply depends on the implementation of low power management strategies. The three topologies proposed in this Thesis (full-bridge rectifier, voltage-doubler, and parallel switch-only rectifier) showed that the maximum power available is a direct function of the storage

capacitor's voltage. The main advantage of full-bridge rectifier topology is that the current flows into the load every half-cycle. Both full-bridge and voltage-doubler topologies can provide the same maximum power. However, the power output by a voltage doubler circuit reaches a maximum at twice the value of the maximum for a full-bridge rectifier. Furthermore, the voltage-doubler topology reduces the number of diodes by two and also shares a common ground with the electric field harvester. Parallel switch-only rectifier takes advantage of the main characteristics of these two topologies, increasing the maximum output power available two times.

- A novel electric field harvester was proposed. The system incorporates a maximum power point tracking algorithm based on distance separation between electrodes. Experimental results showed that the proposed system is able to position the plates in such a way that the device can work in the maximum power point, independently of the electric field distribution.

6.2 Future work

Despite achieving acceptable results and the ongoing research activities in robotic platforms in power systems, there are still several open points which have to be covered in future research work. The most important points in the context of this Thesis are as follows,

- **Robust inspection**
  The algorithms based on the use of geometric patterns to determine the PV-surface are fast but sometimes can return erroneous results. The proposed methodology can be extended using Semantic segmentation algorithm based on convolutional neural networks (CNNs). However, the use of CNNs requires more complex processing systems and extended database. On the other hand, the use of other camera technologies (multispectral and/or hyperspectral) can improve the hot-spot detection algorithm. Regarding the 3D characterization, the static mounting designed for this thesis is an important limiting aspect. The new versions must be mounted on robotic systems in order to evaluate the behavior under movement threats (blurring, vibrations, etc.).

- **Improvement navigation**
  A navigation strategy of an UAV consists of two stages: **(i)** Power line detection and **(ii)** Electrical tower detection. Regarding to the first objective, an important constraint of the visual system is related to lighting conditions. The system cannot operate at night. In this context, the use of thermographic cameras could improve the drone's perception under reduced vision conditions. On the other hand, the algorithm must be extended in order to detect transmission lines with other distributions. To this end, the variation of Hough transform or other machine learning algorithms can be used. The second goal can be performed using deep learning algorithms. Current studies have demonstrated that an algorithm based on Support Vector Machines and YOLO Neural Network has a very high accuracy in the electric tower detection.

- **Electric field energy harvesting conversion system**
  Although the chapter on electric field energy harvesting presented new rectifier

techniques to improve power obtained from the harvester, the development of a maximum power point tracking algorithm based on the theoretical analysis has not been implemented. The design and implementation of this circuit could be an interesting future application. Likewise, the development of management energy circuits that are capable of working with small electrodes is an open challenge. The current empirical advances related to this topic have shown that the use of bidirectional switch connected in serial connection with the harvester increases the output power available in 12%.

6.3 Summary of Contributions

- O. Menéndez, M. Pérez and F. Auat Cheein, "Vision based inspection of transmission lines using unmanned aerial vehicles," 3rd International Seminar on Energy Management in Mining, Santiago-Chile, 2016, Chapter 3.
- O. Menéndez, M. Pérez and F. Auat Cheein, "Vision based inspection of transmission lines using unmanned aerial vehicles," 2016 IEEE International Conference on Multisensor Fusion and Integration for Intelligent Systems (MFI), Baden-Baden, 2016, pp. 412-417. doi: 10.1109/MFI.2016.7849523
- O. Menéndez, F. Auat Cheein, M. Pérez and S. Kouro, "Robotics in Power Systems: Enabling a More Reliable and Safe Grid," in IEEE Industrial Electronics Magazine, vol. 11, no. 2, pp. 22-34, June 2017. doi: 10.1109/MIE.2017.2686458
- O. Menéndez, M. Pérez and F. Auat Cheein, "Photovoltaic Modules Diagnosis Using Artificial Vision Techniques for Artifact Minimization," Energies, 2018, 11, 1688. doi: 10.3390/en11071688
- O. Menéndez, M. Pérez and F. Auat Cheein, "Visual-Based Positioning of Aerial Maintenance Platforms on Overhead Transmission Lines," Applied Science, 2019, 9, 165. doi: 10.3390/app9010165
- F. Auat Cheein, M. Pérez and O. Menéndez, "Sistemas de Inspección de Líneas de Transmisión de Alta Tensión usando Drones Autónomos," Premio Mejor Innovación 2016 - Asociación de la Industria Eléctrica – Electrónica de Chile (AIE)

Bibliography

[1] Systep. Apagón en el Sistema Interconectado Central. http://www.centralenergia.cl/2011/10/19/apagon-en-el-sistema-interconectado-central, 2011. [Online; accessed 30-September-2015]. 1.1

[2] D. P. Kothari and I.J. Nagrath. *Modern Power System Analysis*. Tata McGraw Hill, 2009. 1.1

[3] L. Grigsby. *Electric Power Engineering Handbookl*. Taylor & Francis Group, 2016. 1.1

[4] Heloisa Cunha Furtado and Iain Le May. High temperature degradation in power plants and refineries. *Materials Research*, 7:103 – 110, 03 2004. 1.1

[5] Mohd Shawal Jadin and Soib Taib. Recent progress in diagnosing the reliability of electrical equipment by using infrared thermography. *Infrared Physics & Technology*, 55(4):236 – 245, 2012. 1.1

[6] Joon-Young Park, Jae-Kyung Lee, Byung-Hak Cho, and Ki-Yong Oh. An inspection robot for live-line suspension insulator strings in 345-kv power lines. *Power Delivery, IEEE Transactions on*, 27(2):632–639, April 2012. 1.1, 2.2.0.1

[7] H. Zhang, Y. He, B. Gao, G. Y. Tian, L. Xu, and R. Wu. Evaluation of atmospheric corrosion on coated steel using k -band sweep frequency microwave imaging. *IEEE Sensors Journal*, 16(9):3025–3033, May 2016. 1.1

[8] C.H. Liu, J. Chen, Y.X. Lai, D.H. Zhu, Y. Gu, and J.H. Chen. Enhancing electrical conductivity and strength in al alloys by modification of conventional thermo-mechanical process. *Materials & Design*, 87:1 – 5, 2015. 1.1

[9] S. Refsnæs, N. Magnusson, and T. Ulleberg. Laboratory corrosion tests on overhead line conductors with bird protection systems. *International Transactions on Electrical Energy Systems*, 24(8):1185–1191, 2014. 1.1

[10] William Pentland. Blackout risk tool puts price tag on power reliability, 2013. [Online; accessed 23-October-2017]. 1.1

[11] P. Henneaux, P. E. Labeau, and J. C. Maun. Blackout probabilistic risk assessment and thermal effects: Impacts of changes in generation. *IEEE Transactions on Power Systems*, 28(4):4722–4731, Nov 2013. 1.1

[12] C. De Michelis, C. Rinaldi, C. Sampietri, and R. Vario. 2 - condition monitoring and assessment of power plant components. In John E. Oakey, editor, *Power Plant Life Management and Performance Improvement*, Woodhead Publishing Series in Energy, pages 38 – 109. Woodhead Publishing, 2011. 1.1

[13] E. Csanyi. Guidelines For The Construction And Maintenance Of Transmission Lines. http://electrical-engineering-portal.com/guidelines-for-the-construction-and-maintenance-of-transmission-lines, 2013. [Online; accessed 19-August-2016]. 1.1, 2.3.0.3

[14] E. Head. High-value cargos, 2015. [Online; accessed 19-August-2016]. 1.1, 2.3.0.3

[15] O. Menendez, F. A. Auat Cheein, M. Perez, and S. Kouro. Robotics in power systems: Enabling a more reliable and safe grid. *IEEE Industrial Electronics Magazine*, 11(2):22–34, June 2017. 1.1, 1.1, 1.1, 5, 5.1

[16] Binhai Wang, Rui Guo, Bingqiang Li, Lei Han, Yong Sun, and Mingrui Wang. Smartguard: An autonomous robotic system for inspecting substation equipment. *Journal of Field Robotics*, 29(1):123–137, 2012. 1.1, 1.1, 2.2.0.2

[17] Pouliot and Serge Montambault. Field-oriented developments for linescout technology and its deployment on large water crossing transmission lines. *Journal of Field Robotics*, 29(1):25–46, 2012. 1.1

[18] Gilles Caprari, Andreas Breitenmoser, Wolfgang Fischer, Christoph Hürzeler, Fabien Tâche, Roland Siegwart, Olivier Nguyen, Roland Moser, Patrick Schoeneich, and Francesco Mondada. Highly compact robots for inspection of power plants. *Journal of Field Robotics*, 29(1):47–68, 2012. 1.1

[19] C. A. Veerappan, P. R. Green, and S. M. Rowland. Visual live-line condition monitoring of composite insulators. In *2010 1st International Conference on Applied Robotics for the Power Industry*, pages 1–6, Oct 2010. 1.1, 2.1, 2.3.0.2

[20] L. C. Siebert, L. F. R. B. Toledo, P. A. B. Block, D. B. Bahlke, R. A. Roncolatto, and D. P. Cerqueira. A survey of applied robotics for tree pruning near overhead power lines. In *Proceedings of the 2014 3rd International Conference on Applied Robotics for the Power Industry*, pages 1–5, Oct 2014. 1.1, 2.1

[21] J. Katrasnik, F. Pernus, and B. Likar. A survey of mobile robots for distribution power line inspection. *IEEE Transactions on Power Delivery*, 25(1):485–493, Jan 2010. 1.1, 2.1, 2.2.0.1, 2.2.0.2

[22] Zhengrong Li, Troy S. Bruggemann, Jason J. Ford, Luis Mejias, and Yuee Liu. Toward automated power line corridor monitoring using advanced aircraft control

and multisource feature fusion. *Journal of Field Robotics*, 29(1):4–24, 2012. 1.1, 2.2.0.3

[23] C.W. Devine and D.N. O'Connell. Boom mountable robotic arm, April 1 2014. US Patent 8,684,333. 1.2, 2.3.0.2

[24] R.A. Roncolatto, N.W. Romanelli, A. Hirakawa, O. Horikawa, D.M. Vieira, R. Yamamoto, and V.C. Finotto. Robotics applied for safety improvement in the power distribution lines maintenance. In *Transmission and Distribution Conference and Exposition, 2008. T x00026;D. IEEE/PES*, pages 1–7, April 2008. 1.2, 2.3.0.2

[25] R Aracil, M Ferre, M Hernando, E Pinto, and J.M Sebastian. Telerobotic system for live-power line maintenance: Robtet. *Control Engineering Practice*, 10(11):1271 – 1281, 2002. 1.2, 2.3.0.2

[26] MIR Innovation. LINEROVER – A COMPACT ROBOT FOR INSPECTING OVERHEAD LINES. http://mir-innovation.hydroquebec.com/mir-innovation/en/transmission-solutions-linerover.html, 2016. [Online; accessed 29-November-2016]. 1.2, 2.1, 2.2.0.1

[27] HIBOT CORP. Expliner - Robot for power line inspection. https://www.hibot.co.jp, 2016. [Online; accessed 29-November-2016]. 1.2, 2.1, 2.2.0.1

[28] MIR Innovation. LINESCOUT – A VERSATILE ROBOT FOR INSPECTING OVERHEAD LINES. http://mir-innovation.hydroquebec.com/mir-innovation/en/transmission-solutions-linescout.html, 2016. [Online; accessed 29-November-2016]. 1.2, 2.1, 2.2.0.1

[29] HEXAGON GEOSYSTEMS. AIBOTIX. https://www.aibotix.com/, 2016. [Online; accessed 15-December-2016]. 1.2, 2.1, 2.2.0.3

[30] Chi Chen, Bisheng Yang, Shuang Song, Xiangyang Peng, and Ronggang Huang. Automatic clearance anomaly detection for transmission line corridors utilizing uav-borne lidar data. *Remote Sensing*, 10(4), 2018. 1.2

[31] K. Isawa, S. Nakayama, M. Ikeda, S. Takagi, S. Tosaka, and N. Kasai. Robotic 3d squid imaging system for practical nondestructive evaluation applications. *Physica C: Superconductivity*, 432(3–4):182 – 192, 2005. 1.1

[32] Yann Perrot, Laurent Gargiulo, Michael Houry, Nolwenn Kammerer, Delphine Keller, Yvan Measson, Gérard Piolain, and Alexandre Verney. Long-reach articulated robots for inspection and mini-invasive interventions in hazardous environments: Recent robotics research, qualification testing, and tool developments. *Journal of Field Robotics*, 29(1):175–185, 2012. 1.1, 2.1

[33] T. Long, M. Ozger, O. Cetinkaya, and O. B. Akan. Energy neutral internet of drones. *IEEE Communications Magazine*, 56(1):22–28, Jan 2018. 1.1

[34] DJI. Agrasmg-1. https://www.dji.com/mg-1, 2019. [Online; accessed 31-March-2019]. 1.1, 1.3

[35] Freefly Systems. Freefly Alta Pro 8. https://freeflysystems.com/alta-8/specs, 2019. [Online; accessed 31-March-2019]. 1.1, 1.3

[36] DJI. Spreading wings s1000. https://www.dji.com/spreading-wings-s1000, 2019. [Online; accessed 31-March-2019]. 1.1, 1.3

[37] A. Nemra and N. Aouf. Robust ins/gps sensor fusion for uav localization using sdre nonlinear filtering. *IEEE Sensors Journal*, 10(4):789–798, April 2010. 2

[38] J.-F. Allan and J. Beaudry. Robotic systems applied to power substations - a state-of-the-art survey. In *Applied Robotics for the Power Industry (CARPI), 2014 3rd International Conference on*, pages 1–6, Oct 2014. 2.1

[39] TERRATECH. Integrated Tree Trimming Systems. http://www.terratechmfg.com/, 2016. [Online; accessed 15-December-2016]. 2.1, 2.3.0.2

[40] Quanta Services. Quanta Energized Service. http://www.quantaenergized.com/l, 2016. [Online; accessed 19-August-2016]. 2.1, 2.3.0.2

[41] Bruce Hazel, Jean Côté, Yvan Laroche, and Patrick Mongenot. A portable, multi-process, track-based robot for in situ work on hydropower equipment. *Journal of Field Robotics*, 29(1):69–101, 2012. 2.1

[42] S. Omari, P. Gohl, M. Burri, M. Achtelik, and R. Siegwart. Visual industrial inspection using aerial robots. In *Applied Robotics for the Power Industry (CARPI), 2014 3rd International Conference on*, pages 1–5, Oct 2014. 2.1, 2.2.0.3

[43] I. Maurtua, L. Susperregi, A. Fernández, C. Tubío, C. Perez, J. Rodríguez, T. Felsch, and M. Ghrissi. Mainbot – mobile robots for inspection and maintenance in extensive industrial plants. *Energy Procedia*, 49:1810 – 1819, 2014. Proceedings of the SolarPACES 2013 International Conference. 2.1

[44] S. Montambault and N. Pouliot. The hq linerover: contributing to innovation in transmission line maintenance. In *Transmission and Distribution Construction, Operation and Live-Line Maintenance, 2003. 2003 IEEE ESMO. 2003 IEEE 10th International Conference on*, pages 33–40, April 2003. 2.2.0.1

[45] Feng Zhang, Lei Cao, Rui Guo, Liang Zhong, Juan Jia, Yonggang Jia, and Xiaoming Chi. Extended applications of linerover technology. In *Control and Automation (ICCA), 2013 10th IEEE International Conference on*, pages 1415–1418, June 2013. 2.2.0.1

[46] N. Pouliot, P. L. Richard, and S. Montambault. Linescout technology opens the way to robotic inspection and maintenance of high-voltage power lines. *IEEE Power and Energy Technology Systems Journal*, 2(1):1–11, March 2015. 2.2.0.1

[47] N. Pouliot and S. Montambault. Linescout technology: From inspection to robotic maintenance on live transmission power lines. In *Robotics and Automation, 2009. ICRA '09. IEEE International Conference on*, pages 1034–1040, May 2009. 2.2.0.1

[48] N. Pouliot, P. Richard, and S. Montambault. Linescout power line robot: Characterization of a utm-30lx lidar system for obstacle detection. In *Intelligent Robots and Systems (IROS), 2012 IEEE/RSJ International Conference on*, pages 4327–4334, Oct 2012. 2.2.0.1

[49] P.-L. Richard, N. Pouliot, and S. Montambault. Introduction of a lidar-based obstacle detection system on the linescout power line robot. In *Advanced Intelligent Mechatronics (AIM), 2014 IEEE/ASME International Conference on*, pages 1734–1740, July 2014. 2.2.0.1

[50] P. Debenest and M. Guarnieri. Expliner x2014; from prototype towards a practical robot for inspection of high-voltage lines. In *Applied Robotics for the Power Industry (CARPI), 2010 1st International Conference on*, pages 1–6, Oct 2010. 2.2.0.1

[51] Guo Rui, Zhang Feng, Cao Lei, and Yong Jun. A mobile robot for inspection of overhead transmission lines. In *Applied Robotics for the Power Industry (CARPI), 2014 3rd International Conference on*, pages 1–3, Oct 2014. 2.2.0.1

[52] Li. Zheng and Ruan. Yi. Autonomous inspection robot for power transmission lines maintenance while operating on the overhead ground wires. In *International Journal of Advanced Robotic Systems*, 2010. 2.2.0.1

[53] Andrew John Phillips, J. Mark Major, and Glynn R. Bartlett. Line inspection robot and system, March 04 2014. US Patent 8,666,553 B2. 2.2.0.1

[54] D. Elizondo, T. Gentile, H. Candia, and G. Bell. Ground based robots for energized transmission line work-technology description, field projects and technical-economical justification of their application. In *Transmission and Distribution Conference and Exposition: Latin America (T D-LA), 2010 IEEE/PES*, pages 700–705, Nov 2010. 2.2.0.2, 2.3.0.2

[55] Rui Guo, Bingqiang Li, Yutian Sun, and Lei Han. A patrol robot for electric power substation. In *Mechatronics and Automation, 2009. ICMA 2009. International Conference on*, pages 55–59, Aug 2009. 2.2.0.2

[56] Jingchuan Wang and Weidong Chen. A novel localization system based on infrared vision for outdoor mobile robot. In *Proceedings of the 2010 International Conference on Life System Modeling and Simulation and Intelligent Computing, and 2010 International Conference on Intelligent Computing for Sustainable Energy and Environment: Part III*, LSMS/ICSEE'10, pages 33–41, Berlin, Heidelberg, 2010. Springer-Verlag. 2.2.0.2

[57] H. Wu, Y. Wu, C. Liu, and G. Yang. Visual data driven approach for metric localization in substation. *Chinese Journal of Electronics*, 24(4):795–801, 2015. 2.2.0.2

[58] Peng Xiao, Mengchao Fu, Haipeng Wang, Taiping Wang, Chao Zhang, and Yongxi Li. Design of a 2d laser mapping system for substation inspection robot. In *2016 4th International Conference on Applied Robotics for the Power Industry (CARPI)*, pages 1–5, Oct 2016. 2.2.0.2

[59] I. Purkayastha, M. Tirozzi, J. Smith, and K. Monti. Mobile inspection robot, September 5 2013. US Patent 13,766,125. 2.2.0.2

[60] Z. Xueheng. The substation inspection robot, October 12 2016. CN Patent 201,610,570,004. 2.2.0.2

[61] S. Antunes and K. Bousson. Safe flight envelope for overhead line inspection. In *Applied Robotics for the Power Industry (CARPI), 2014 3rd International Conference on*, pages 1–6, Oct 2014. 2.2.0.3

[62] Jing-Jing Xiong and En-Hui Zheng. Position and attitude tracking control for a quadrotor uav. *{ISA} Transactions*, 53(3):725 – 731, 2014. 2.2.0.3

[63] W. de Britto Vidal Filho and A.M. de Almeida Pinto. Vtol aerial robot for inspection of transmission line. In *Applied Robotics for the Power Industry (CARPI), 2014 3rd International Conference on*, pages 1–4, Oct 2014. 2.2.0.3

[64] J.T.F.B. de Sousa, B.C. Pinheiro, and U.F. Moreno. Unmanned vehicles network: Platforms and software toolchain. In *Applied Robotics for the Power Industry (CARPI), 2014 3rd International Conference on*, pages 1–6, Oct 2014. 2.2.0.3

[65] S. Pirbodaghi, D. Thangarajan, Teo Hung Liang, M. Shanmugavel, V. Ragavan, and J. S. Sequeira. A cooperative heterogeneous unmanned autonomous systems solution for monitoring and inspecting power distribution system. In *2015 International Conference on Control, Instrumentation, Communication and Computational Technologies (ICCICCT)*, pages 495–502, Dec 2015. 2.2.0.3

[66] Q. Wu and J. An. An active contour model based on texture distribution for extracting inhomogeneous insulators from aerial images. *IEEE Transactions on Geoscience and Remote Sensing*, 52(6):3613–3626, June 2014. 2.2.0.3

[67] J. Zhang, H. Shan, X. Cao, P. Yan, and X. Li. Pylon line spatial correlation assisted transmission line detection. *IEEE Transactions on Aerospace and Electronic Systems*, 50(4):2890–2905, October 2014. 2.2.0.3

[68] H. Sharma, R. Bhujade, V. Adithya, and P. Balamuralidhar. Vision-based detection of power distribution lines in complex remote surroundings. In *2014 Twentieth National Conference on Communications (NCC)*, pages 1–6, Feb 2014. 2.2.0.3

[69] Zhengrong Li, Yuee Liu, Rodney Walker, Ross Hayward, and Jinglan Zhang. Towards automatic power line detection for a uav surveillance system using pulse coupled neural filter and an improved hough transform. *Machine Vision and Applications*, 21(5):677–686, 2010. 2.2.0.3

[70] G. Zhou and X. Zhou. Seamless fusion of lidar and aerial imagery for building extraction. *IEEE Transactions on Geoscience and Remote Sensing*, 52(11):7393–7407, Nov 2014. 2.2.0.3

[71] S. J. Mills, M. P. Gerardo Castro, Z. Li, J. Cai, R. Hayward, L. Mejias, and R. A. Walker. Evaluation of aerial remote sensing techniques for vegetation management in power-line corridors. *IEEE Transactions on Geoscience and Remote Sensing*, 48(9):3379–3390, Sept 2010. 2.2.0.3

[72] Milan Simic, Cees Bil, and Vuk Vojisavljevic. Investigation in wireless power transmission for {UAV} charging. *Procedia Computer Science*, 60:1846 – 1855, 2015. Knowledge-Based and Intelligent Information amp; Engineering Systems 19th Annual Conference, KES-2015, Singapore, September 2015 Proceedings. 2.2.0.3

[73] Mingbo Yang, Zize Liang, Hanbo Qian, En Li, and Guodong Yang. Design and analysis of multi-winding power current transformer for power transmission lines inspection robot. *Procedia Engineering*, 29:2187 – 2193, 2012. 2012 International Workshop on Information and Electronics Engineering. 2.2.0.3

[74] I. Golightly and Dewi Jones. Visual control of an unmanned aerial vehicle for power line inspection. In *Advanced Robotics, 2005. ICAR '05. Proceedings., 12th International Conference on*, pages 288–295, July 2005. 2.2.0.3

[75] D. I. Jones. An experimental power pick-up mechanism for an electrically driven uav. In *2007 IEEE International Symposium on Industrial Electronics*, pages 2033–2038, June 2007. 2.2.0.3

[76] K. Toussaint, N. Pouliot, and S. Montambault. Transmission line maintenance robots capable of crossing obstacles: State-of-the-art review and challenges ahead. *Journal of Field Robotics*, 26(5):477–499, 2009. 2.3.0.1

[77] M. Campos, G. Pereira, S. Vale, A. Bracarense, G. Pinheiro, and M. Oliveira. A mobile manipulator for installation and removal of aircraft warning spheres on aerial power transmission lines. In *Robotics and Automation, 2002. Proceedings. ICRA '02. IEEE International Conference on*, volume 4, pages 3559–3564 vol.4, 2002. 2.3.0.1

[78] Byung-Hak Cho, Seung-Hyun Byun, Joon-Young Park, and Jin-Seok Kim. Development of automatic inspection robot for live-line insulators. In *Transmission Distribution Construction, Operation and Live-Line Maintenance, 2006. ESMO 2006. IEEE 11th International Conference on*, Oct 2006. 2.3.0.1

[79] Joon-Young Park, Jae-Kyung Lee, Byung-Hak Cho, and Ki-Yong Oh. Robot mechanism for inspection of live-line suspension insulator stringt, August 07 2012. US Patent 12,254,014. 2.3.0.1

[80] J.-F. Allan, S. Lavoie, S. Reiher, and G. Lambert. Climbing and pole line hardware installation robot for construction of distribution lines. In *Applied Robotics for the*

Power Industry (CARPI), 2010 1st International Conference on, pages 1–5, Oct 2010. 2.3.0.1

[81] M.N. Ahmadabadi, H. Moradi, A. Sadeghi, A. Madani, and M. Farahnak. The evolution of ut pole climbing robots. In *Applied Robotics for the Power Industry (CARPI), 2010 1st International Conference on*, pages 1–6, Oct 2010. 2.3.0.1

[82] Daniel Schmidt and Karsten Berns. Climbing robots for maintenance and inspections of vertical structures—a survey of design aspects and technologies. *Robotics and Autonomous Systems*, 61(12):1288 – 1305, 2013. 2.3.0.1

[83] V. Banthia, Y. Maddahi, S. Balakrishnan, and N. Sepehri. Haptic-enabled teleoperation of base-excited hydraulic manipulators applied to live-line maintenance. In *2014 IEEE/RSJ International Conference on Intelligent Robots and Systems*, pages 1222–1229, Sept 2014. 2.3.0.2

[84] K. Takaoka, K. Yokoyama, H. Wakisako, K. Yano, K. Higashijima, and S. Murakami. Development of the fully-automatic live-line maintenance robot-phase iii. In *Assembly and Task Planning, 2001, Proceedings of the IEEE International Symposium on*, pages 423–428, 2001. 2.3.0.2

[85] Lu Shouyin, Li Yanping, and Qi Wei. Robotic live-working for electric power lines maintenances. In *Industrial Electronics and Applications, 2009. ICIEA 2009. 4th IEEE Conference on*, pages 1716–1719, May 2009. 2.3.0.2

[86] D.N. O'Connell and D.K. Wabnegger. Method for stringing replacement optical ground wire or static wire near energized power lines, September 3 2015. US Patent App. 14/633,749. 2.3.0.2

[87] W. Scaff, R.A. Pavani, A. Riyuiti Hirakawa, O. Horikawa, and A. Chamas Filho. Automatic elevator for assisting maintenance of distribution power line - control system. In *Applied Robotics for the Power Industry (CARPI), 2014 3rd International Conference on*, pages 1–6, Oct 2014. 2.3.0.2

[88] Kiyoshi Tsukahara, Yorihiko Tanaka, Yingxin He, Toshihisa Miyamoto, and Kyouichi Tatsuno. *Conceptual Design of a Power Distribution Line Maintenance Robot Using a Developed CG Simulator and Experimental Robot System*, pages 340–351. Springer Berlin Heidelberg, Berlin, Heidelberg, 2008. 2.3.0.2

[89] J.L. Robitaille. Tree trimmer telescopic, March 3 2011. US Patent App. 12/583,893. 2.3.0.2

[90] J. Prohaska. Mobile tree-trimming apparatus, April 10 2014. US Patent 13,819,844. 2.3.0.2

[91] C. Skipper and J. Kregl. Rotary plant hedger, May 08 2014. US Patent 13,833,536. 2.3.0.2

[92] OFIL Systems. AVI ROM A flying corona detection robot system. http://www.ofilsystems.com/catalog/index.html, 2013. [Online; accessed 19-August-2016]. 2.3.0.3

[93] A. Haddock and D. Haddock. Apparatus and method for aerial chemical trimming of vegetation, November 24 2015. US Patent 9,192,947. 2.3.0.3

[94] M. Nayyerloo, X. Chen, and J.G.Chase. *Cable-Climbing Robots for Power Transmission Lines Inspection, Mobile Robots - State of the Art in Land, Sea, Air, and Collaborative Missions*. InTechl, 2009. 2.3.0.3

[95] Y. Bazi and F. Melgani. Convolutional svm networks for object detection in uav imagery. *IEEE Transactions on Geoscience and Remote Sensing*, PP(99):1–12, 2018. 3

[96] R. Platon, J. Martel, N. Woodruff, and T. Y. Chau. Online fault detection in pv systems. *IEEE Transactions on Sustainable Energy*, 6(4):1200–1207, Oct 2015. 3

[97] S. Salamanca, P. Merchán, and I. García. On the detection of solar panels by image processing techniques. In *2017 25th Mediterranean Conference on Control and Automation (MED)*, pages 478–483, July 2017. 3

[98] V. Golovko, S. Bezobrazov, A. Kroshchanka, A. Sachenko, M. Komar, and A. Karachka. Convolutional neural network based solar photovoltaic panel detection in satellite photos. In *2017 9th IEEE International Conference on Intelligent Data Acquisition and Advanced Computing Systems: Technology and Applications (IDAACS)*, volume 1, pages 14–19, Sept 2017. 3

[99] J. M. Malof, Rui Hou, L. M. Collins, K. Bradbury, and R. Newell. Automatic solar photovoltaic panel detection in satellite imagery. In *2015 International Conference on Renewable Energy Research and Applications (ICRERA)*, pages 1428–1431, Nov 2015. 3

[100] B. Feng, X. Shen, J. Long, and H. Chen. A novel crack detection algorithm for solar panel surface images. In *2013 International Conference on Computer Sciences and Applications*, pages 650–654, Dec 2013. 3

[101] Manolis I. A. Lourakis and Antonis A. Argyros. Sba: A software package for generic sparse bundle adjustment. *ACM Trans. Math. Softw.*, 36(1):2:1–2:30, March 2009. 3, 3.1.2.2

[102] A. J. Davison, I. D. Reid, N. D. Molton, and O. Stasse. Monoslam real time single camera slam. *IEEE Transactions on Pattern Analysis and Machine Intelligence*, 29(6):1052–1067, June 2007. 3

[103] G. Guidi, J. A. Beraldin, S. Ciofi, and C. Atzeni. Fusion of range camera and photogrammetry: a systematic procedure for improving 3-d models metric accuracy. *IEEE Transactions on Systems, Man, and Cybernetics, Part B (Cybernetics)*, 33(4):667–676, Aug 2003. 3

[104] Rodrigo Méndez Perez, Fernando Auat Cheein, and Joan R. Rosell-Polo. Flexible system of multiple rgb-d sensors for measuring and classifying fruits in agri-food industry. *Computers and Electronics in Agriculture*, 139:231 – 242, 2017. 3

[105] Marius Muja and David G. Lowe. Fast approximate nearest neighbors with automatic algorithm configuration. In *In VISAPP International Conference on Computer Vision Theory and Applications*, pages 331–340, 2009. 3, 3.1.2.2

[106] J. Y. Bouguet. *Camera Calibration Toolbox for Matlab*. Computational Vision at the California Institute of Technologyr, 2015. 3.1.2.1

[107] M. Putica. Adjustment of the images contrast and brightness in the ortophotomosaic of the high objects. In *ISPA 2001. Proceedings of the 2nd International Symposium on Image and Signal Processing and Analysis. In conjunction with 23rd International Conference on Information Technology Interfaces (IEEE Cat.*, pages 383–387, June 2001. 3.1.2.2

[108] G. X. Ritteri and J. N. Wilson. *Handbook of Computer Vision algorithms in image algebra*. CRC Pressl, 2001. 3.1.2.4, 4.1.2.1

[109] E. Skoplaki, A.G. Boudouvis, and J.A. Palyvos. A simple correlation for the operating temperature of photovoltaic modules of arbitrary mounting. *Solar Energy Materials and Solar Cells*, 92(11):1393 – 1402, 2008. 3.1.3.1

[110] J.C. Bezdek. *Pattern-Recognition with Fuzzy Objective Function Algorithms*. Kluwer Academic Publishers: Norwell, MA, USA, 1981. 3.1.3.2

[111] G. Acciani, O. Falcone, and S. Vergura. Typical defects of pv-cells. In *2010 IEEE International Symposium on Industrial Electronics*, pages 2745–2749, July 2010. 3.2.3

[112] Salazar, April M. and Macabebe, Erees Queen B. Hotspots detection in photovoltaic modules using infrared thermography. *MATEC Web Conf.*, 70:10015, 2016. 3.2.5, 3.2.5

[113] J.A. Tsanakas, D. Chrysostomou, P.N. Botsaris, and A. Gasteratos. Fault diagnosis of photovoltaic modules through image processing and canny edge detection on field thermographic measurements. *International Journal of Sustainable Energy*, 34(6):351–372, 2015. 3.2.5

[114] An infrared thermographic approach as a hot-spot detection tool for photovoltaic modules using image histogram and line profile analysis. *International Journal of Condition Monitoring*, 2(1), 2012. 3.2.5

[115] Open Source Robotics Foundation. ROS Indigo Igloo. http://wiki.ros.org/indigo, 2018. [Online; accessed 27-November-2018]. 4.1, 4.2

[116] S. Chen and Y. F. Li. Finding optimal focusing distance and edge blur distribution for weakly calibrated 3-d vision. *IEEE Transactions on Industrial Informatics*, 9(3):1680–1687, Aug 2013. 4.1.2.1

[117] J. M. Geusebroek, A. W. M. Smeulders, and J. van de Weijer. Fast anisotropic gauss filtering. *IEEE Transactions on Image Processing*, 12(8):938–943, Aug 2003. 4.1.2.1

[118] Alonso Kelly. *Mobile Robotics Mathematics, Models and Methods*. Cambridgel, 2013. 4.1.2.3

[119] Open Source Robotics Foundation. GAZEBO Robot simulation made easy. http://gazebosim.org/, 2014. [Online; accessed 22-August-2017]. 4.2

[120] MATLAB. *version 9.4.0.813650 (R2018a)*. The MathWorks Inc., Natick, Massachusetts, 2018. 4.2

[121] J. Kim and S. Sukkarieh. Autonomous airborne navigation in unknown terrain environments. *IEEE Transactions on Aerospace and Electronic Systems*, 40(3):1031–1045, July 2004. 4.2.1

[122] Y. Tang, Y. Hu, J. Cui, F. Liao, M. Lao, F. Lin, and R. S. H. Teo. Vision-aided multi-uav autonomous flocking in gps-denied environment. *IEEE Transactions on Industrial Electronics*, 66(1):616–626, Jan 2019. 4.2.1

[123] G. Mao and B. Fidan. *Localization Algorithms and Strategies for Wireless Sensor Networks*. Information Science Reference, 1 edition, 2009. 4.2.5

[124] V. C. Gungor, D. Sahin, T. Kocak, S. Ergut, C. Buccella, C. Cecati, and G. P. Hancke. A survey on smart grid potential applications and communication requirements. *IEEE Transactions on Industrial Informatics*, 9(1):28–42, Feb 2013. 5, 5.1, 5.1

[125] M. Alhawari, B. Mohammad, H. Saleh, and M. Ismail. A survey of thermal energy harvesting techniques and interface circuitry. In *2013 IEEE 20th International Conference on Electronics, Circuits, and Systems (ICECS)*, pages 381–384, Dec 2013. 5.1, 5.1

[126] A. Decker. Solar energy harvesting for autonomous field devices. *IET Wireless Sensor Systems*, 4(1):1–8, March 2014. 5.1, 5.1, 5.1.1.3

[127] R. Moghe, A. R. Iyer, F. C. Lambert, and D. M. Divan. A low-cost wireless voltage sensor for monitoring mv/hv utility assets. *IEEE Transactions on Smart Grid*, 5(4):2002–2009, July 2014. 5.1, 5.1.2

[128] F. Guo, H. Hayat, and J. Wang. Energy harvesting devices for high voltage transmission line monitoring. In *2011 IEEE Power and Energy Society General Meeting*, pages 1–8, July 2011. 5.1, 5.1, 5.1.1.6, 5.1.2, 5.1.2

[129] Jianxin Guo, Hang Hu, Xinyu Da, Jian Liu, and Wei Li. Optimization of energy efficiency for cognitive radio with partial rf energy harvesting. *AEU - International Journal of Electronics and Communications*, 85:74 – 77, 2018. 5.1

[130] F. Dell'Anna, T. Dong, P. Li, W. Yumei, Z. Yang, M. R. Casu, M. Azadmehr, and Y. Berg. State-of-the-art power management circuits for piezoelectric energy harvesters. *IEEE Circuits and Systems Magazine*, 18(3):27–48, thirdquarter 2018. 5.1, 5.1, 5.1.1.1, 5.1.1.3

[131] Aman Kansal, Jason Hsu, Sadaf Zahedi, and Mani B. Srivastava. Power management in energy harvesting sensor networks. *ACM Trans. Embed. Comput. Syst.*, 6(4), September 2007. 5.1.1

[132] E. O. Torres and G. A. Rincon-Mora. Self-tuning electrostatic energy-harvester ic. *IEEE Transactions on Circuits and Systems II: Express Briefs*, 57(10):808–812, Oct 2010. 5.1

[133] R. Bolt, M. Magno, T. Burger, A. Romani, and L. Benini. Kinetic ac/dc converter for electromagnetic energy harvesting in autonomous wearable devices. *IEEE Transactions on Circuits and Systems II: Express Briefs*, 64(12):1422–1426, Dec 2017. 5.1

[134] Y. Qian, D. Lu, J. He, and Z. Hong. An onchip transformer-based selfstartup hybrid sidito converter for thermoelectric energy harvesting. *IEEE Transactions on Circuits and Systems II: Express Briefs*, 65(11):1673–1677, Nov 2018. 5.1

[135] M. Zhu, P. C. Baker, N. M. Roscoe, M. D. Judd, and J. Fitch. Alternative power sources for autonomous sensors in high voltage plant. In *2009 IEEE Electrical Insulation Conference*, pages 36–40, May 2009. 5.1, 5.1.2, 5.2

[136] Fayaz Akhtar and Mubashir Husain Rehmani. Energy replenishment using renewable and traditional energy resources for sustainable wireless sensor networks: A review. *Renewable and Sustainable Energy Reviews*, 45:769 – 784, 2015. 5.1, 5.1.1.3

[137] H. Kim, Y. Min, C. Jeong, K. Kim, C. Kim, and S. Kim. A 1-mw solar-energy-harvesting circuit using an adaptive mppt with a sar and a counter. *IEEE Transactions on Circuits and Systems II: Express Briefs*, 60(6):331–335, June 2013. 5.1

[138] Yanyan Shi, Jianwei Jing, Yue Fan, Lan Yang, Yan Li, and Meng Wang. A novel compact broadband rectenna for ambient rf energy harvesting. *AEU - International Journal of Electronics and Communications*, 95:264 – 270, 2018. 5.1, 5.1.1.4

[139] D. Mishra, S. De, and K. R. Chowdhury. Charging time characterization for wireless rf energy transfer. *IEEE Transactions on Circuits and Systems II: Express Briefs*, 62(4):362–366, April 2015. 5.1, 5.1.1.4

[140] Marzieh Beheshti Asl and Mohammad Hossein Zarifi. Rf to dc micro-converter in standard cmos process for on-chip power harvesting applications. *AEU - International Journal of Electronics and Communications*, 68(12):1180 – 1184, 2014. 5.1, 5.1.1.4

[141] Gaurav Singh, Rahul Ponnaganti, T.V. Prabhakar, and K.J. Vinoy. A tuned rectifier for rf energy harvesting from ambient radiations. *AEU - International Journal of Electronics and Communications*, 67(7):564 – 569, 2013. 5.1, 5.1.1.4

[142] O. Cetinkaya and O. B. Akan. Electric-field energy harvesting in wireless networks. *IEEE Wireless Communications*, 24(2):34–41, April 2017. 5.1, 5.1.1.5, 5.1.1.6, 5.1.2, 5.1.2, 5.2

[143] S. Yuan, Y. Huang, J. Zhou, Q. Xu, C. Song, and P. Thompson. Magnetic field energy harvesting under overhead power lines. *IEEE Transactions on Power Electronics*, 30(11):6191–6202, Nov 2015. 5.1, 5.1.1.5

[144] H. Zangl, T. Bretterklieber, and G. Brasseur. A feasibility study on autonomous online condition monitoring of high-voltage overhead power lines. *IEEE Transactions on Instrumentation and Measurement*, 58(5):1789–1796, May 2009. 5.1, 5.1.1.6, 5.1.2, 5.1.2, 5.2

[145] R. Moghe, A. R. Iyer, F. C. Lambert, and D. Divan. A low-cost electric field energy harvester for an mv/hv asset-monitoring smart sensor. *IEEE Transactions on Industry Applications*, 51(2):1828–1836, March 2015. 5.1, 5.1.1.6, 5.2

[146] S. Sudevalayam and P. Kulkarni. Energy harvesting sensor nodes: Survey and implications. *IEEE Communications Surveys Tutorials*, 13(3):443–461, Third 2011. 5.1.1.1, 5.1.1.2, 5.1.1.3, 5.1.1.4

[147] Shad Roundy. On the effectiveness of vibration-based energy harvesting. *Journal of Intelligent Material Systems and Structures*, 16(10):809–823, 2005. 5.1.1.1

[148] Alberto Arroyo, Pablo Castro, Raquel Martinez, Mario Manana, Alfredo Madrazo, Ramón Lecuna, and Antonio Gonzalez. Comparison between ieee and cigre thermal behaviour standards and measured temperature on a 132-kv overhead power line. *Energies*, 8(12):13660–13671, 2015. 5.1.1.2

[149] A. E. Tzinevrakis, D. K. Tsanakas, and E. I. Mimos. Analytical calculation of the electric field produced by single-circuit power lines. *IEEE Transactions on Power Delivery*, 23(3):1495–1505, July 2008. 5.1.2

[150] S. Kang, J. Kim, S. Yang, T. Yun, and H. Kim. Electric field energy harvesting under actual three-phase 765 kv power transmission lines for wireless sensor node. *Electronics Letters*, 53(16):1135–1136, 2017. 5.1.2, 5.1.2

[151] K. Chang, Sungmuk Kang, Kyungjin Park, Seunghwan Shin, Hyeong-Seok Kim, and Hoseong Kim. Electric Field Energy Harvesting Powered Wireless Sensors for Smart Grid. *Journal of Electrical Engineering & Technology*, 7:75–80, 2012. 5.1.2, 5.1.2

[152] H. Kim, D. Choi, S. Gong, and K. Park. Stray electric field energy harvesting technology using mems switch from insulated ac power line. *Electronics Letters*, 50(17):1236–1238, Aug 2014. 5.1.2, 5.1.2, 5.2.1.2

[153] H. Zangl, T. Bretterklieber, and G. Brasseur. Energy harvesting for online condition monitoring of high voltage overhead power lines. In *2008 IEEE Instrumentation and Measurement Technology Conference*, pages 1364–1369, May 2008. 5.1.2

[154] M. J. Moser, T. Bretterklieber, H. Zangl, and G. Brasseur. Strong and weak electric field interfering: Capacitive icing detection and capacitive energy harvesting on a 220-kv high-voltage overhead power line. *IEEE Transactions on Industrial Electronics*, 58(7):2597–2604, July 2011. 5.1.2

[155] J. Zhang, P. Li, Y. Wen, F. Zhang, and C. Yang. A management circuit with upconversion oscillation technology for electric-field energy harvesting. *IEEE Transactions on Power Electronics*, 31(8):5515–5523, Aug 2016. 5.1.2

[156] T. Keutel, X. Zhao, and O. Kanoun. Energy scavenging for monitoring of overhead power line networks. In *Proceedings SENSOR 2009, Volume II*, pages 207 – 212, Jun 2009. 5.1.2

[157] X. Zhao, T. Keutel, M. Baldauf, and O. Kanoun. Energy harvesting for a wireless-monitoring system of overhead high-voltage power lines. *IET Generation, Transmission Distribution*, 7(2):101–107, Feb 2013. 5.1.2

[158] J. C. Rodríguez, D. G. Holmes, B. P. McGrath, and R. H. Wilkinson. Maximum energy harvesting from medium voltage electric-field energy using power line insulators. In *2014 Australasian Universities Power Engineering Conference (AUPEC)*, pages 1–6, Sep. 2014. 5.1.2

[159] R. Moghe, Y. Yang, F. Lambert, and D. Divan. A scoping study of electric and magnetic field energy harvesting for wireless sensor networks in power system applications. In *2009 IEEE Energy Conversion Congress and Exposition*, pages 3550–3557, Sept 2009. 5.1.2

[160] D. Zhao, D. Dai, and L. Li. Electric field energy harvesting for on-line condition-monitoring device installed on high-voltage transmission tower. *Electronics Letters*, 51(21):1692–1693, 2015. 5.1.2

[161] S. Kang, S. Yang, and H. Kim. Non-intrusive voltage measurement of ac power lines for smart grid system based on electric field energy harvesting. *Electronics Letters*, 53(3):181–183, 2017. 5.1.2

[162] J. C. Rodríguez, D. G. Holmes, B. Mcgrath, and R. H. Wilkinson. A self-triggered pulsed-mode flyback converter for electric-field energy harvesting. *IEEE Journal of Emerging and Selected Topics in Power Electronics*, 6(1):377–386, March 2018. 5.2

[163] X. Zhao, T. Keutel, M. Baldauf, and O. Kanoun. Energy harvesting for overhead power line monitoring. In *International Multi-Conference on Systems, Signals Devices*, pages 1–5, March 2012. 5.2

[164] M. Zhu, A. Reid, S. Finney, and M. Judd. Energy scavenging technique for powering wireless sensors. In *2008 International Conference on Condition Monitoring and Diagnosis*, pages 881–884, April 2008. 5.2